Hall effect of itinerant electron metamagnetic systems

田邉, 巧祐

Hall effect of itinerant electron metamagnetic systems

Doctoral Dissertation

Kosuke Tanabe
Department of Physics, Graduate School of Science,
Kyushu University

2023

Abstract

Itinerant electron metamagnetism (IEM) means a magnetic transition from a Pauli paramagnetic state to a ferromagnetic state induced by a magnetic field. We notice that the itinerant electron metamagnetic materials are suitable systems to compare physical properties between the ferromagnetic and paramagnetic states, because both states are realized depending on a magnetic field at the same temperature. In the present study, we focus on Hall effect. It is known that the Hall effect of magnetic materials consists of the normal Hall effect (NHE) and the anomalous Hall effect (AHE). The former reflects the electronic structure near the Fermi level, whereas the latter is proportional to the magnetization *M*. In the ferromagnetic state, the NHE and AHE can be separated. However, it is difficult to separate these two terms in the paramagnetic state, because both are proportional to *M*. In the present study, we found that IEM enables us to determine the normal Hall coefficients in both the ferromagnetic and paramagnetic states simultaneously, under the assumption that the anomalous Hall coefficient is independent of the magnetic state.

In Chapter 3, we explained our analytical method and apply it to the Hall resistivity of $Co(S_{1-x}Se_x)_2$. We successfully determined the normal Hall coefficients of both ferromagnetic and paramagnetic states. The validity of the assumption on the AHE was also checked. The electronic structure was calculated for CoS_2 and $CoSe_2$ by full-potential linearized-augmented-plane-wave (FLAPW) method. The normal Hall coefficients were evaluated theoretically for nonmagnetic and ferromagnetic state of CoS_2, and they are compared with the experimental results. The difference between the calculated results and the experimental ones were discussed.

Hall effect of $Lu(Co_{0.91}Al_{0.09})_2$, $LuCo_2$ and $ErCo_2$ were described in Chapter 4. Our analytical method was applied to the Hall resistivity of $Lu(Co_{0.91}Al_{0.09})_2$.The energy band calculations were performed for nonmagnetic and ferromagnetic state of $LuCo_2$. The calculated normal Hall coefficients were compared with the experimental results of these compounds. For $ErCo_2$, we used a conventional method to analyze the Hall resistivity, because the above assumption on the AHE is not valid. It was found that the anomalous Hall coefficient changes the sign from positive to negative at the Curie temperature. The origin of this sign change was discussed.

Chapter 5 gives the experimental data of Hall effect of $La(Fe_{1-x}Si_x)_{13}$. The measurements were carried out at pressures of 0.5 and 1.0 GPa, because high pressures make the itinerant electron metamagnetic transition temperature lower. By applying the conventional method, we estimated the normal Hall coefficient in the ferromagnetic state. The results were discussed in the framework of two carrier model. These compounds show large AHE. The origin of AHE of this system was discussed by referring the previous work reported by Karpenkov *et al*. These compounds show positive magnetoresistance (MR). We also discussed the origin of positive MR on the basis of the electronic structure.

Finally, the conclusions were given in Chapter 6.

Contents

Chapter 1 Introduction

1.1 Itinerant electron metamagnetism (IEM)

A sudden increase in magnetization upon the application of a magnetic field is called metamagnetism. This is schematically shown in Fig. 1-1. Originally, metamagnetism means a magnetic transition from an antiferromagnetic state to a ferromagnetic state in the magnetization process. This is a first-order magnetic transition (FOMT) accompanied by a hysteresis. The metamagnetic behavior is also observed for metallic systems. In 1962, Wohlfarth and Rhodes predicted that a ferromagnetic state can be induced by a magnetic field for some metallic paramagnets [1]. This is a transition from a Pauli paramagnetic state to a ferromagnetic state and it is called itinerant electron metamagnetism (IEM). It is known that a peculiar energy band structure near the Fermi level is responsible for the onset of IEM [2]. When the Fermi level ε_F is situated at the bottom of a valley or at the foot of a peak in the density of states (DOS), as shown in Fig. 1-2, IEM can take place. This is because the application of a magnetic field increases the total density of states at ε_F, $D(\varepsilon_F,)$ which is favorable to satisfy the Stoner condition for the onset of ferromagnetism.

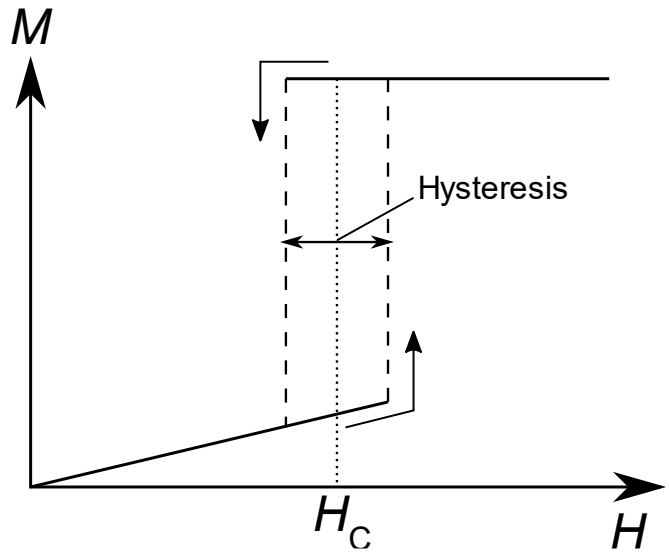

Fig. 1-1 Schematic illustration of metamagnetism.

Typical examples of IEM are $Co(S_{1-x}Se_x)_2$, RCo_2 (R = rare earth elements) and $La(Fe_{1-x}Si_x)_{13}$. The magnetic properties of these systems will be described in sections 1.3-1.5. IEM was reported not only for 3*d* electron systems, but also for 4*d* ($Sr_3Ru_2O_7$) and 5*f* (UCoAl) electron systems [3, 4]. In the last two decades, IEM has attracted attention for the application to materials science. Some 3*d* transition metal systems showing IEM have large magnetocaloric effects [5, 6]. These compounds are considered as potential candidates of working material of magnetic refrigeration near room temperature. On the other hand, new materials exhibiting IEM have been reported still recently, such as Fe_3Mo_3N [7], $Sr_{1-x}Ca_xCo_2P_2$ [8], and $LaFe_{12}B_6$ [9]. Thus, IEM is extensively

studied from both the fundamental and applied aspects, currently. It should be noted that the material showing IEM is a suitable system to compare physical properties between the ferromagnetic and paramagnetic states, because both states can be realized depending on a magnetic field at the same temperature. In this thesis, we focus on Hall effect of itinerant electron metamagnetic systems.

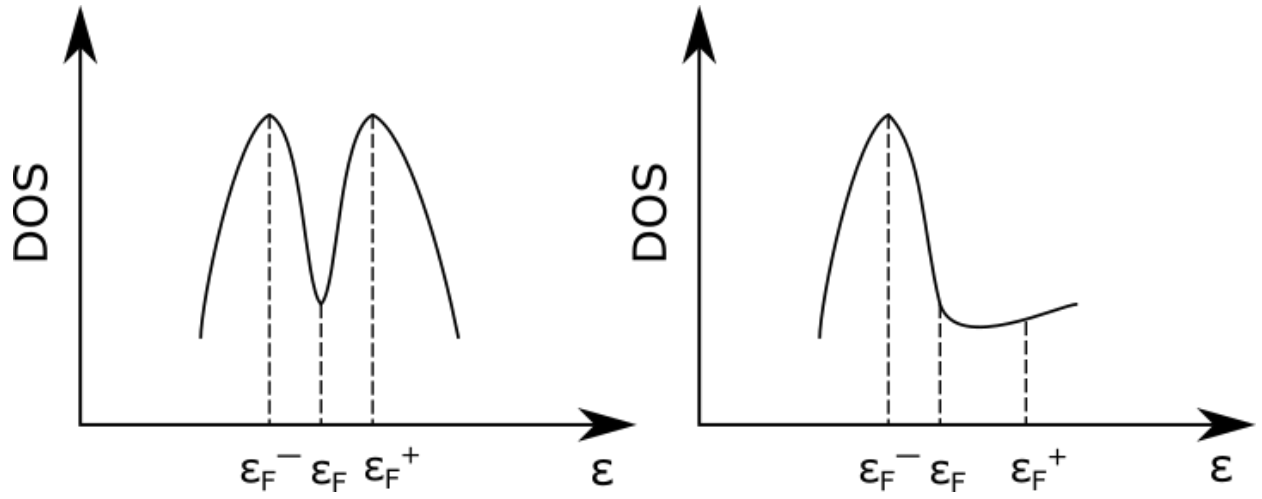

Fig. 1-2 Typical DOS curves which are favorable for onset of IEM. Here, ε_F is the Fermi level in the paramagnetic state and ε_F^+ and ε_F^- mean the Fermi level of up-spin and down-spin bands in the induced ferromagnetic state, respectively.

1.2 Theoretical background

Wohlfarth and Rhodes predicted IEM using a phenomenological Landau theory [1]. Shimizu discussed rigorous conditions for the onset of IEM [10]. In 1990's, Yamada extended the theory of IEM to finite temperatures by taking the effects of spin fluctuations into account [11]. In this section, we summarize the theory of IEM.

First, we review the theory of IEM at absolute zero ($T = 0$). In the Landau theory, the magnetic part of the free energy ΔF can be expanded as a power series in the magnetization M,

$$\Delta F(M) = \tfrac{1}{2} aM^2 + \tfrac{1}{4} bM^4 + \tfrac{1}{6} cM^6, \quad (1.1)$$

where a, b and c are Landau expansion coefficients depending on the electronic structure near the Fermi level. When $a > 0$, $b < 0$, $c > 0$ and $ac/b^2 < 3/16$, $\Delta F(M)$ has two minima at $M = 0$ and at a finite value of $M = M_0$ with $\Delta F(M_0) < \Delta F(0)$. The magnetic equation of state is expressed as,

$$\frac{d\Delta F}{dM} = H = aM + bM^3 + cM^5. \quad (1.2)$$

The condition for the occurrence of IEM is given by,

$$a > 0,\ b < 0,\ c > 0, \quad \text{and} \quad \frac{3}{16} < \frac{ac}{b^2} < \frac{9}{20}. \qquad (1.3)$$

This is obtained by the condition that the transition field H_C is positive. As shown in Fig. 1-3, a vertical line at H_C is drawn such that the two areas marked by the circles are equal from Maxwell construction.

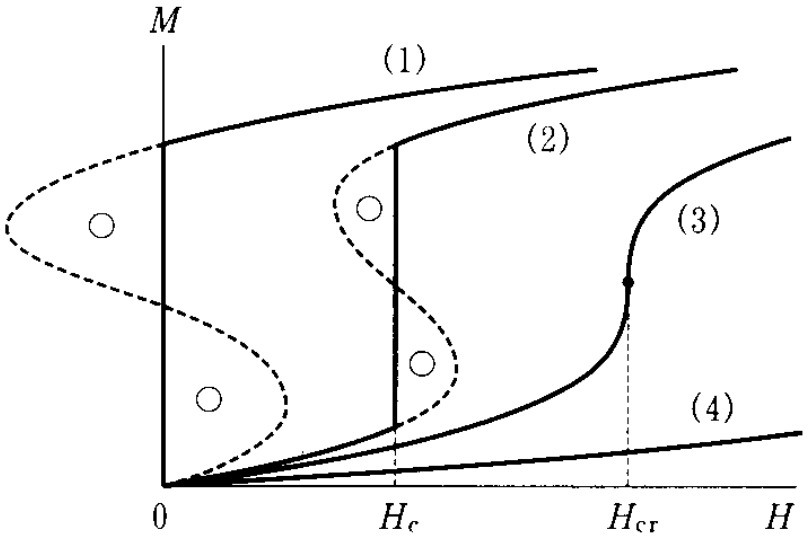

Fig.1-3 Schematic illustration of eq. (1.2). Curves (1), (2) and (3) correspond to $ac/b^2 = 3/16$, $3/16 < ac/b^2 < 9/20$, and $ac/b^2 = 9/20$, respectively [2].

At finite temperatures, the scenario is almost the same, but Landau expansion coefficients are dependent on temperature by the effect of spin fluctuations.

$$H = A(T)M + B(T)M^3 + C(T)M^5, \qquad (1.4)$$

where,

$$\begin{aligned} A(T) &= a + \tfrac{5}{3}b\xi(T)^2 + \tfrac{35}{9}c\xi(T)^4, \\ B(T) &= b + \tfrac{14}{3}c\xi(T)^2, \\ C(T) &= c. \end{aligned} \qquad (1.5)$$

Here, $\xi(T)^2$ is the mean square amplitude of thermal spin fluctuations. It is known that $\xi(T)^2$ is proportional to T^2 at low temperatures and to T at high temperatures. Since $\xi(T)^2$ increases monotonically with increasing temperature, we can discuss IEM qualitatively. The condition for the occurrence of IEM is similar to eq. (1.2),

$$A(T) > 0,\ B(T) < 0,\ C(T) > 0, \quad \text{and} \quad \frac{3}{16} < \frac{A(T)C(T)}{B(T)^2} < \frac{9}{20}. \qquad (1.6)$$

We introduce four important temperatures. Temperature dependence of the magnetic susceptibility χ is given by,

$$\chi = \frac{1}{A(T)}. \qquad (1.7)$$

We define $T_{\max}$ as the temperature, where χ has a maximum. $\xi(T_{\max})^2$ is written as,

$$\xi(T_{\max})^2 = \frac{3}{14}\frac{|b|}{c}. \qquad (1.8)$$

The condition $A(T)C(T)/B^2(T) = 9/20$ gives the temperature T_0, at which IEM disappears. $\xi(T_0)^2$ is given by,

$$\xi(T_0)^2 = \xi(T_{\max})^2\left(1-\sqrt{\frac{70}{19}}\sqrt{\frac{ac}{b^2}-\frac{5}{28}}\right). \qquad (1.9)$$

The condition $A(T)C(T)/B^2(T) = 3/16$ gives the temperature T_1, at which a ferromagnetic state is realized. $\xi(T_1)^2$ is given by,

$$\xi(T_1)^2 = \xi(T_{\max})^2\left(1-4\sqrt{7}\sqrt{\frac{ac}{b^2}-\frac{5}{28}}\right). \qquad (1.10)$$

It is easy to show $\xi(T_1)^2 < \xi(T_0)^2 < \xi(T_{\max})^2$. This fact means $T_1 < T_0 < T_{\max}$. Substituting eq. (1.10) to eqs. (1.5), we have $A(T_1) > 0$ and $B(T_1) < 0$. Therefore, a FOMT takes place at T_1. Finally, the Curie temperature T_C is determined from $A(T_C) = 0$ and $B(T_C) > 0$

$$\xi(T_C)^2 = \xi(T_{\max})^2\left(1+2\sqrt{\frac{7}{5}}\sqrt{\frac{5}{28}-\frac{ac}{b^2}}\right). \qquad (1.11)$$

Equations (1.9) - (1.11) indicate that $\xi(T)^2/\xi(T_{\max})^2$ only depends on ac/b^2. The ac/b^2 dependence of $\xi(T)^2$ ($T = T_0$, T_1 and T_C) is illustrated in Fig. 1-4. The vertical axis $\xi(T)^2$ reduced by $|b|/c$ corresponds to temperature, because $\xi(T)^2$ is a monotonically increasing function of T. On the other hand, the value of ac/b^2 can be changed

by pressure or alloying. Therefore, Fig. 1-4 can be regarded as a magnetic phase diagram. It is noted that IEM appears in the region of $T_1 < T < T_0$.

This theory is successfully applied to IEM of RCo_2, $Co(S_{1-x}Se_x)_2$ and $La(Fe_{1-x}Si_x)_{13}$ [12]. In this thesis, we study Hall effect of these materials, so that we review their magnetic properties in the following subsections.

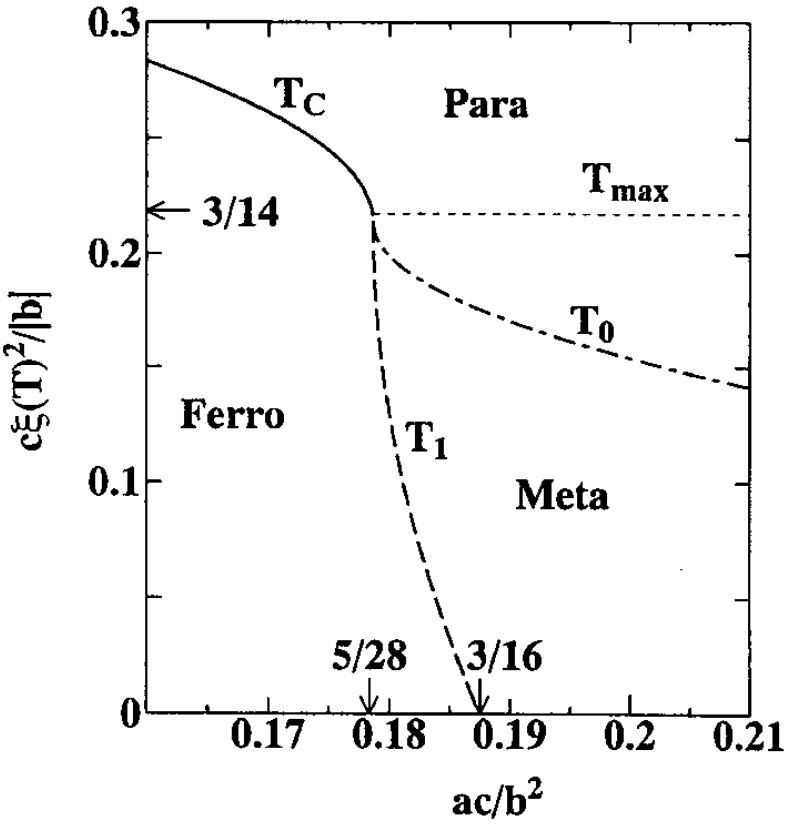

Fig.1-4 Magnetic phase diagram of IEM [11]. The vertical axis corresponds to temperature and the horizontal axis to pressure or composition. IEM takes place in the region of $T_1 < T < T_0$.

1.3 $Co(S_{1-x}Se_x)_2$

The CoS_2 and $CoSe_2$ compounds form the Pyrite structure, which is shown in Fig. 1-5 [13]. This structure is cubic and can be regarded as an NaCl-type structure with Co atoms and chalcogen atom pairs. The Co atoms occupy the 4*a* site, while the S and Se atoms occupy the 8*c* site. The unit cell contains four formula units.

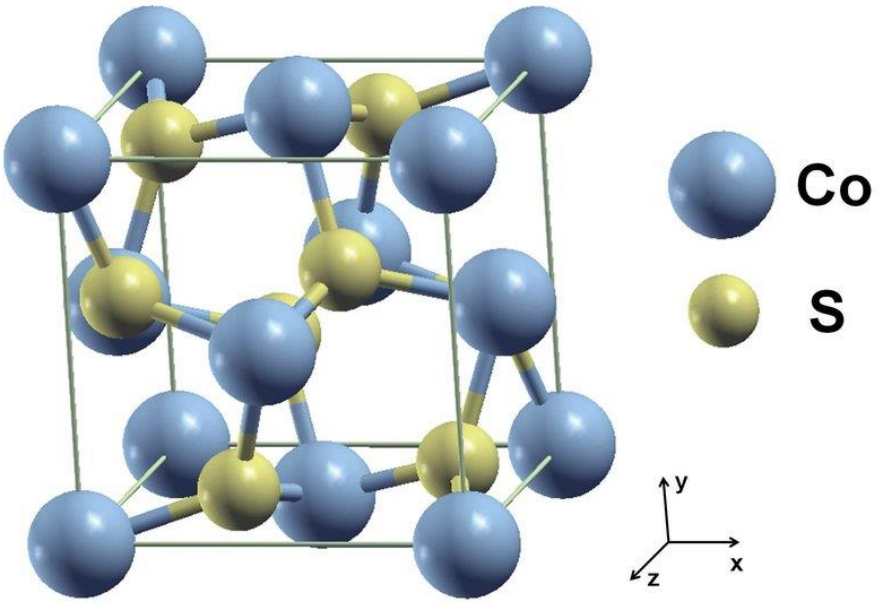

Fig. 1-5 Crystal structure of Pyrite CoS_2. This figure is taken from ref 13.

In the cubic symmetry, the 3*d* band is split into t_{2g} and e_g subbands by the crystalline field. It is known that 3*d* electrons of the Co atoms are in the low-spin state. Thus, the t_{2g} subband is completely filled and the e_g subband is partially filled with one 3*d* electron per Co atom. CoS_2 is a ferromagnet with T_C =120 K and a saturation magnetization of 0.85 μ_B/Co, whereas $CoSe_2$ is a strongly enhanced Pauli paramagnet. The pseudo-binary $Co(S_{1-x}Se_x)_2$ has a solid solution in the whole concentration range of x. In $Co(S_{1-x}Se_x)_2$, T_C is rapidly decreased with increasing x and ferromagnetism disappears at around $x = 0.12$. For $0.03 \leq x \leq 0.11$, the magnetic transition is first-order. IEM of $Co(S_{1-x}Se_x)_2$ was first reported by Adachi *et al*. for $x = 0.12$ and 0.14 [14]. Later, Goto *et al*. studied IEM of this system with $0 \leq x < 0.20$ under high magnetic fields and high pressures [15]. The magnetization curves of $Co(S_{1-x}Se_x)_2$ at 4.2 K are displayed in Fig. 1-6. The compounds with $x = 0$ and 0.10 show ferromagnetic behavior. On the other hand, sharp metamagnetic transitions are observed for $0.12 \leq x < 0.20$ accompanied by a hysteresis. The saturation magnetization is weakly dependent on x. The $M - B$ curves of $x = 0.14$ at various temperatures are depicted in Fig. 1-7. With increasing temperature, the transition field B_C is increased, while the hysteresis becomes smaller. Above 60 K, the transition becomes broad, and the hysteresis vanishes, suggesting disappearance of IEM.

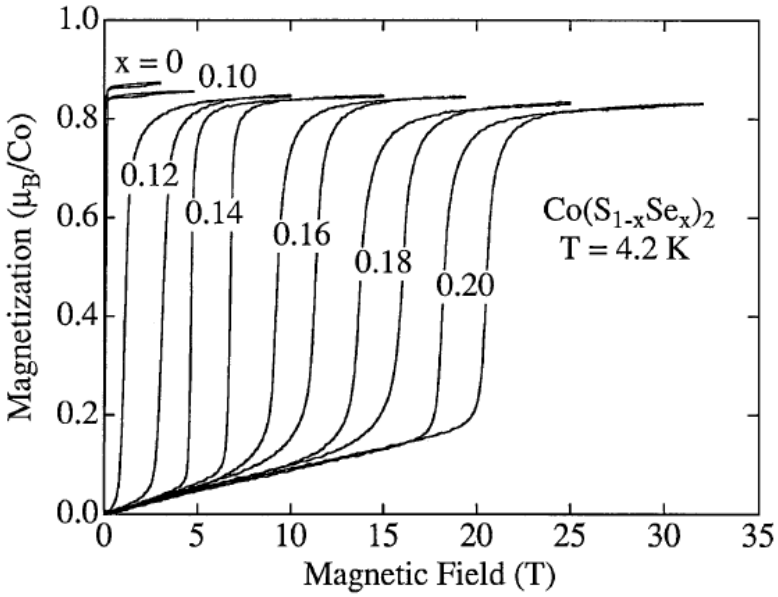

Fig. 1-6 The magnetization curves of $Co(S_{1-x}Se_x)_2$ with $0 \leq x < 0.20$ at 4.2 K [15].

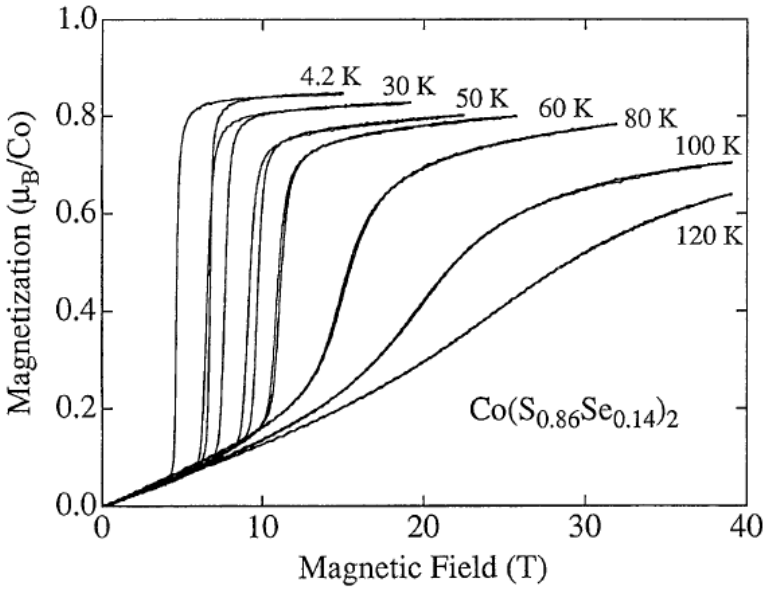

Fig. 1-7 The magnetization curves of $x = 0.14$ at various temperatures [15].

The $T - x$ magnetic phase diagram of $Co(S_{1-x}Se_x)_2$ is illustrated in Fig. 1-8. IEM appears between T_C and T_0 which is temperature that IEM disappear. The phase diagram is well reproduced by the theoretical phase diagram shown in Fig. 1-4. The application of pressure on CoS_2 also induces IEM. The $T - p$ phase diagram of CoS_2 is very similar to the $T - x$ phase diagram of $Co(S_{1-x}Se_x)_2$ [15]. Sadakuni *et al*. have estimated that 1% Se substitution corresponds to a pressure of 0.48 GPa in $Co(S_{1-x}Se_x)_2$ [16]. These results indicate that magnetic behavior of $Co(S_{1-x}Se_x)_2$ is well described by the theory of IEM, in which the effects of spin fluctuations are taken into consideration.

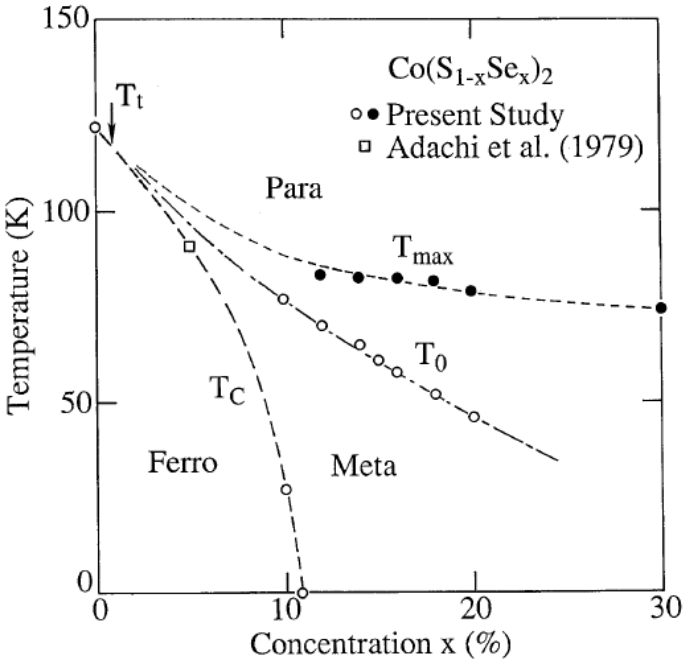

Fig. 1-8 Magnetic phase diagram of $Co(S_{1-x}Se_x)_2$ [15].

1.4 RCo_2 and $Lu(Co_{1-x}Al_x)_2$

Among the intermetallic compounds between rare-earth elements (R) and 3*d* transition metals, the cubic Laves phase compounds RCo_2 exhibit unique magnetic properties. Figure 1-9 shows the crystal structure of C15 Laves phase. Both R and Co atoms occupy one equivalent site, 8*a* and 16*d*, respectively. The unit cell contains eight formula units. The R atoms form the diamond lattice and the Co atoms form the corner-sharing tetrahedron lattice.

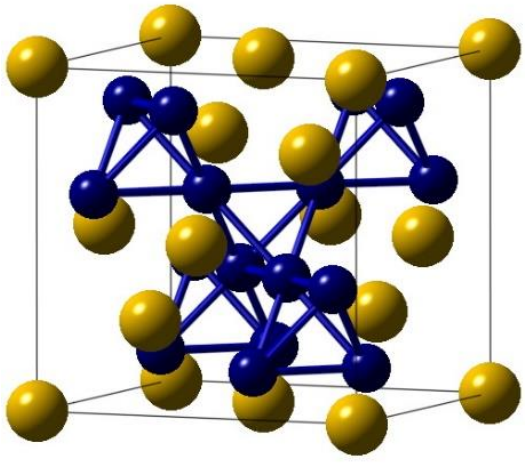

Fig. 1-9 Crystal structure of C15 Laves phase. R and Co atoms are represented by yellow and blue circles, respectively. This figure is taken from ref. 17.

YCo_2 and $LuCo_2$, where Y and Lu are nonmagnetic elements, are strongly exchange-enhanced Pauli paramagnets. The magnetic susceptibility χ of these compounds are very large compared with that expected from $D(\varepsilon_F)$, indicating the Stoner enhancement factor is more than 20 [18,19]. Moreover, χ of these compounds increases with increasing temperature, having a maximum near room temperature. At higher temperatures, χ decreases with temperature following the Curie-Weiss law [20]. When R is a magnetic rare-earth element, Co possesses a magnetic moment by a molecular field from R. The molecular field is proportional to the spin component of the R moment, $(g_J - 1)J$, where g_J is the Landé g-factor and J the total angular momentum. It has been found that the Co moment is abruptly induced above the critical field [21, 22]. Therefore, YCo_2 and $LuCo_2$ are expected to show IEM at high magnetic fields. Band calculations predicted B_C for IEM is in the range of 90 – 350 T for YCo_2 [23, 24]. Schinkel measured the magnetization of YCo_2 at 4.2 K and 77 K up to 38 T [25]. He observed upturns in the $M - B$ curves above 15 T, suggesting an initial stage of IEM. The complete IEM for YCo_2 and $LuCo_2$ was observed by Goto *et al.* in 1989 [26, 27]. Using a destructive single-turn coil, they measured the magnetization up to 100 T and observed IEM of YCo_2 and $LuCo_2$ at around 70 T. It was found that B_C of YCo_2 is proportional to T^2 at low temperatures. The T^2 dependence of B_C is explained by the theory of IEM described previously. Figure 1-10 displays the plots of Co moment vs effective magnetic field of RCo_2 [12]. The effective field of RCo_2 is calculated from the molecular field, which is calibrated by the magnetization curve of $LuCo_2$.

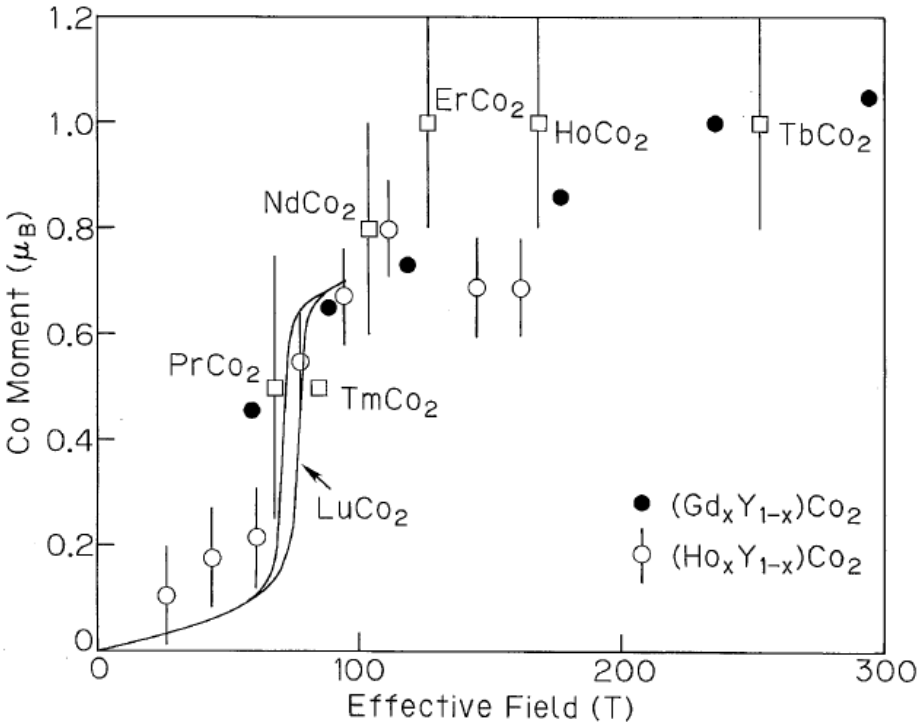

Fig. 1-10 Plots of Co moment vs the effective magnetic field of RCo_2. The magnetization curve of $LuCo_2$ is also shown [12].

In the case of heavy rare-earth elements, the Co moments align antiparallel to the R moments, so that a ferrimagnetic structure is realized below the Curie temperature T_C. The compounds with R = Dy, Ho and Er undergo a FOMT at T_C of 32–135 K, while a second-order magnetic transition takes place for $GdCo_2$ and $TbCo_2$ at 230 K and 395 K, respectively [28]. The order of magnetic phase transitions in RCo_2 was discussed by Bloch *et al*. in the framework of the phenomenological Landau theory [28].

$ErCo_2$ exhibits a FOMT at T_C = 32 K. Neutron diffraction measurements reported that the Er and Co moments at low temperatures are 9.0 μ_B and 1.0 μ_B, respectively [29, 30]. Figure 1-11 shows the magnetization curves of $ErCo_2$ single crystal, when the magnetic field is applied parallel to [111] axis (easy axis of magnetization) [31]. Above T_C, the compound shows metamagnetic behavior from a paramagnetic to ferrimagnetic state. This transition is accompanied by IEM of the Co sublattice.

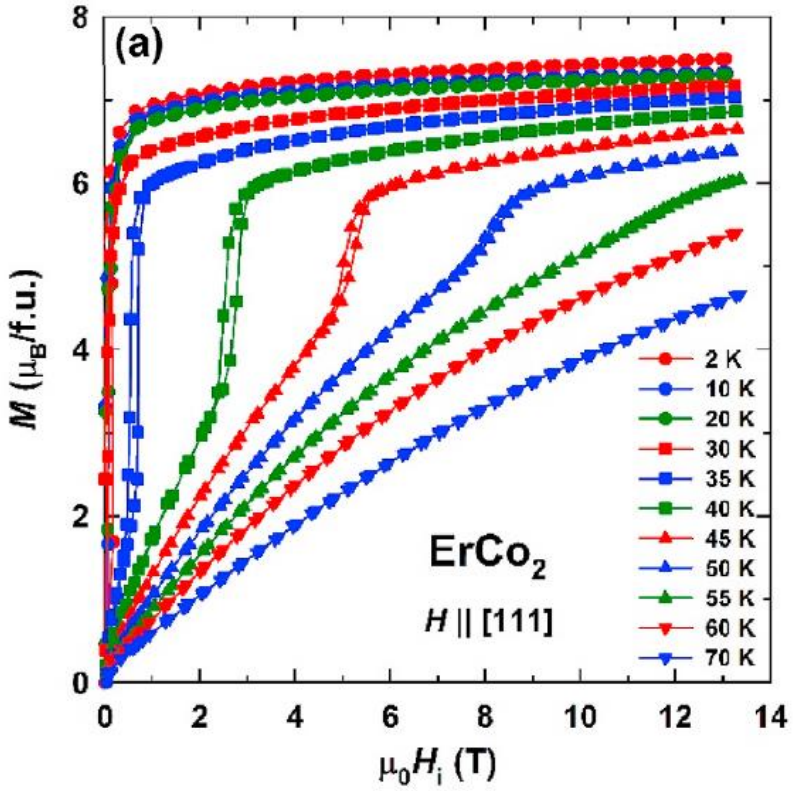

Fig. 1-11 Magnetization curves of $ErCo_2$ single crystal at various temperatures. The magnetic field is applied parallel to [111] axis [31].

Before direct observations of IEM in YCo_2 and $LuCo_2$, attempts to reduce B_C were made by substituting a third element for Co in YCo_2 and $LuCo_2$. Aleksandryan *et al*. found that substitution of a small amount of Al increases the Curie temperature T_C dramatically [32]. Yoshimura and Nakamura reported appearance of weak ferromagnetism in $Y(Co_{1-x}Al_x)_2$ with $0.12 < x < 0.20$ [33]. These two groups independently succeeded in observing IEM of $Y(Co_{1-x}Al_x)_2$ below 35 T [34, 35].

The substitution effect on magnetism of $LuCo_2$ have been studied by several groups [36-38]. The magnetic phase diagram of $Lu(Co_{1-x}Al_x)_2$ reported by Gabelko *et al*. is illustrated in Fig. 1-12 [36]. The compounds with $0 \le x < 0.07$ are paramagnetic. The B_C for IEM is decreased nearly linearly with increasing x and it goes down to zero at around $x = 0.09$.(not shown) A ferromagnetic state emerges in the concentration range of $0.08 \le x \le 0.22$. The Curie temperature shows a maximum value of 130 K at around $x = 0.15$. Fukamichi *et al.* examined IEM of $Lu(Co_{1-x}Al_x)_2$ with $0.085 \le x \le 0.095$ in details and constructed the magnetic phase diagram in the vicinity of the critical concentration for ferromagnetism [38]. This magnetic phase diagram can be understood by the theory of IEM by assuming that ac/b^2 decreases with x.

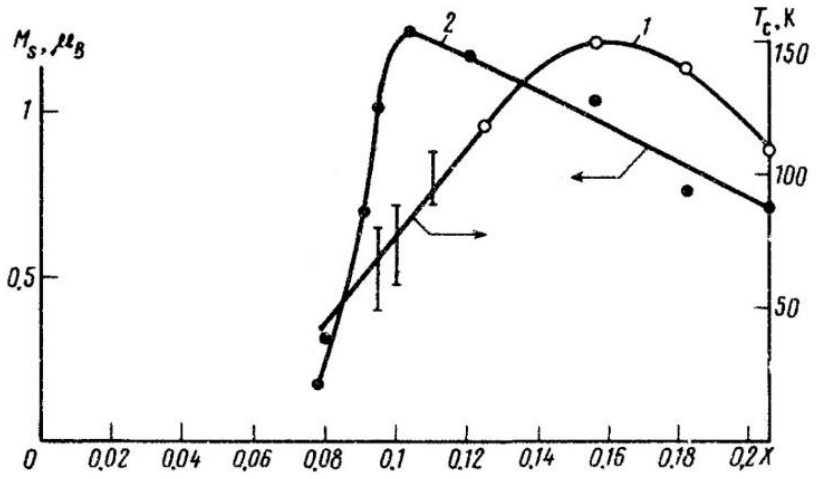

Fig. 1-12 Magnetic phase diagram of $Lu(Co_{1-x}Al_x)_2$ reported by Gabelko *et al.* [36].

1.5 $La(Fe_{1-x}Si_x)_{13}$

Ternary $La(Fe_{1-x}Si_x)_{13}$ compounds form the cubic $NaZn_{13}$-type structure in the concentration range of $0.10 \le x < 0.18$. Though no intermetallic compounds exist in the binary La-Fe system, a small amount of Si substitution stabilizes this structure. The crystal structure of $La(Fe_{1-x}Si_x)_{13}$ is shown in Fig. 1-13 [39]. The La atoms occupy the 8a site, which forms the simple cubic structure. The Fe atoms occupy two nonequivalent sites, 8*b* (denoted as FeI in the figure) and 96 *i* (FeII). Thus, the unit cell contains eight formula units. The Si atoms preferentially substitute for FeII site. The FeI are surrounded by an icosahedron of 12 FeII, and the FeII are surrounded by nine nearest FeII and one FeI. The magnetic phase diagram of $La(Fe_{1-x}Si_x)_{13}$ is depicted in Fig. 1-14 [12, 40]. All the $La(Fe_{1-x}Si_x)_{13}$ compounds are ferromagnetic and T_C increases from 190 K to 245 K with increasing x from 0.12 to 0.17. The magnetic transition at T_C is first order for $x \le 0.14$ and second order for $x > 0.14$. The IME is observed between T_0 and T_C.

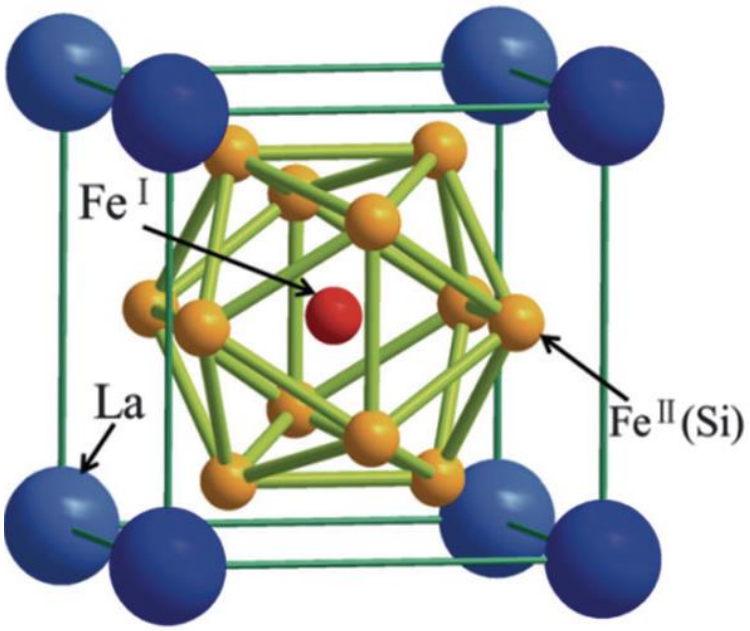

Fig. 1-13 Crystal structure of $La(Fe_{1-x}Si_x)_{13}$ ($NaZn_{13}$-type). The figure is taken from ref. 39.

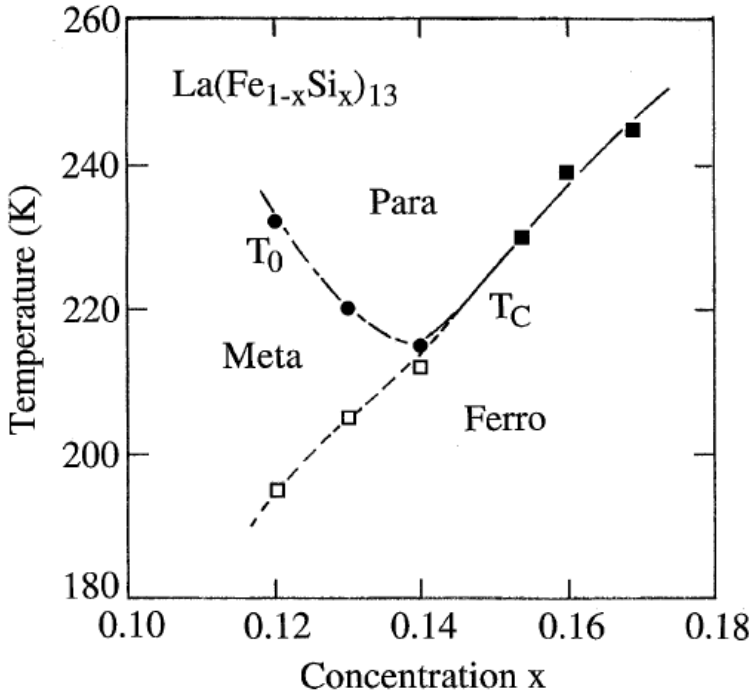

Fig. 1-14 Magnetic phase diagram of $La(Fe_{1-x}Si_x)_{13}$ [12, 40].

1.6 Hall effect

When the electric current is applied along the *x*-axis and the magnetic field $\boldsymbol{B} = (0, 0, B_z)$ is applied along the *z*-axis, the electric field is generated along the *y*-axis, as shown in Fig. 1-15. This is called the Hall effect.

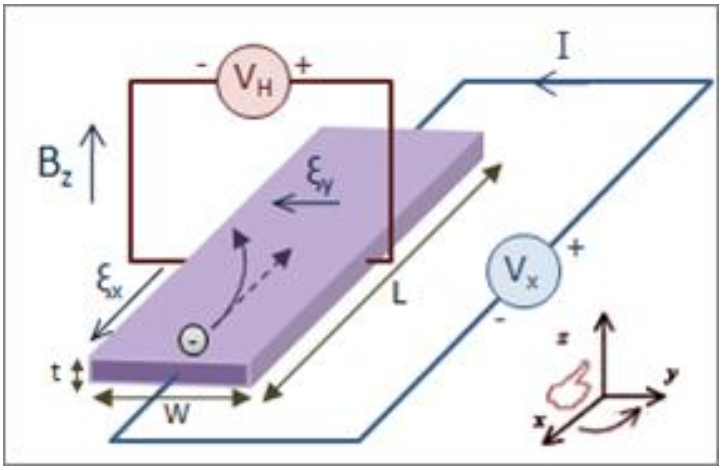

Fig. 1-15. Standard configuration of Hall effect. This figure is taken from ref. 41.

1.6.1 Normal (Ordinary) Hall effect (NHE)

The origin of Hall effect is Lorentz force. The charge carrier with an electric charge q feels a following Lorentz force $\boldsymbol{F}$ under an electric field $\boldsymbol{E}$ and a magnetic field $\boldsymbol{B}$,

$$\boldsymbol{F} = q\left(\boldsymbol{E} + \boldsymbol{v} \times \boldsymbol{B}\right). \qquad (1.12)$$

where $\boldsymbol{v}$ is a drift velocity. This force deflects the charge carriers in the y direction. The charge carriers are accumulated, which cause the electric field in the y direction, E_y. Eventually, the y component of $\boldsymbol{F}$ becomes zero, then, we have $E_y = v_x B_z$ .Since the electric current density i_x is given by $i_x = nqv_x$, respectively. where n is the charge carrier density, E_y is expressed as,

$$E_y = \frac{i_x B_z}{nq} = R_{\mathrm{N}} i_x B_z. \qquad (1.13)$$

This is the normal Hall effect (NHE) and $R_{\mathrm{N}} = 1/nq$ is called the normal Hall coefficient. E_y and i_x are related to the electric voltage along the *y*-axis V_y, and the electric current along the *x*-axis I_x as, $V_y = E_y w$ and $I_x = i_x wt$, where w and t are the width and thickness of the sample (see Fig. 1-15). So, we write,

$$\rho_{xy} = \frac{V_y t}{I_x} = R_{\mathrm{N}} B_z. \qquad (1.14)$$

The quantity ρ_{xy} is called the Hall resistivity. In the NHE, ρ_{xy} is proportional to a magnetic field.

Above results indicate R_N is negative, when the charge carriers are electrons, while $R_N > 0$ when they are holes. If both carriers contribute to the NHE, R_N is given by,

$$R_N = \frac{n_h \mu_h^2 - n_e \mu_e^2}{e\left(n_h \mu_h + n_e \mu_e\right)^2}, \qquad (1.15)$$

where n_h (n_e) is the hole (electron) density and μ_h (μ_e) is hole (electron) mobility. Thus, the sign of R_N depends not only on the carrier density but also on the carrier mobility.

Since the NHE is one of the transport properties, it is derived from the Boltzmann equation [42-44]. The electrical conductivity tensor is defined as,

$$j_\alpha = \sigma_{\alpha\beta} E_\beta + \sigma_{\alpha\beta\gamma} E_\beta E_\gamma + \cdots. \qquad (1.16)$$

Using the relaxation time approximation, $\sigma_{\alpha\beta}$ and $\sigma_{\alpha\beta\gamma}$ are given by,

$$\sigma_{\alpha\beta} = \frac{e^2}{4\pi^3\hbar} \iint \tau v_\alpha v_\beta \left(-\frac{\partial f}{\partial \varepsilon}\right) d\boldsymbol{k}, \qquad (1.17)$$

and,

$$\sigma_{\alpha\beta\gamma} = -\frac{e^3}{4\pi^3\hbar} \int \tau^2 \left(-\frac{\partial f}{\partial \varepsilon}\right) v_\alpha \cdot \left(\boldsymbol{v} \times \nabla\right)_\gamma v_\beta d\boldsymbol{k}. \qquad (1.18)$$

with the Fermi-Dirac distribution function f, the relaxation time τ. Here $\boldsymbol{v}$ means the group velocity of electrons, which is given by $\boldsymbol{v} = \frac{1}{\hbar}\left(\frac{d\varepsilon}{d\boldsymbol{k}}\right)_{\varepsilon=\varepsilon_F}$. In weak magnetic fields, the nomal Hall coefficient is expressed as,

$$R_N = \frac{\sigma_{xyz}}{\sigma_{xx}\sigma_{yy}}, \qquad (1.19)$$

in the setup of Fig. 1-15. If τ is independent of $\boldsymbol{k}$, R_N does not include τ in its form. This is called the τ constant approximation. In this case, R_N can be estimated from the energy band calculations.

1.6.2 Anomalous (Extraordinary) Hall effect (AHE)

The Hall resistivity of ferromagnetic materials is quite different from that expected from eq. (1.14). As shown in Fig. 1-16, ρ_{xy} shows a rapid rise initially with increasing field, followed by a linear variation at high fields. This field dependence of ρ_{xy} is well expressed by a following equation [42, 45],

$$\rho_{xy} = R_{\mathrm{N}} B + R_{\mathrm{A}} M. \qquad (1.20)$$

The first term is the NHE described in the previous subsection. The second term is termed the anomalous (extraordinary) Hall effect (AHE), which is proportional to the magnetization. The proportional coefficient R_{A} is called the anomalous Hall coefficient. The AHE is observed not only in ferromagnets but also in paramagnets and in antiferromagnets, when they have large magnetic moments.

The origin of AHE can be classified into the extrinsic effect and the intrinsic effect. The former is based on the concept in which ρ_{xy} should arise from the impurity scattering, because the lattice imperfection is responsible for the resistivity. Smit pointed out that conduction electrons can be scattered asymmetrically from a magnetic impurity potential depending on the spin direction, when the spin-orbit interaction is taken into account [46, 47]. This is called the skew scattering and is schematically shown in Fig. 1-17(a). The electrons with up-spin are deflected to the right more than to the left and vice versa for down-spin. It is suggested that for the skew scattering mechanism, the Hall resistivity varies linearly with the conventional electrical resistivity, $\rho_{xy} \propto \rho_{xx}$. On the other hand, Berger proposed the side jump mechanism [48, 49]. When a wave packet of a conduction electron is scattered from a spherical impurity with the spin-orbit interaction, the trajectory of the electron is shifted depending on the spin direction, as shown in Fig. 1-17(b). The side jump mechanism predicts quadratic ρ_{xx} dependence of ρ_{xy}, $\rho_{xy} \propto \rho_{xx}^2$. The intrinsic mechanism of AHE was first discussed by Karplus and Luttinger in 1954 [50]. Due to the spin-orbit interaction, the electrons have an anomalous velocity perpendicular both to the electric field and to the direction of magnetization. The sum of the anomalous velocity over all occupied band states can be nonzero, giving AHE. The anomalous velocity of magnetic Bloch electrons is now related to Berry phase and the intrinsic AHE is given by the integral of the Berry curvature over all occupied Bloch states [51]. The intrinsic AHE predicts $\rho_{xy} \propto \rho_{xx}^2$, which has the same scaling law with that of the side jump mechanism.

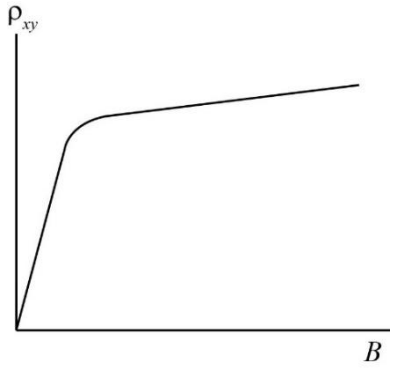

Fig. 1-16 Typical behavior of field dependence of Hall resistivity of ferromagnetic materials.

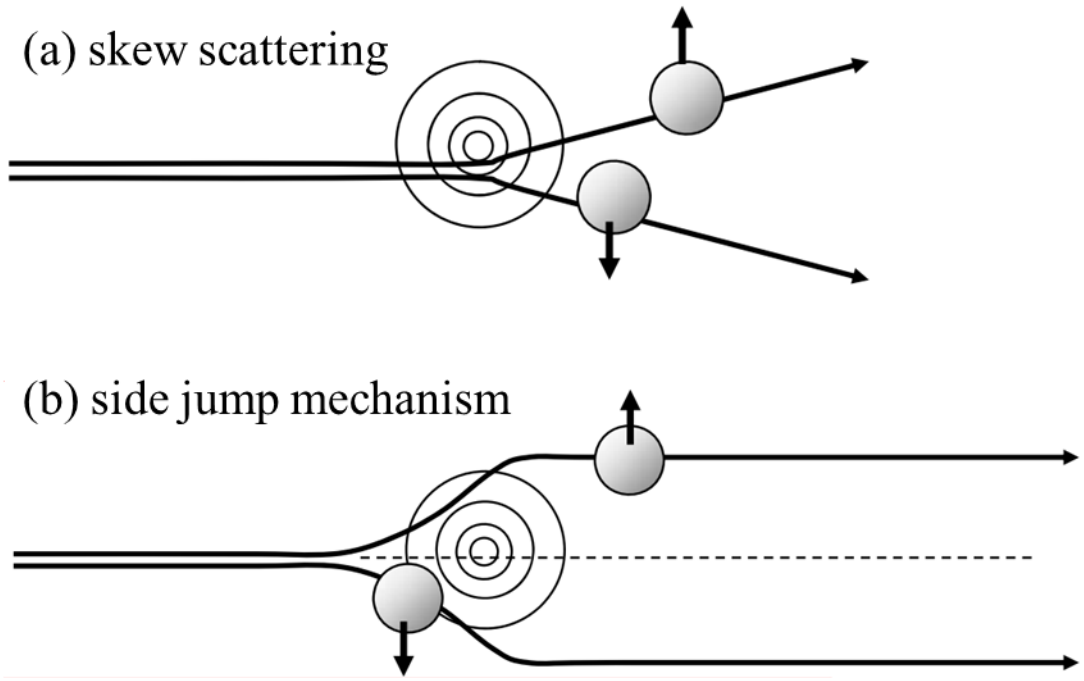

Fig. 1-17 (a) Skew scattering. (b) Side jump mechanism. This figure is taken from ref. 51.

1.7 Aims of the thesis

As described before, IEM provides a unique stage to investigate the electronic structures of the ferromagnetic and paramagnetic states, because both states appear at the same temperature. In this study, we examine Hall effect of itinerant electron metamagnets. As mentioned in the previous section, ferromagnets exhibit characteristic $\rho_{xy} - B$ curves shown in Fig. 1-16. Then, the NHE and AHE can be evaluated. In the case of paramagnets, on the other hand, both the NHE and AHE are proportional to B, because the magnetization can be expressed as $M = \chi_p B$, where χ_p is a paramagnetic susceptibility. This makes it difficult to estimate the NHE and AHE in the paramagnetic state. In IEM, both the ferromagnetic and paramagnetic states are realized depending on a magnetic field. We notice that this may enable us to estimate the NHE and AHE in the paramagnetic state by using R_A in the ferromagnetic state. In the present study, we measured the field dependence of Hall resistivity of IEM systems, $Co(S_{1-x}Se_x)_2$, $Lu(Co_{1-x}Al_x)_2$, $ErCo_2$, and $La(Fe_{1-x}Si_x)_{13}$. The data are analyzed in various ways and obtained R_N in the paramagnetic state as well as in the ferromagnetic state. Furthermore, we compare R_N's determined from experiments with those obtained from the energy band calculations.

Chapter 2 Experimental details

2.1 Sample preparation

Polycrystalline $Co(S_{1-x}Se_x)_2$ samples were synthesized by solid state reaction. Powders of Co (purity: 99.9 %), S (99.9999 %), and Se (99.999 %) were weighted in appropriate compositions. The initial compositions of synthesized samples were x = 0.08, 0.10, 0.11, 0.12, 0.13, and 0.14. The powder mixture put in an alumina crucible was sealed in an evacuated quartz tube and heated at 250 °C for two days and at 400 °C for five days for a preliminary heat treatment. Subsequently, the resultant products were pulverized, mixed, and pressed into a pellet under a pressure of 200kgf/cm^2. The pellet was heated for two days at 700 °C in an evacuated quartz tube. The samples were checked by powder X-ray diffraction with Fe $K\alpha$ radiation. Figure 2.1 shows X-ray diffraction patterns of $Co(S_{1-x}Se_x)_2$. No foreign phase other than the Pyrite structure was detected in each X-ray diffraction pattern. The lattice parameters obtained from the X-ray diffraction measurements are shown as a function of x in Fig. 2-2. They are in agreement with the previous results [52] and approximately obey Vegard's law.

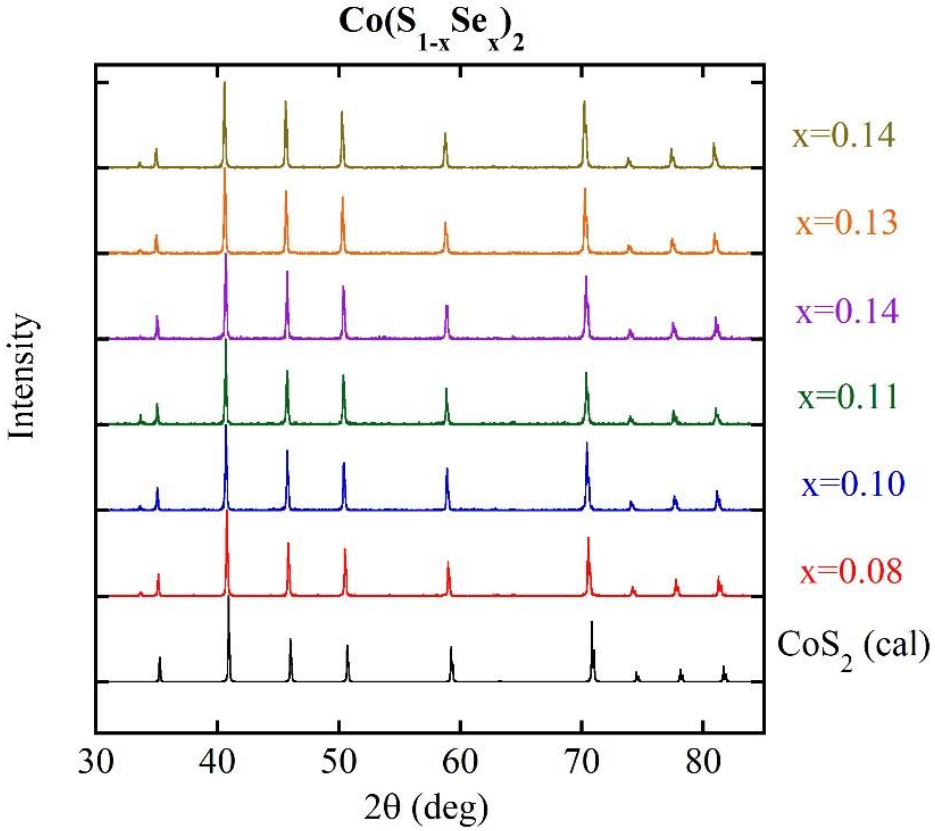

Fig. 2-1 X-ray diffraction patterns of $Co(S_{1-x}Se_x)_2$. The calculated pattern for CoS_2 is also shown at the bottom.

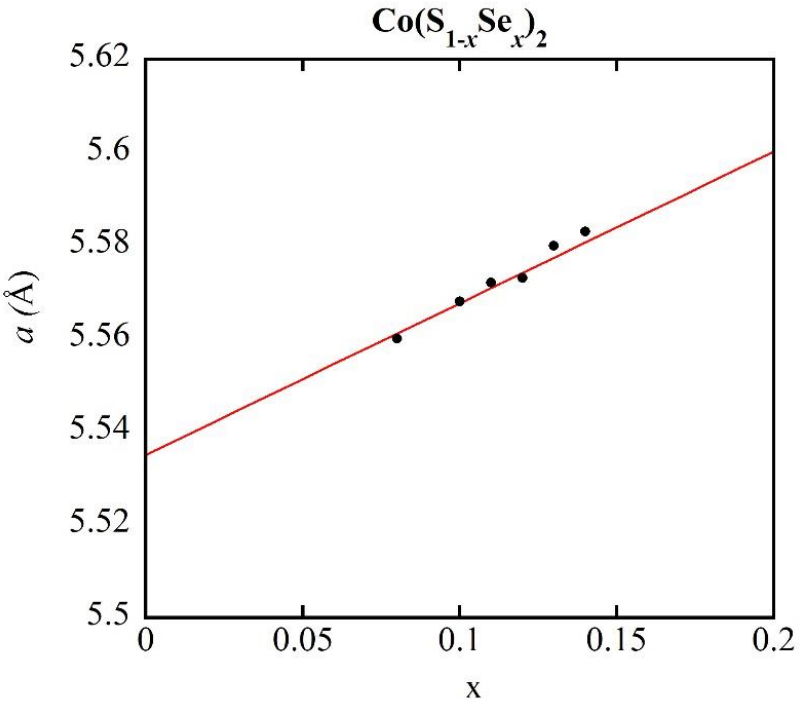

Fig. 2-2 Concentration dependence of the lattice parameter of $Co(S_{1-x}Se_x)_2$. A red line represents Vegard's law taken from ref. 52.

In the study of RCo_2, we used $ErCo_2$ single crystals and $Lu(Co_{1-x}Al_x)_2$ polycrystalline samples for the measurements. Single crystals of $ErCo_2$ was grown by a modified Czochralski method in a tri-arc furnace using Er (99.9%) and Co (99.99%) at Institute of Physics of the Czech Academy of Science, Prague. The pulling of crystal was performed under in an argon atmosphere. A tungsten rod was used as a seed, and the pulling speed was 10 mm/h. The initial composition was taken as $ErCo_{1.96}$. Back-scattered Laue diffraction patterns confirmed the single-crystalline state of the samples. Polycrystalline $LuCo_2$ and $Lu(Co_{0.91}Al_{0.09})_2$ were prepared by arc-melting constituents in an argon atmosphere. The purities of constituents are 99.9% for Lu and Co, and 99.99% for Al. In the binary Lu-Co phase diagram, ferromagnetic $LuCo_3$ exists as an adjacent phase of $LuCo_2$. The Laves phase is formed by a peritectic reaction. To avoid the contamination of $LuCo_3$, we used Lu-rich initial compositions of Lu:(CoAl) = 35:65. To ensure homogeneity, we turned the batch upside down and melted it several times. The ingot was wrapped in a Ta foil and then it was sealed in an evacuated quartz tube for annealing. $LuCo_2$ was annealed at 900 °C for seven days, while $Lu(Co_{0.91}Al_{0.09})_2$ was annealed at 1050°C for seven days. Yokoyama *et al.* reported that annealing condition is crucial to achieve sharp IEM in $Lu(Co_{1-x}Al_x)_2$ [53]. Then, we chose a higher annealing temperature of 1050°C for $Lu(Co_{0.91}Al_{0.09})_2$. X-ray diffraction patterns of $LuCo_2$ and $Lu(Co_{0.91}Al_{0.09})_2$ are displayed in Fig. 2-3. It is found that these samples have the C15 Laves phase structure. A small amount of Lu_2O_3 was detected as an impurity phase (shown by arrows in Fig. 2-3). The lattice parameters of $LuCo_2$ was and $Lu(Co_{0.91}Al_{0.09})_2$ are 7.103 Å and 7.150 Å, respectively. These values are in agreement with the previous reports [54].

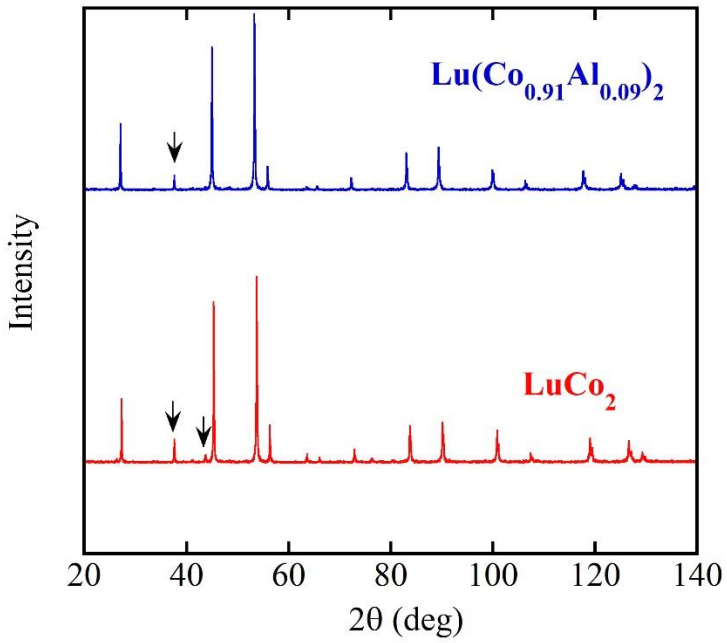

Fig. 2-3 X-ray diffraction patterns of $LuCo_2$ and $Lu(Co_{0.91}Al_{0.09})_2$. Arrows indicate the diffraction peaks due to Lu_2O_3 impurity phase.

The $La(Fe_{1-x}Si_x)_{13}$ compounds with x = 0.10 and 0.12 were prepared by arc-melting constituents with the stoichiometric compositions in an argon atmosphere. The purities of the raw materials are 99.9% for La, 99.9% for Fe and 99.999% for Si. The ingot was turned upside down and melted, again. This procedure was repeated for several times. The product was wrapped in a Ta foil and then it was sealed in an evacuated quartz tube for a heat treatment. Since La and Fe are immiscible in a solid state, it is necessary to anneal an ingot at high temperatures for a long time to obtain a desired compound with the $NaZn_{13}$-type structure. Then, the sample were kept at 1050°C for ten days. The X-ray diffraction patterns of $La(Fe_{1-x}Si_x)_{13}$ are shown in Fig. 2-4. Most of diffraction peaks can be indexed to the cubic $NaZn_{13}$-type structure. For both x = 0.10 and 0.12, an extra peak is observed at around 2θ = 57° (shown by the arrow), which is assigned to the α-Fe(Si) phase (Si can be incorporated into α-Fe). Since α-Fe(Si) is ferromagnetic, the presence of α-Fe(Si) phase gives some impacts on magnetic properties of $La(Fe_{1-x}Si_x)_{13}$. This problem will be discussed in Chapter 5.

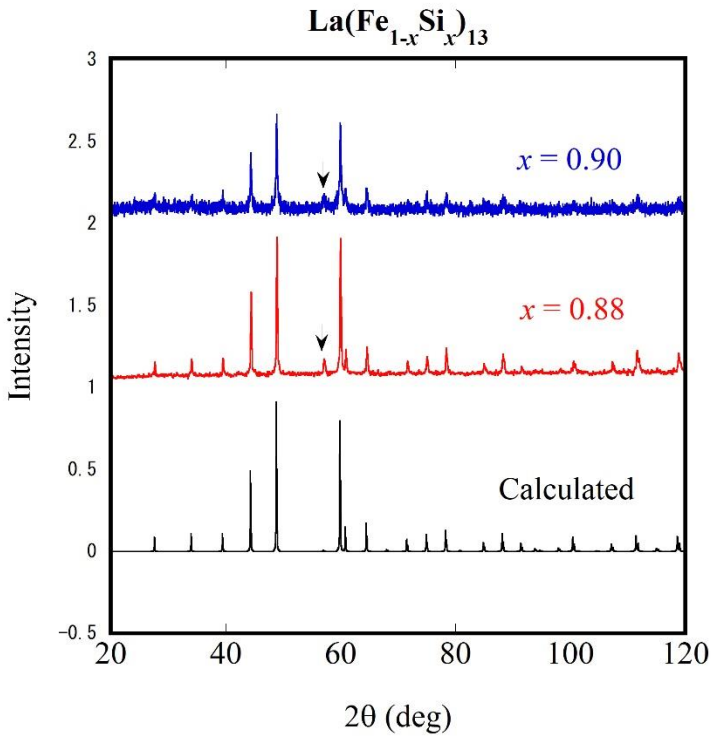

Fig. 2-4 X-ray diffraction patterns of $La(Fe_{1-x}Si_x)_{13}$ with x = 0.10 and 0.12. The calculated pattern is also shown. Arrows indicate the diffraction peaks due to α-Fe(Si) impurity phase.

2.2 Magnetization measurements

Magnetization measurements were carried out using a commercial superconducting quantum interference device (SQUID) magnetometer (Quantum Design MPMS) up to 7 T at a constant temperature. For some samples, magnetization was measured at high pressures using a CuBe piston–cylinder cell. Daphne 7474 oil was used as a pressure-transmitting medium.

2.3 Hall effect measurements

Hall effect was measured by an ac four probe method in a standard configuration, in which the electric current I is applied along the $+x$ direction, the magnetic field B is applied along the $+z$ direction and the Hall voltage was measured along the $-y$ direction (Fig. 2-5). The sample was shaped into a plate of dimensions 1~2 (l) × 1 (w) × 0.3~0.5 (t) mm. Four platinum wires with 50μm diameter were contacted with silver conductive epoxy. The sample was fixed by Apiezon N grease to the sample stage. The sample stage was inserted to the variable temperature insert (VTI) and it was situated at the central position of magnetic field.

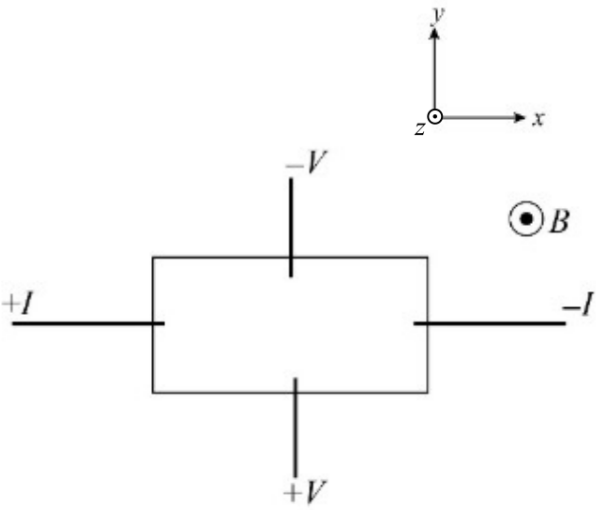

Fig. 2-5 Schematic setup for Hall effect measurements.

The block diagram of Hall effect measurements is illustrated in Fig. 2-6. The field dependence of Hall resistivity was measured up to 12 T at a constant temperature. The temperature was roughly controlled by a VTI temperature controller (Oxford ITC 503). Precise temperature control was achieved by PID temperature controller (Lake Shore Model 331) with a heater and a Cernox thermometer mounted on the sample stage. The temperature stability was controlled at a fixed temperature within ±0.1 K during the measurements. The Hall resistivity was measured with an ac resistance bridge (Linear Research LR-700), of which excitation frequency is 16 Hz. The measured voltage V includes not only the Hall voltage V_{xy} but also the longitudinal voltage V_{xx} due to a small misalignment of terminals. To obtain V_{xy} correctly, we first measured V_+, which is the voltage with B applied along the $+z$ direction. Then, we measured V_- with B along the $-z$ direction at the same temperature. The Hall voltage was calculated from $V_{xy} = (V_+ - V_-)/2$. The Hall resistivity ρ_{xy} is given by $\rho_{xy} = V_{xy}t/I$, where t is the thickness of the sample. On the other hand, V_{xx} is given by $(V_+ + V_-)/2$. The resistance $r_{xx} = V_{xx}/I$ is proportional to the longitudinal resistivity ρ_{xx}. Electric appliances are connected to a personal computer via a GPIB bus that enables for their remote control with LabVIEW software. In the present study, we measured the $\rho_{xy} - B$ curves in the field-increasing process except $La(Fe_{1-x}Si_x)_{13}$. The measurements for $La(Fe_{1-x}Si_x)_{13}$ were carried out for both field-increasing and field- decreasing processes. The field sweep rate was 0.5-1.0 T/min.

Measurements at high pressures were carried out in a double-layered CuBe/NiCrAl cell. Daphne 7474 oil was used as a pressure-transmitting medium. For Hall effect measurements, the sample glued on a Bakelite stage was placed into a Teflon cell, which was inserted into a cylinder cell. The relation between actual pressure and pressure load was obtained from pressure dependence of superconducting transition of tin, beforehand. Hall resistivity measurements using a pressure cell is useful to fix a sample tightly in strong magnetic fields. This is important when the sample has large magnetization. Then, we used a pressure cell for the Hall resistivity measurements of $ErCo_2$ at ambient pressure.

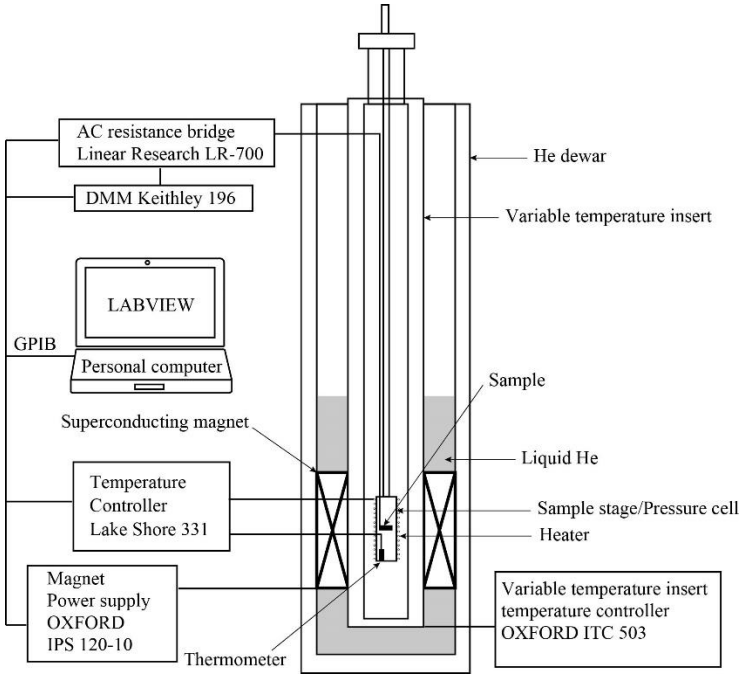

Fig. 2-6 Block diagram of Hall effect measurements.

2.4 Energy band calculations

For CoS_2, $CoSe_2$, and $LuCo_2$, the electronic structure was calculated in collaboration with The Institute of Scientific and Industrial Research (SANKEN), Osaka University. The electronic states were calculated by using the all-electron full-potential linearized-augmented-plane-wave (FLAPW) program package HiLAPW [55]. These calculations were performed using LDA exchange-correlation potential [56], LAPW basis set with the scalar-relativistic scheme, and the improved tetrahedron integration method up to 16×16×16 $\boldsymbol{k}$-mesh points in the Brillouin zone [57]. The calculated energy dispersion was fitted with symmetrized star functions by a spline method with 64×64×64 $\boldsymbol{k}$-mesh points and used for calculations of the Fermi surfaces, the Fermi velocity and the Hall coefficients [44]. The Fermi surfaces were drawn by using FermiSurfer program [58]. The normal Hall coefficients were evaluated by using eqs. (1.17) - (1.19).

Chapter 3 Results and discussion on $Co(S_{1-x}Se_x)_2$

3.1 Experimental results and analyses

Figure 3-1 shows the isothermal magnetization curves of $Co(S_{1-x}Se_x)_2$ compounds at 4.2 K or 5 K. The data with increasing field are shown. The magnetization of x = 0.08 and 0.10 is saturated above 1 T, indicating that they are ferromagnetic at low temperatures. On the other hand, the compounds with $x \geq 0.11$ are paramagnetic with no spontaneous magnetization in the ground state. IEM is observed for $0.11 \leq x \leq 0.13$ below 7 T.

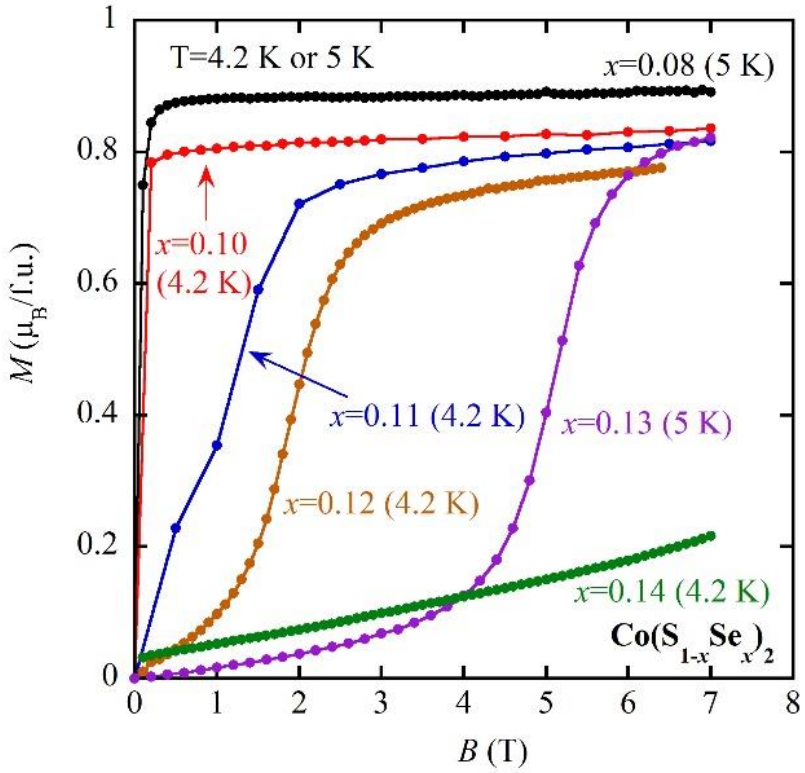

Fig. 3-1 Isothermal magnetization curves of $Co(S_{1-x}Se_x)_2$ compounds with $0.08 \leq x \leq 0.14$ at 4.2 or 5 K. Data with increasing field are shown. Solid lines are guide to the eye.

The magnetization curves of x = 0.10 and 0.11 at various temperatures are displayed in Figs. 3-2 (a) and 3-2 (b), respectively. The T_C of x = 0.10 is about 55 K, so that the $M - B$ curve at 70 K exhibits itinerant electron metamagnetic behavior. For x = 0.11, on the other hand, IEM is observed in the whole temperature range below 60 K. A small ferromagnetic component is observed for x = 0.11 at low fields. This is probably due to concentration fluctuations, because ferromagnetism appears in the vicinity of x = 0.11.

The field dependence of the Hall resistivity of $Co(S_{1-x}Se_x)_2$ at 4.2 K is illustrated in Fig. 3-3. In the ferromagnetic state, a rapid fall of ρ_{xy} was found at low fields. This is attributable to the AHE. Therefore, the AHE is negative in the present system. Above the technical saturation, ρ_{xy} increases nearly linearly with

increasing magnetic field. The $\rho_{xy} - B$ curves with $0.11 \leq x \leq 0.13$ can be divided into three regions: the paramagnetic region, the transitional region near the transition field of IEM B_C, and the ferromagnetic region. In the paramagnetic region at low fields, ρ_{xy} decreases with increasing field. In the transitional region, the Hall resistivity suddenly drops due to the AHE. And ρ_{xy} increases linearly with magnetic field in the ferromagnetic region at high fields.

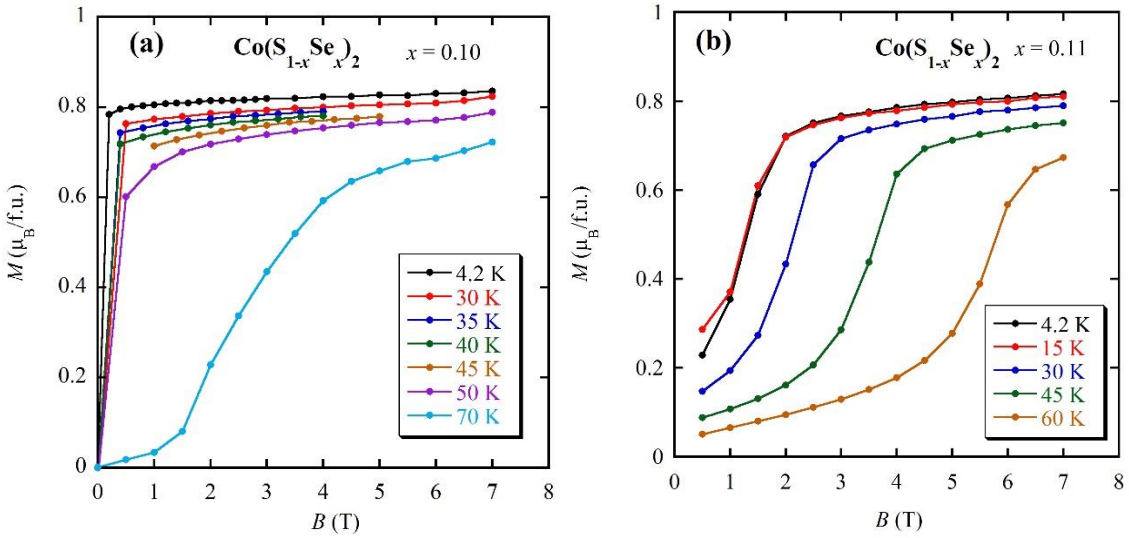

Fig. 3-2 The magnetization curves of $Co(S_{1-x}Se_x)_2$ at various temperatures for $x = 0.10$ (a) and $x = 0.11$ (b).

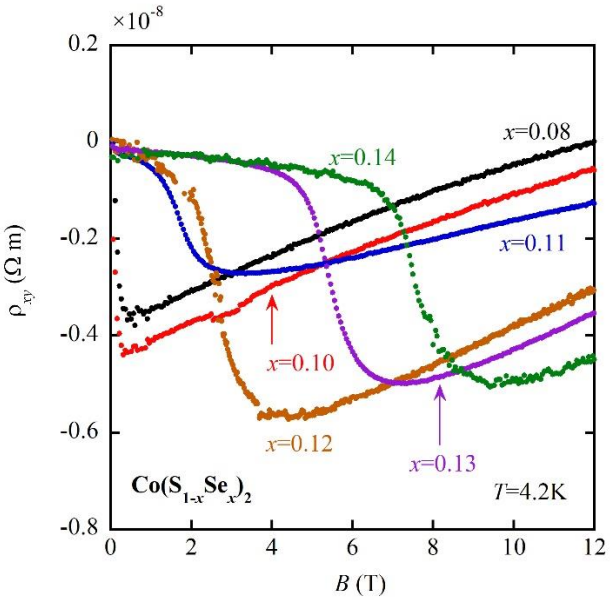

Fig. 3-3 Field dependence of the Hall resistivity ρ_{xy} of $Co(S_{1-x}Se_x)_2$ compounds with $0.08 \leq x \leq 0.14$ at 4.2 K.

The $\rho_{xy} - B$ curves of $x = 0.10$ and 0.11 at various temperatures are depicted in Figs. 3-4 (a) and 3-4 (b), respectively. The field dependence of ρ_{xy} of $x = 0.10$ at $T \leq 50$ K shows ferromagnetic behavior. The $\rho_{xy} - B$ curves at $T \geq 60$ K are characterized by the three regions mentioned above. The magnitude of AHE increases with increasing temperature. On the other hand, the slope of ρ_{xy} is weakly dependent on temperature between 4.2 K and 60 K. The compound with $x = 0.11$ exhibits IEM below 75 K. With increasing temperature, B_C is increased and the transition becomes broader. Each $\rho_{xy} - B$ curve has a negative slope below B_C and a positive slope above B_C. The negative jump of ρ_{xy} at around B_C increases with increasing temperature. The positive slope in the ferromagnetic region is not sensitive to temperature below 30 K. These trends are similar to $x = 0.10$.

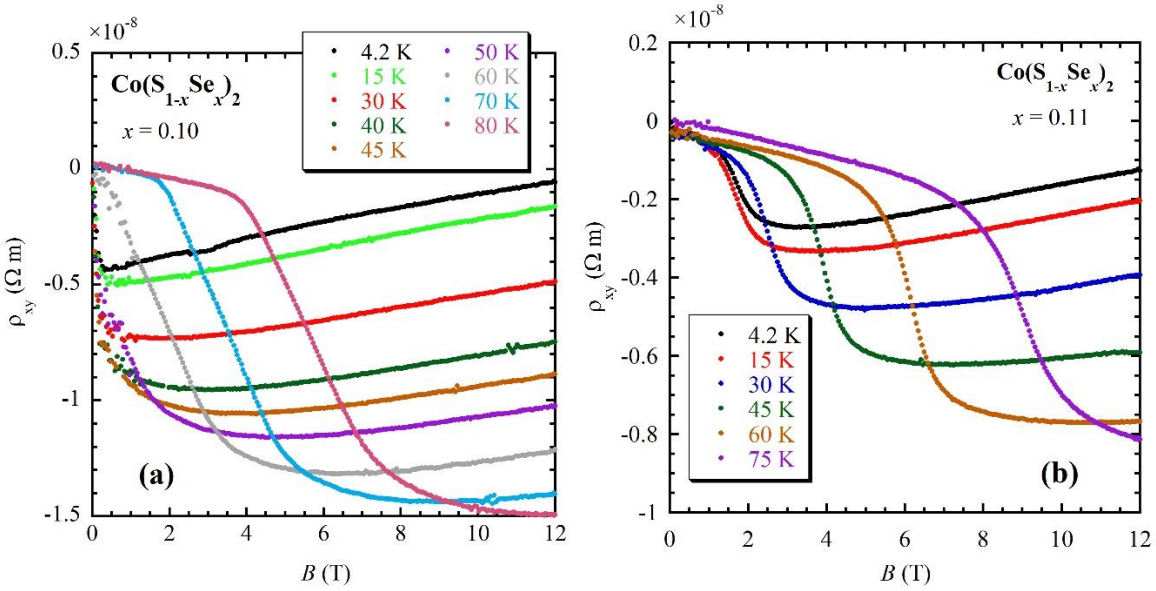

Fig. 3-4 The $\rho_{xy} - B$ curves of $Co(S_{1-x}Se_x)_2$ at various temperatures for $x = 0.10$ (a) and $x = 0.11$ (b).

In the following, we analyze the Hall resistivity of $Co(S_{1-x}Se_x)_2$.

As shown in eq. (1.19), the Hall resistivity of magnetic materials is expressed as,

$$\rho_{xy} = R_N B + R_A M, \qquad (3.1)$$

where R_N and R_A are the normal and anomalous Hall coefficients, respectively. Since IEM is accompanied by abrupt band splitting, R_N depends on the magnetic state. Then, we define $R_N{}^f$ and $R_N{}^p$ as R_N in the ferromagnetic state and that in the paramagnetic state, respectively. We assume that R_A is independent of the magnetic state. The validity of this assumption will be discussed later. Obviously, R_A is negative in the present system. The positive slope of the $\rho_{xy} - B$ curves in the ferromagnetic state indicates $R_N{}^f > 0$, because the AHE has a negative contribution. On the other hand, the $\rho_{xy} - B$ curves have negative slopes in the paramagnetic state. Since the AHE is negative, the sign of $R_N{}^p$ is not determined at this stage.

In the ferromagnetic state, the magnetization curve is approximated as,

$$M = M^0 + \chi_{hf} B, \qquad (3.2)$$

where M_0 is the spontaneous magnetization and χ_{hf} the high-field magnetic susceptibility. The Hall resistivity in the ferromagnetic state is also written in the first approximation as,

$$\rho_{xy} = \rho_{xy}^0 + R_{obs} B, \qquad (3.3)$$

where $\rho_{xy}{}^0$ and R_{obs} are the intercept and slope of the $\rho_{xy} - B$ curve, respectively. Putting eq. (3.2) into eq. (3.1) and comparing it with eq. (3.3), we have,

$$R_N^f = R_{obs} - R_A \chi_{hf}, \qquad (3.4)$$

$$R_A = \rho_{xy}^0 / M^0. \qquad (3.5)$$

Using these relations, we can estimate $R_N{}^f$ from the experimental results.

As shown in Fig. 1-7, χ_{hf} of $Co(S_{1-x}Se_x)_2$ at 4.2 K is very small. Very small χ_{hf} is consistent with the results of electronic structure calculations on CoS_2. As described later, our electronic structure calculations show that the ferromagnetic CoS_2 is half metallic. These results are in agreement with the previous reports [59, 60]. This means that further band splitting is not induced by a magnetic field for CoS_2 at $T = 0$. Moreover, ultrahigh-resolution photoemission spectroscopy of CoS_2 and $Co(S_{0.925}Se_{0.075})_2$ has revealed that the substitution of Se for S does not change the band structure considerably [61, 62]. Therefore, we can approximate $\chi_{hf} \sim 0$ at 4.2 K for ferromagnetic $Co(S_{1-x}Se_x)_2$. In this case, $R_N{}^f$ is given by R_{obs}. The $R_N{}^f$ values of $Co(S_{1-x}Se_x)_2$ with $0.08 \le x \le 0.13$ at 4.2 K are listed in Table 3-1. For $x = 0.14$, it is difficult to estimate R_{obs} in the ferromagnetic state accurately, because of the narrow ferromagnetic region (see Fig. 3.3). It is found that $R_N{}^f$ is in the range of 31-39 $\times 10^{-11}$ m^3/C except $x = 0.11$. These results may suggest that $R_N{}^f$ of $Co(S_{1-x}Se_x)_2$ is weakly dependent on the Se concentration for $0.08 \le x \le 0.13$.

Table 3-1 The normal Hall coefficients $R_N{}^f$ and $R_N{}^p$ of $Co(S_{1-x}Se_x)_2$ at 4.2 K.

x	0.08	0.10	0.11	0.12	0.13	0.14
$R_N{}^f$ (10^{-11} m^3/C)	36.7	31.4	19.2	38.9	38.3	
$R_N{}^p$ (10^{-11} m^3/C)					12.2	14.6

At temperatures higher than 4.2 K, we estimated $R_N{}^f$ from eqs. (3.4) and (3.5). Since the maximum field of magnetization measurements is 7 T, we cannot evaluate χ_{hf} for $x \geq 0.12$ at any temperature with satisfactory accuracy. Thus, $R_N{}^f$ for $0.08 \leq x \leq 0.11$ was obtained. The results are shown in Fig. 3-5 as a function of temperature. It is found that $R_N{}^f$ exhibits weak temperature dependence. As shown in Figs. 3-4 (a) and 3-4 (b), R_{obs} in the ferromagnetic state is not sensitive to temperature for both $x = 0.10$ and 0.11. These results indicate that the anomalous Hall term $R_A\chi_{hf}$ is much smaller than $R_N{}^f$ in eq. (3.4).

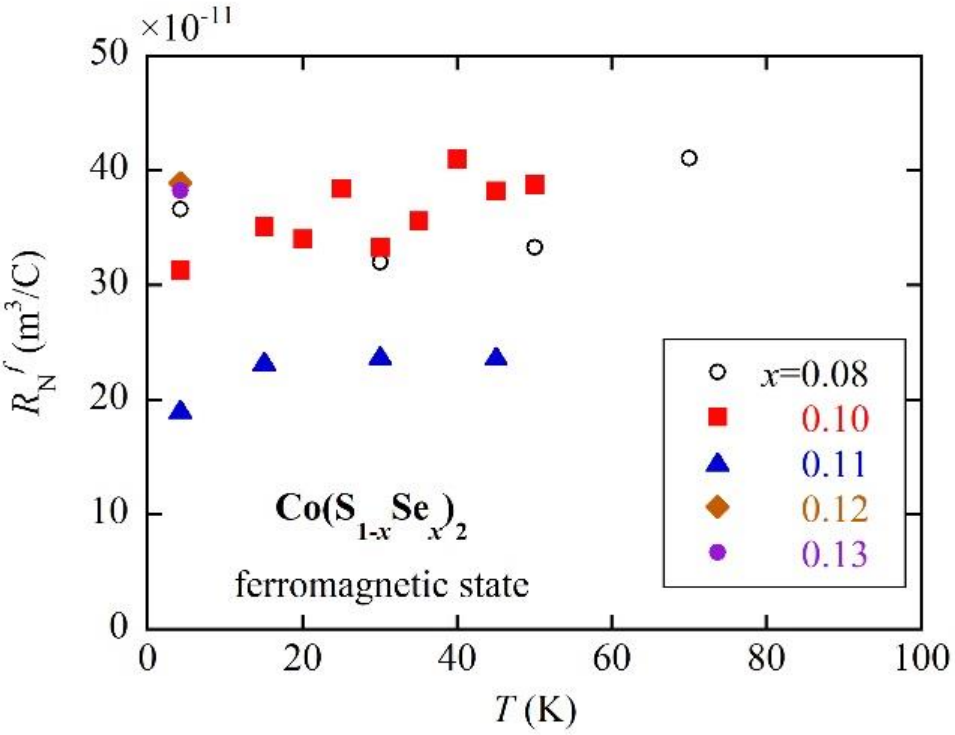

Fig. 3-5 Temperature dependence of $R_N{}^f$ of $Co(S_{1-x}Se_x)_2$ with $0.08 \leq x \leq 0.11$.

Next, we analyze the $\rho_{xy} - B$ curves in the paramagnetic state. Well below B_C, both M and ρ_{xy} are nearly proportional to a magnetic field. Then, we can write M and ρ_{xy} in the paramagnetic state as,

$$M = \chi_p B, \qquad (3.6)$$

$$\rho_{xy} = R_{obs} B, \qquad (3.7)$$

where χ_p means the paramagnetic susceptibility. Putting eq. (3.6) into eq. (3.1) and comparing it with eq. (3.7), we have,

$$R_N^p = R_{obs} - R_A\chi_p. \qquad (3.8)$$

Note that R_{obs} and χ_p are obtained from the $\rho_{xy} - T$ and $M - T$ curves in the paramagnetic state,respectivery, while R_A from those in the ferromagnetic state. Therefore, both magnetic states are necessary at the same temperature for this analysis. We emphasize that IEM can provide this situation. At 4.2 K, we obtained R_{obs} in the paramagnetic state and χ_p for $x = 0.13$ and 0.14. Here, a small ferromagnetic component at low fields in the $M - B$ curve of $x = 0.14$ was eliminated. The magnetization curve of $x = 0.14$ does not show metamagnetic behavior up to 7 T (see Fig. 3-1). Then, we use the $M - B$ curve of $x = 0.14$ reported by Goto *et al*. to determine M^0 [15]. The $R_N{}^p$ values of $x = 0.13$ and 0.14 at 4.2 K are also listed in Table 3-1. The analyses revealed that $R_N{}^p$ is positive for these compounds. Their values are slightly smaller than $R_N{}^f$. This implies that $R_A\chi_p$ is dominant in R_{obs} due to large χ_p in the paramagnetic state. We also estimated $R_N{}^p$ of some compounds above 4.2 K. The temperature dependence of $R_N{}^p$ for $0.11 \le x \le 0.14$ is depicted in Fig. 3-6. Though a few data of $R_N{}^p$ are available, the results suggest that $R_N{}^p$ is 10-20 $\times 10^{-11}$m^3/C for $0.11 \le x \le 0.14$ below 60 K.

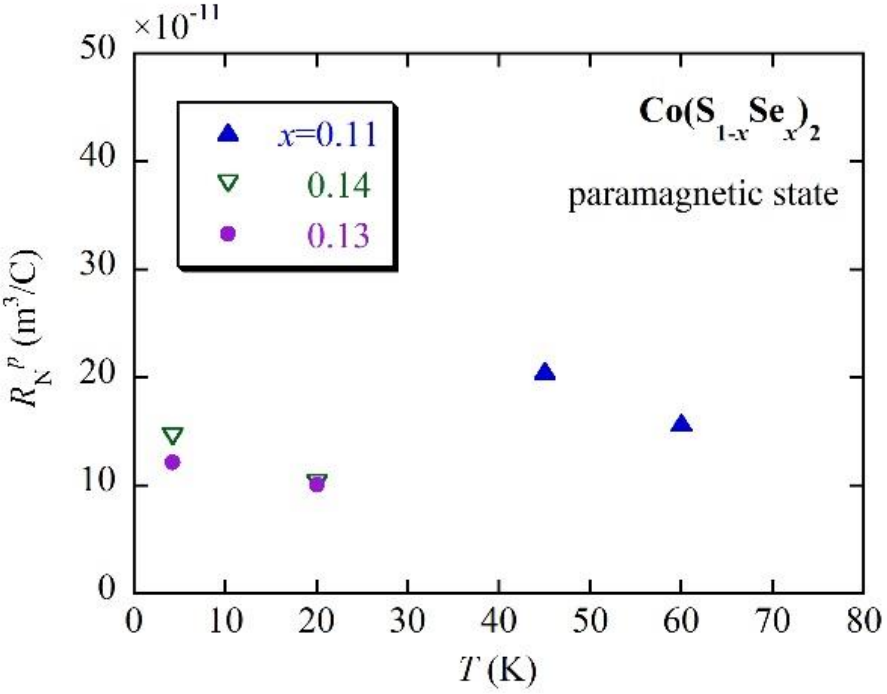

Fig. 3-6 Temperature dependence of $R_N{}^p$ of $Co(S_{1-x}Se_x)_2$ with $0.11 \le x \le 0.14$.

As, described before, we assumed that R_A in the ferromagnetic state is equal to that in the paramagnetic state in the present analyses. We now discuss the validity of this assumption. The AHE originates in the impurity scattering, such as skew scattering or side jump mechanism, and the intrinsic effect, which is expressed by an integral of the Berry curvature in the momentum space. It seems reasonable to assume that R_A is independent of magnetic state when the impurity scattering is dominant in the AHE. In our experiments, R_A shows strong sample dependence. For example, a different sample with $x = 0.12$ has R_A that is less than one third of that of the sample shown in Fig. 3-3. Similar sample dependence of AHE was also observed for ferromagnetic CoS_2 [63]. These results strongly suggest that the AHE originates in the impurity scattering, such as skew scattering

or side jump mechanism. The longitudinal resistivity ρ_{xx} dependence of the anomalous Hall resistivity ρ_{xy}^0 is a good measure to clarify the origin of AHE. As described in 1.6.1, the skew scattering predicts $\rho_{xy} \propto \rho_{xx}$, while the side jump mechanism and the Berry curvature contribution are expected to show $\rho_{xy} \propto \rho_{xx}^2$. In the present study, ρ_{xx} has not been measured. However, we notice that r_{xx}, which is calculated from $V_{xy} = (V_+ + V_-)/2$, is available instead of ρ_{xx}. Moreover, field dependence of r_{xx} is obtained, which enables us to estimate r_{xx} in the ferromagnetic state. It is known that r_{xx} shows a jump at B_C. Above B_C, r_{xx} is almost saturated. Then, we extrapolated r_{xx} in the ferromagnetic state to $B = 0$ and obtained the longitudinal resistance in the ferromagnetic state r_{xx}^0. The plots of ρ_{xy}^0 vs. r_{xx}^0 of $Co(S_{0.90}Se_{0.10})_2$ are depicted in Fig. 3-7. A nearly linear relation between ρ_{xy}^0 and r_{xx}^0 is observed, suggesting that the skew scattering is dominant in the AHE of $Co(S_{1-x}Se_x)_2$. These results strongly support the validity of our assumption that R_A is independent of the magnetic state.

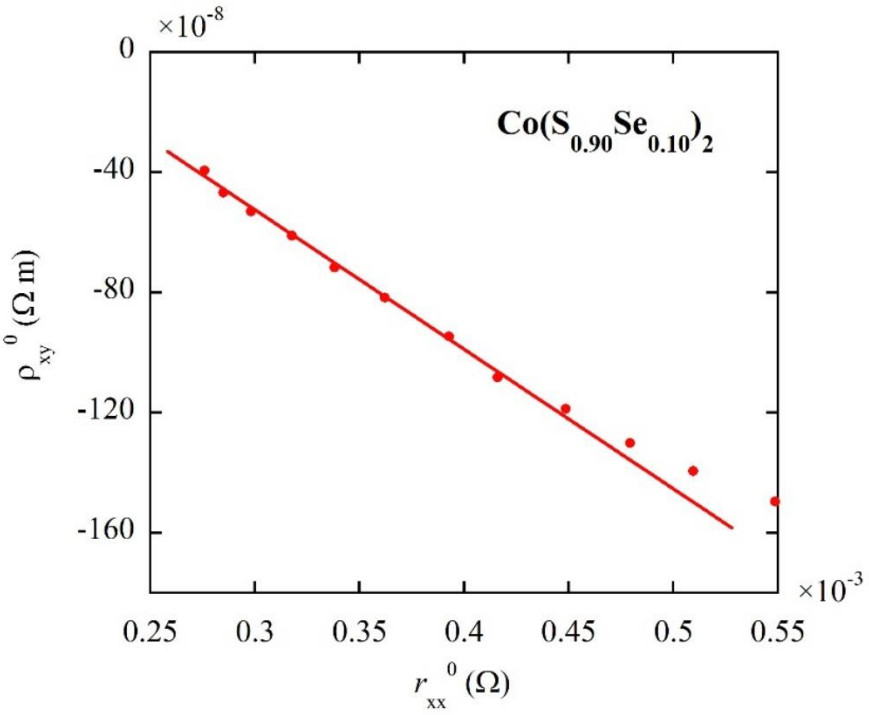

Fig. 3-7 Pots of ρ_{xy}^0 vs. r_{xx}^0 of $Co(S_{0.90}Se_{0.10})_2$.

Figure 3-8 shows R_A of $Co(S_{1-x}Se_x)_2$ as a function of temperature. For any x, R_A decreases with increasing temperature. This mainly originates in temperature dependence of ρ_{xy}^0, as shown in Figs. 3-4 (a) and 3-4 (b). The magnitude of R_A and its decreasing rate do not show systematic composition dependence. These results are consistent with our conclusion that the impurity scattering is responsible for the AHE.

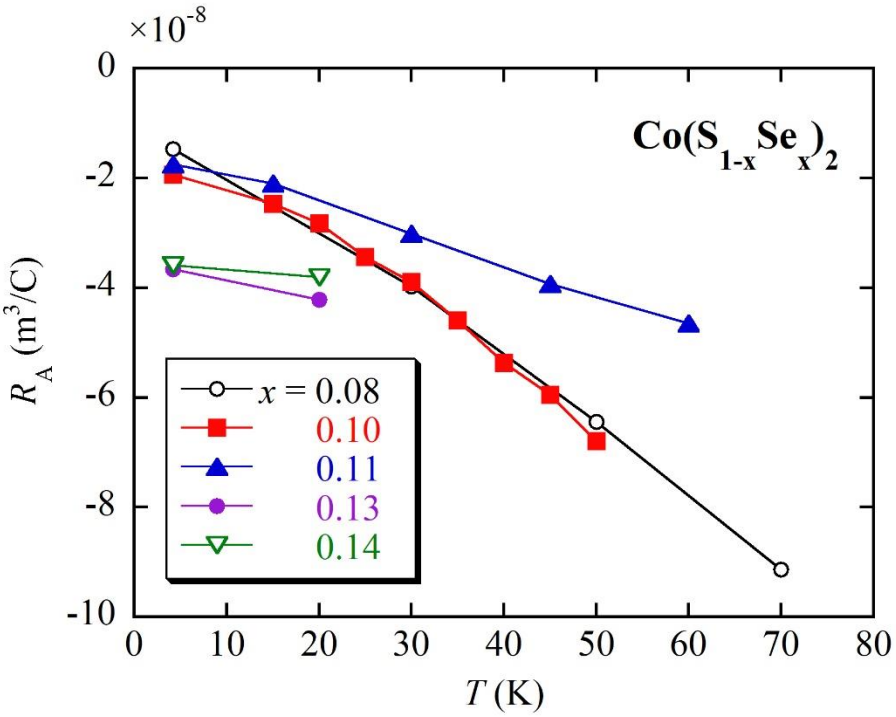

Fig. 3-8 Temperature dependence of R_A of $Co(S_{1-x}Se_x)_2$ with $0.08 \leq x \leq 0.14$. Solid lines are guide to the eye.

3.2 Energy band structure

The electronic structures of nonmagnetic and ferromagnetic CoS_2 and nonmagnetic $CoSe_2$ were calculated by using the lattice parameters and atomic positions previously reported [64, 65]. The first Brillouin zone of the Pyrite structure is depicted in Fig. 3-9. The X, Y, and Z points are equivalent due to the three-fold rotation symmetry, while the MX axis and MY axis are not equivalent in absence of the four-fold rotation symmetry in the *Pa*-3 space group. The partially filled energy band of nonmagnetic CoS_2 is displayed in Fig. 3-10. There exist four bands associated with the Fermi surface: the 41st, 42nd, 43rd, and 44th bands. The corresponding Fermi surfaces are illustrated in Fig. 3-11. The 41st and 42nd bands form the hole-like Fermi surfaces, which enclose unoccupied electron states. The 43rd and 44th bands form the electron-like surfaces, which enclose occupied electron states.

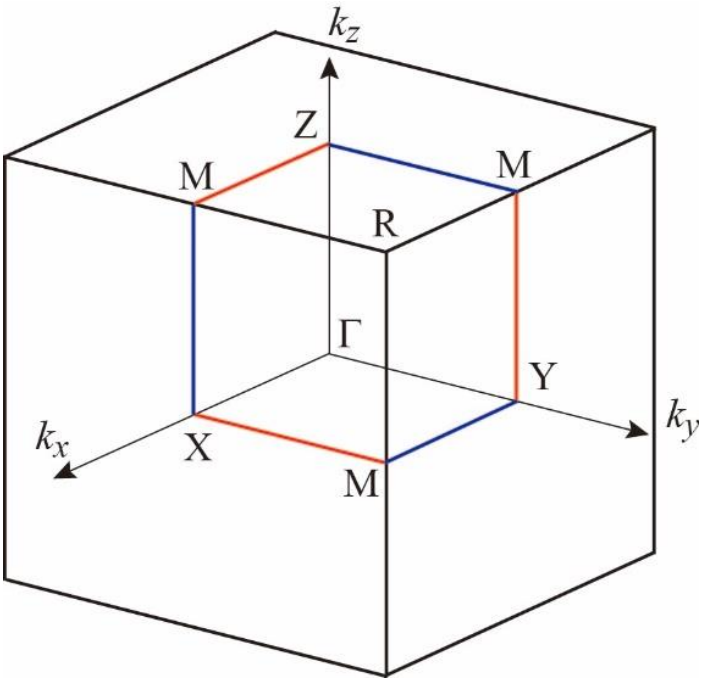

Fig. 3-9 The first Brillouin zone of CoS_2. Note that the X, Y, and Z points are equivalent points while the MX axis (red color) and the MY axis (blue color) are not equivalent.

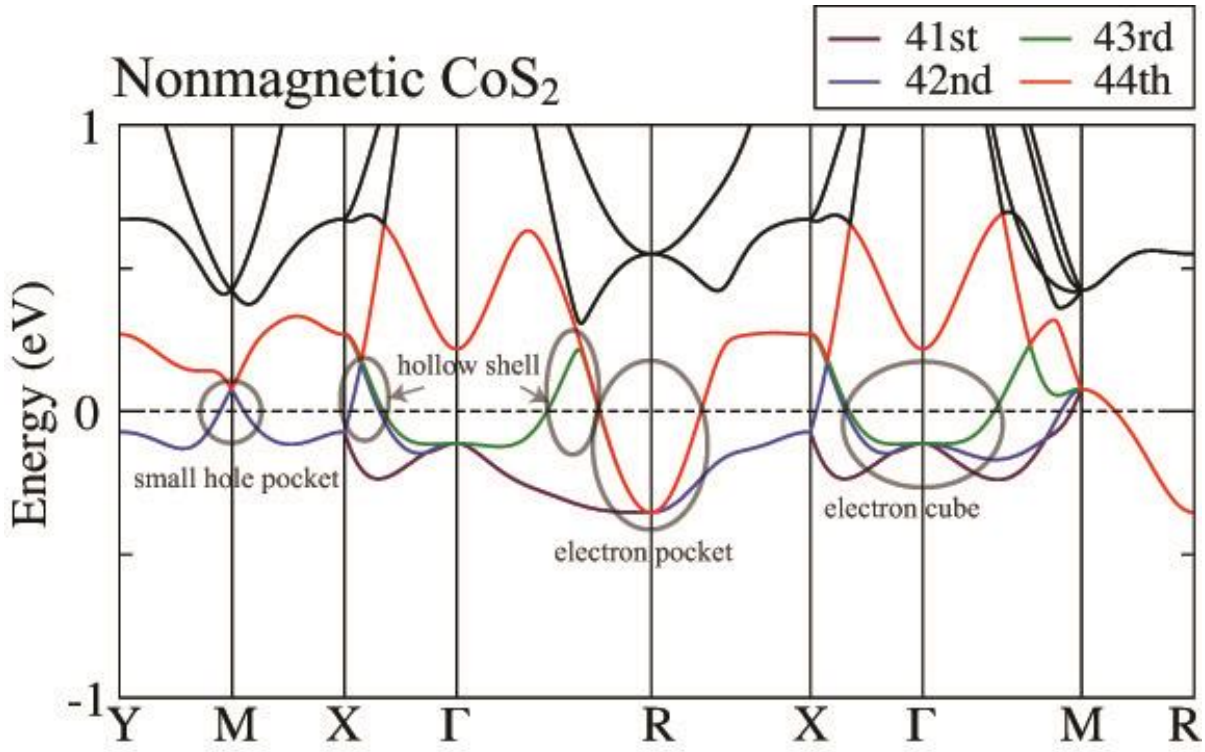

Fig. 3-10 Partially filled band of nonmagnetic CoS_2.

In the figure, each color represents the Fermi velocity: blue showing the lowest velocity and red showing the highest velocity. The 41st Fermi surface originates in a small hole pocket at around the M point. The 41st band and the 42nd band (also the 43rd band and 44th band) are doubly degenerate along the Y - M - X in Fig. 3-10. The 42nd Fermi surface is characterized by a hollow-shell structure in addition to a small hole pocket at around the M point. The Fermi velocity on the shell near the X point is significantly large due to the flat surface. The Fermi surface of the 43rd band consists of a nearly cubic electron surface centered at the Γ point and a nearly spherical electron surface centered at the R point. The Fermi velocity at the electron sphere is slightly larger than that at the electron cube. The 44th Fermi surface forms an electron pocket at the R point, which is very similar to that of the 43rd band.

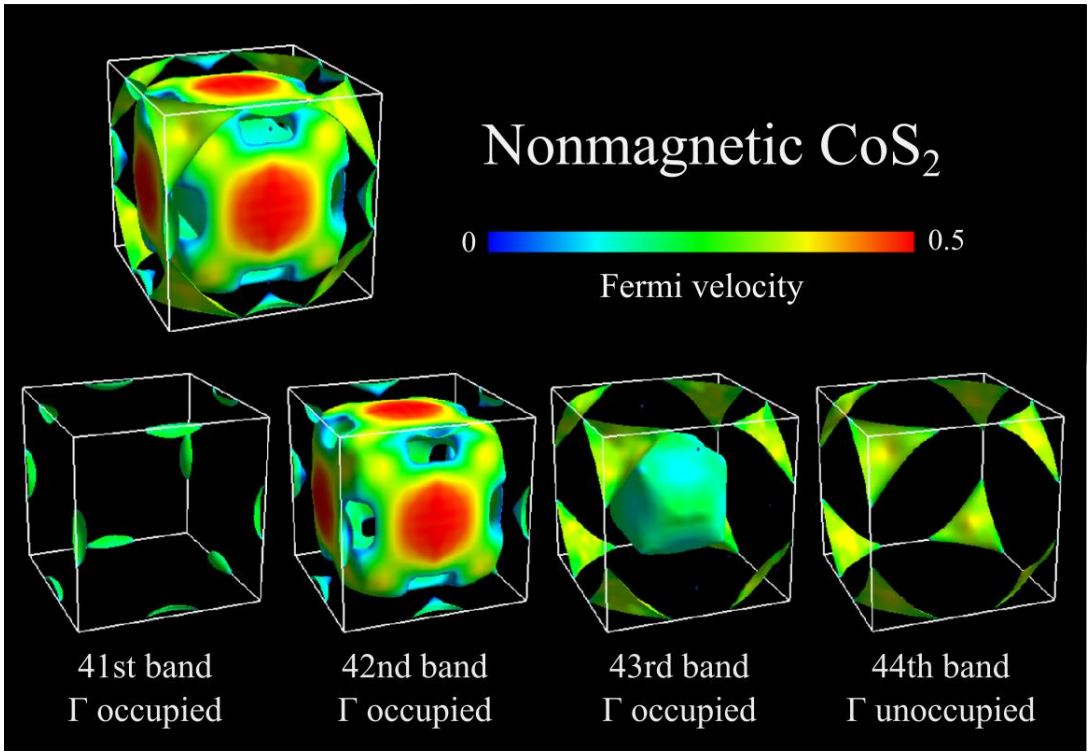

Fig. 3-11 Fermi surface and Fermi velocity of nonmagnetic CoS_2.

The energy band of ferromagnetic CoS_2 near the Fermi level is shown in Fig. 3-12. Our calculations show the half-metallic state of ferromagnetic CoS_2, in which only the up-spin bands form the Fermi surfaces. Thus, the up-spin bands are shown in the figure. The corresponding Fermi surfaces of ferromagnetic CoS_2 are illustrated in Fig. 3-13 The Fermi surfaces consist of the 44th hole-like surface and the 45th and 46th electron-like surfaces, being consistent with the previous work [60]. The 44th Fermi surface is a large hole cube centered at the Γ point. The Fermi velocity on the cube near the X point is considerably large. The 45th band is mostly degenerate with the 46th band except an electron bridge along the ΓM axis; the Fermi surface portions at around the R point are isolated in the 46th band, while they are connected in the 45th band.

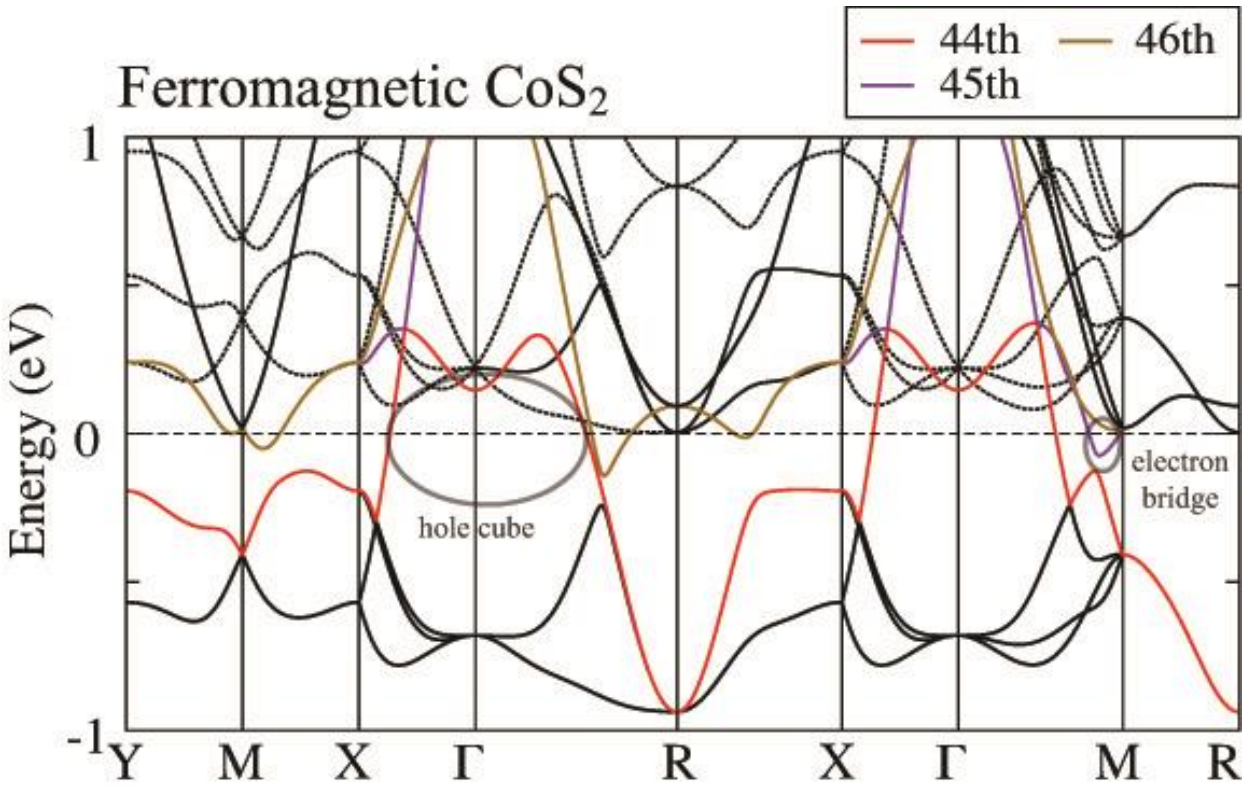

Fig. 3-12 Partially filled band of ferromagnetic CoS_2. Only up-spin bands are shown.

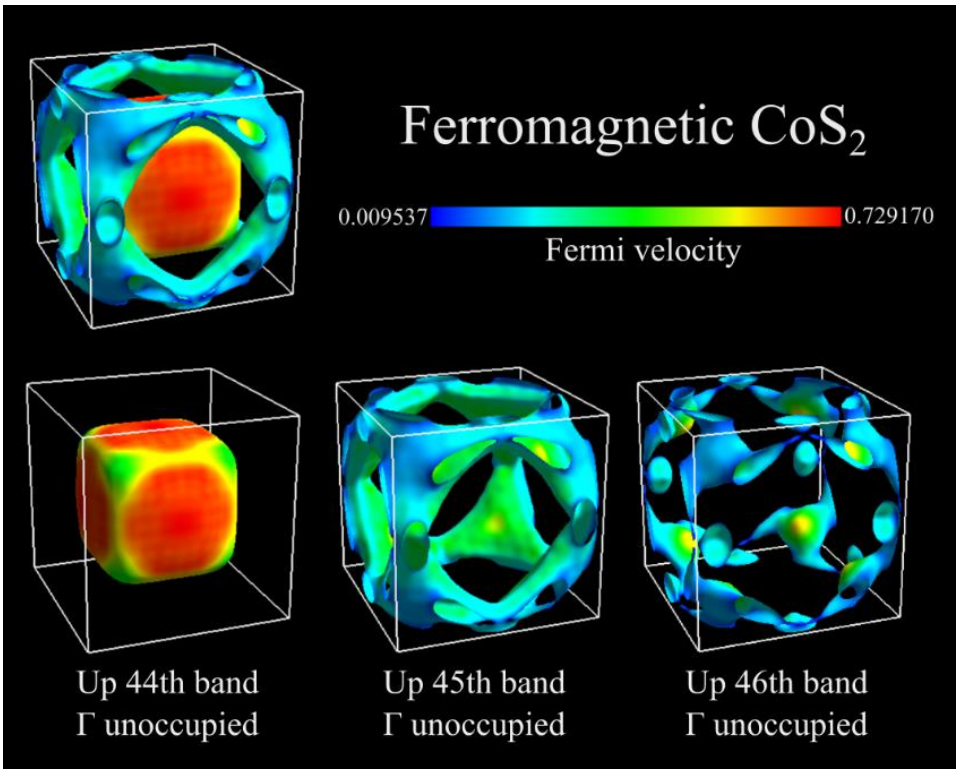

Fig. 3-13 Fermi surface and Fermi velocity of ferromagnetic CoS_2.

We also calculated the energy bands and the Fermi surfaces of nonmagnetic $CoSe_2$, which are shown in Figs. 3-14 and 3-15, respectively. The Fermi surfaces of nonmagnetic $CoSe_2$ consist of the 41st and 42nd hole-like surfaces and the 43rd and 44th electron-like surfaces, which are similar to the nonmagnetic CoS_2. The overall features of the Fermi surfaces are in agreement with the previous study [60]. In the 41st band, a hole pocket at around the M point and that at around the X point form the Fermi surfaces. In the 42nd Fermi surfaces, a hollow-shell structure emerges. The Fermi surface has a more spherical-like shape compared with that of nonmagnetic CoS_2. Large Fermi velocities are obtained on some points of the Fermi surface. The Fermi surfaces of the 43rd band and the 44th band consist of two electron spheres, one centered at the R point and the other at the Γ point. In both bands, the Fermi surfaces at the R point have relatively large Fermi velocities.

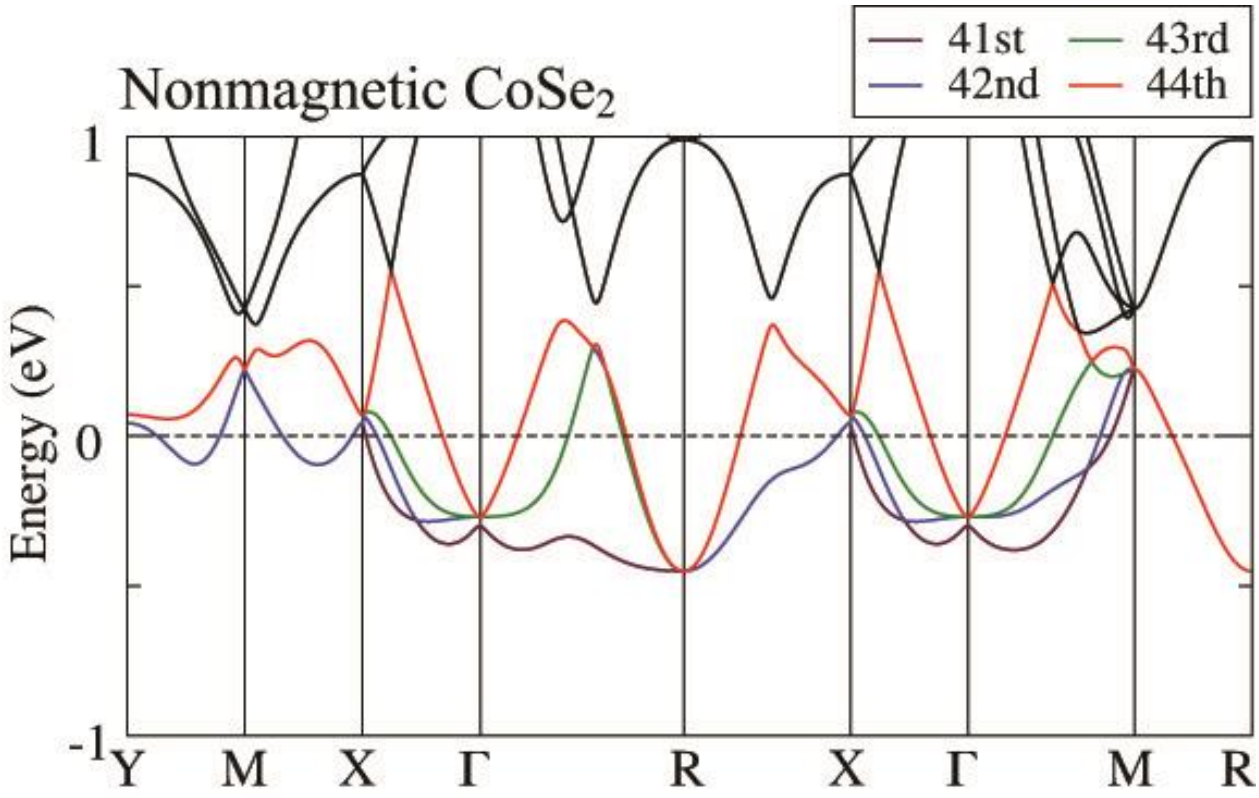

Fig. 3-14 Partially filled band of nonmagnetic $CoSe_2$.

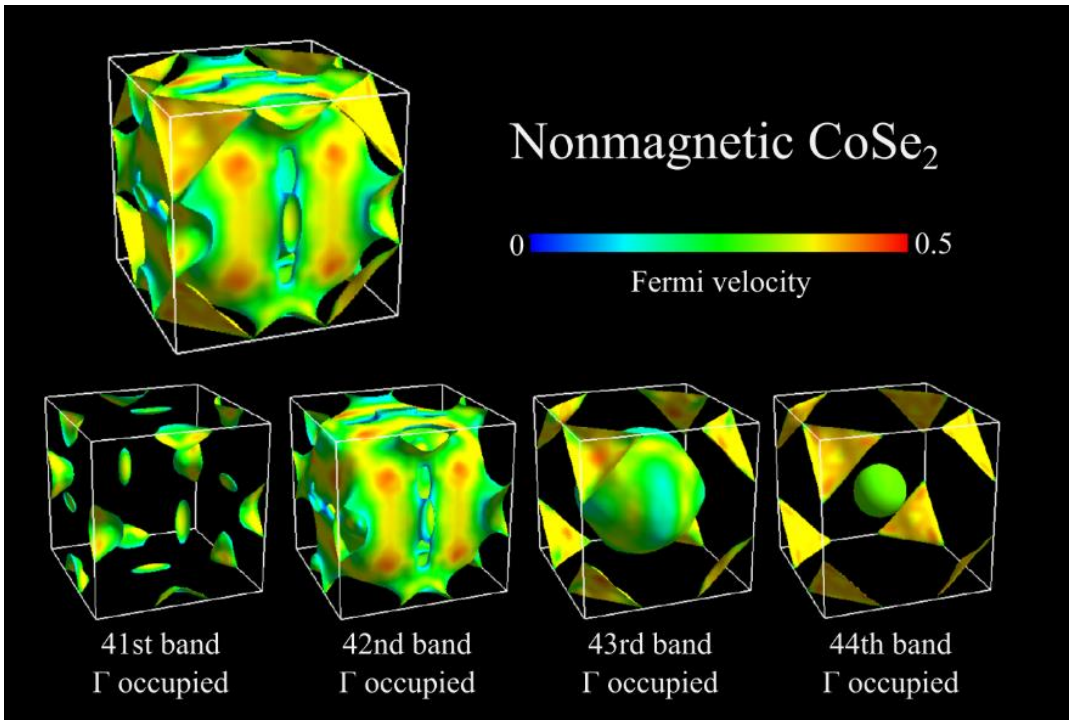

Fig. 3-15 Fermi surface and Fermi velocity of nonmagnetic $CoSe_2$.

We calculated the density of states at the Fermi energy $N(\varepsilon_F)$, the root mean square of the Fermi velocity v_F, and the normal Hall coefficient R_N for CoS_2 and $CoSe_2$, which are listed in Table 3-2. The $N(\varepsilon_F)$ of ferromagnetic CoS_2 is smaller than that of nonmagnetic CoS_2 and $CoSe_2$. This is due to half metallicity of the ferromagnetic state of CoS_2. The Fermi velocity of CoS_2 and $CoSe_2$ is in the range of 0.26-0.32 $\times$ 10^8 cm/s. No significant difference in v_F is found between the ferromagnetic and nonmagnetic states of CoS_2. The normal Hall coefficient of CoS_2 is strongly dependent on the magnetic state. In the ferromagnetic state, R_N is positive and large, whereas R_N of nonmagnetic CoS_2 is negative and small. In contrast, nonmagnetic $CoSe_2$ has a positive R_N.

Table 3-2 Calculated density of states (DOS) at Fermi energy $N(\varepsilon_F)$, the root mean square of the Fermi velocity v_F, and normal Hall coefficient R_N of CoS_2 and $CoSe_2$.

	Ferromagnetic CoS_2	Nonmagnetic CoS_2	Nonmagnetic $CoSe_2$
$N(\varepsilon_F)$ [/Ry cell]	69.378	145.360	145.650
v_F [10^8 cm/s]	0.281	0.265	0.315
R_N [10^{-11} m^3/C]	26.139	-0.463	16.46

3.3 Discussion

In this subsection, we compare the normal Hall coefficients of $Co(S_{1-x}Se_x)_2$ determined experimentally with those calculated from the energy band calculations for CoS_2 and $CoSe_2$. In the ferromagnetic state, $R_N{}^f$ is in the range of 30-40 × $10^{-11}m^3/C$. The calculated value for ferromagnetic CoS_2 is 26.139× $10^{-11}m^3/C$. Thus, the agreement between the experimental $R_N{}^f$ and the theoretical R_N is satisfactory. The large and positive R_N of ferromagnetic CoS_2 originates in the hole cube with large Fermi velocities.

In the paramagnetic state, the experimental results suggest that $R_N{}^p$ is 10-20 × $10^{-11}m^3/C$, which is a little smaller than $R_N{}^f$. The calculated R_N's of nonmagnetic CoS_2 is −0.463 × 10^{-11} m^3/C, which is negative and much smaller than $R_N{}^p$. The small R_N of nonmagnetic CoS_2 means that the positive contribution of the hole-like Fermi surface to R_N nearly cancels the negative contribution of the electron-like Fermi surface. The calculated R_N of nonmagnetic $CoSe_2$ is 16.46× 10^{-11} m^3/C. The experimental $R_N{}^p$ values are rather close to this R_N of nonmagnetic $CoSe_2$.

In the following, we discuss the origin of discrepancy between the experimental $R_N{}^p$ and the calculated R_N of nonmagnetic CoS_2 from both experimental and theoretical aspects. Compared with the ferromagnetic state, precise determination of $R_N{}^p$ is difficult, because the AHE makes a significant contribution to R_{obs} in the paramagnetic state. As shown in eq. (3-8), estimation of χ_p is crucial to determine $R_N{}^p$ precisely. However, the paramagnetic state is realized only at low field regions, below 4 T for x = 0.13 and below 6 T for 0.14 at 4.2 K. Because $Co(S_{1-x}Se_x)_2$ is a solid solution, the concentration fluctuations are inevitable. Therefore, some parts of the sample have a lower Se composition than the initial value. These parts undergo IEM below B_C, which enhances the magnetic susceptibility in the paramagnetic state. In this case, $R_N{}^p$ is overestimated. Narrow field ranges of the paramagnetic state make it difficult to estimate χ_p without ambiguity. Actually, if we adopt the magnetic susceptibility of x = 0.20 for χ_p from ref. 15, our analyses for x = 0.13 and 0.14 give $R_N{}^p$ =0.3-1.0 ×10^{-11} m^3/C at 4.2 K, which is very close to the calculated R_N of nonmagnetic CoS_2. The compound with x = 0.20 exhibits IEM at around 20 T, so that the effect of concentration fluctuations on χ_p is avoidable at low fields. To clarify this point, experiments under further high magnetic fields are desired for the compounds with x > 0.14.

In the theoretical aspect, we found some similarities in the Fermi surfaces between nonmagnetic CoS_2 and nonmagnetic $CoSe_2$, though there is a significant difference between their R_N values. These results suggest that the normal Hall coefficient is sensitive to the fine structures of the energy band for the individual materials. Although the experimental $R_N{}^p$ values are not well reproduced by the calculated results, our calculated results explain the experimental trend that R_N of the nonmagnetic state is smaller than that of the ferromagnetic state in CoS_2. To study the effect of a magnetic field on the normal Hall coefficient, we calculated R_N of nonmagnetic CoS_2 under a hypothetical magnetic field in a rigid-band approximation. By applying a magnetic field, we artificially shift up the Fermi energy for the up-spin state and shift down the Fermi energy for the down-spin state so that the total occupation number is fixed. The calculated R_N is shown in Figs. 3-16 (a) as a function of the Fermi energy shift. It is found that R_N strongly depends on the energy shift. The normal Hall coefficient is first negative mainly due to the electron carriers of 41-42th Fermi surfaces. It changes the sign to positive, when the Fermi energy crosses the upper part of 43-44th bands and the hole-carrier contribution becomes dominant.

Figure 3-16 (b) shows the relation between the normal Hall coefficient and the magnetization M induced by a hypothetical magnetic field. Here, the relation between the induced magnetization and the Fermi energy shift was obtained through the integrated DOS (not shown). In this figure, up-spin and down-spin components of R_N are also depicted. R_N is tiny at $M = 0$ (nonmagnetic state) and it shows the negative value, when the spin polarization is small. The sign of R_N turns to be positive, when the spin polarization becomes large. The rather complex behavior originates in the non-symmetric electron and hole contributions from the four Fermi surfaces. At $M > 3$ μ_B/unit cell, R_N becomes negative and very large in magnitude. We note that the down-spin component should be zero in the ferromagnetic state of CoS_2, because it is half metallic. Therefore, the rigid band model is no longer valid for such a large spin polarization. Our calculation results suggest that the magnetization induced by an external magnetic field leads to positive R_N in the nonmagnetic state. The experimental results may be explained by this scenario.

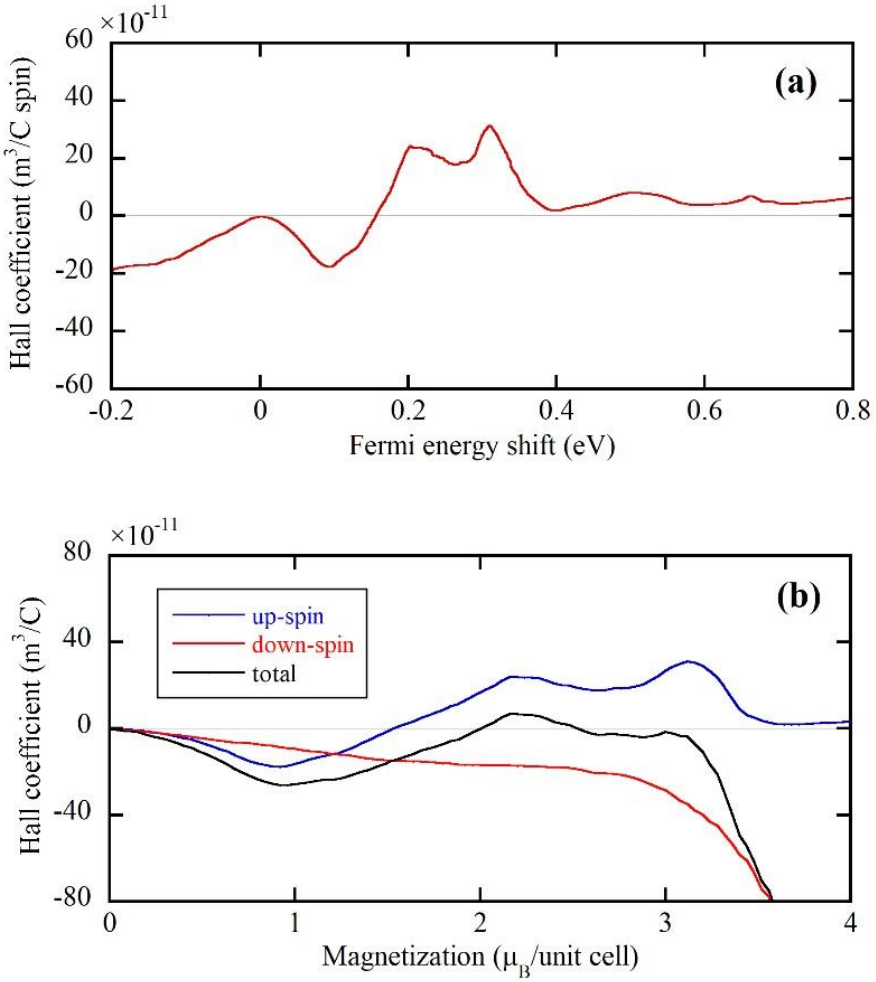

Fig. 3-16 (a) Calculated normal Hall coefficient for nonmagnetic CoS_2 as shifting the Fermi energy. (b) Calculated normal Hall coefficient for nonmagnetic CoS_2 as a function of induced magnetization.

In conclusion, we successfully estimated $R_N{}^f$ and $R_N{}^p$ of $Co(S_{1-x}Se_x)_2$ by assuming that R_A is independent of the magnetic state. This is the first report to determine the normal Hall coefficients in both the ferromagnetic and paramagnetic states at the same temperature. Appearance of both magnetic states depending on a magnetic field in IEM makes it possible to estimate these values, simultaneously. The validity of the above assumption was checked. The estimated normal Hall coefficients are compared with the theoretical values calculated from the energy band structures. Fairly good agreement between the experimental and theoretical values was obtained for the ferromagnetic state. The difference between these two values in the paramagnetic state was discussed from both experimental and theoretical aspects.

Chapter 4 Results and discussion on $Lu(Co_{1-x}Al_x)_2$ and RCo_2 (R=Lu and Er)

In this chapter, first we show the experimental results and analyses of $Lu(Co_{0.91}Al_{0.09})_2$. This compound shows IEM and our analyses shown in Chapter 3 are applicable to the results. Then, we show the results of $LuCo_2$. For the analyses, we adopted R_A of $Lu(Co_{0.91}Al_{0.09})_2$. Third, the results of $ErCo_2$ are presented. We used alternative analyses to obtain R_N and R_A of $ErCo_2$. The band calculations were performed for ferromagnetic and nonmagnetic $LuCo_2$.We compare the calculated results with the experimental results in the final section.

4.1 Experimental results and analyses of $Lu(Co_{0.91}Al_{0.09})_2$

For $Lu(Co_{0.91}Al_{0.09})_2$, the measurements were carried out at p = 0.5 GPa as well as at ambient pressure. Figure 4-1 shows the temperature dependence of magnetization of $Lu(Co_{0.91}Al_{0.09})_2$ at various magnetic fields and at ambient pressure. The $M - T$ curves were measured on heating. The compound is ferromagnetic at low temperatures. A sharp magnetic transition was detected at 1 T at around 50 K suggesting a FOMT. With increasing magnetic field, the transition becomes broader. The Curie temperature can be obtained from the peak in the $-dM/dT$ vs. T curve. By extrapolating the peak temperature to B = 0, we have T_C = 48 K for $Lu(Co_{0.91}Al_{0.09})_2$. The magnetization curves of $Lu(Co_{0.91}Al_{0.09})_2$ at various temperatures are illustrated in Fig. 4-2. Above T_C, the compound undergoes IEM. The transition field increases with increasing temperature. The hysteresis is quite small at ambient pressure.

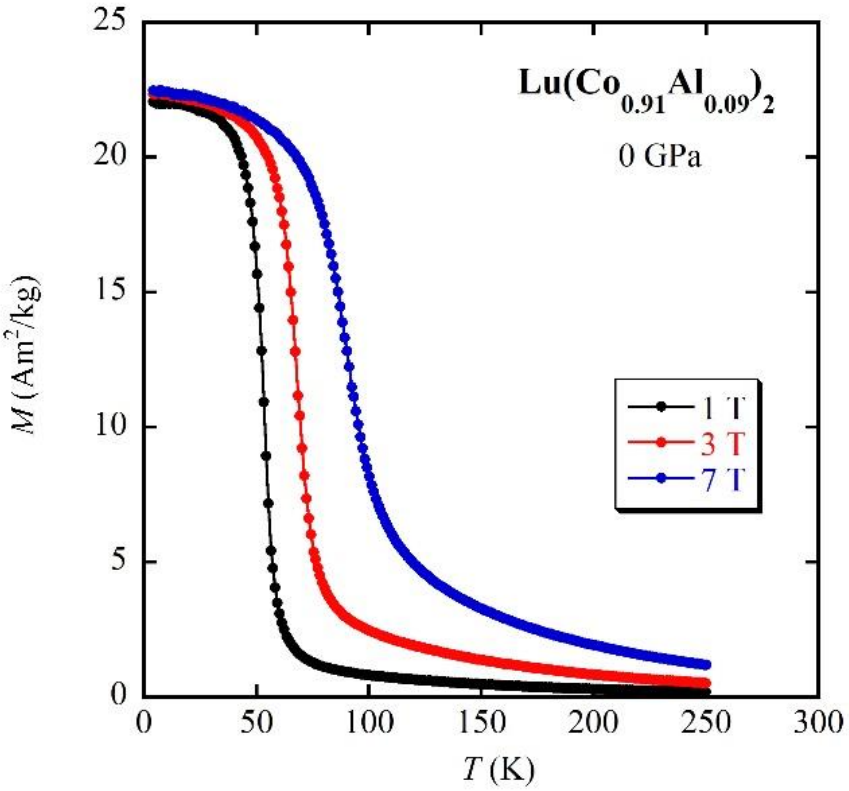

Fig. 4-1 Temperature dependence of magnetization of $Lu(Co_{0.91}Al_{0.09})_2$ at B = 1, 3 and 7 T and at ambient pressure. Data were obtained on heating.

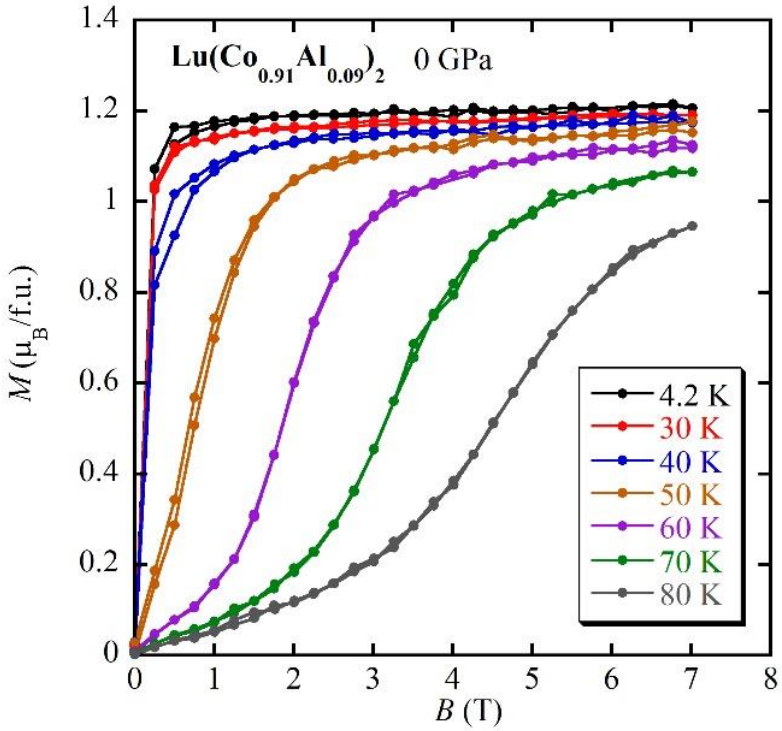

Fig. 4-2 Magnetization curves of $Lu(Co_{0.91}Al_{0.09})_2$ at various temperatures and at ambient pressure. Solid lines are guide to the eye.

The field dependence of the Hall resistivity of $Lu(Co_{0.91}Al_{0.09})_2$ at various temperatures and at ambient pressure is illustrated in Fig. 4-3. Below T_C, the $\rho_{xy} - B$ curves show rapid falls at low fields, which are attributable to the AHE. Therefore, the compound exhibits the negative AHE. Above the technical saturation, ρ_{xy} has a positive slope. Above T_C, ρ_{xy} initially decreases with increasing field in the paramagnetic state. When IEM takes place, ρ_{xy} rapidly drops due to the negative AHE. At high fields where the ferromagnetic state is induced, the $\rho_{xy} - B$ curves increases with increasing magnetic field.

Next, we show the results of $Lu(Co_{0.91}Al_{0.09})_2$ at a pressure of 0.5 GPa. The isothermal magnetization curves of $Lu(Co_{0.91}Al_{0.09})_2$ at are displayed in Fig. 4-4. No ferromagnetic behavior was observed and IEM is detected at 4.2 K. This means that applying a pressure of 0.5GPa stabilizes a paramagnetic state down to the lowest temperature. The itinerant electron metamagnetic transition is accompanied by a large hysteresis at 4.2 K. The hysteresis becomes smaller with increasing temperature. Above 40 K, hysteresis almost disappears.

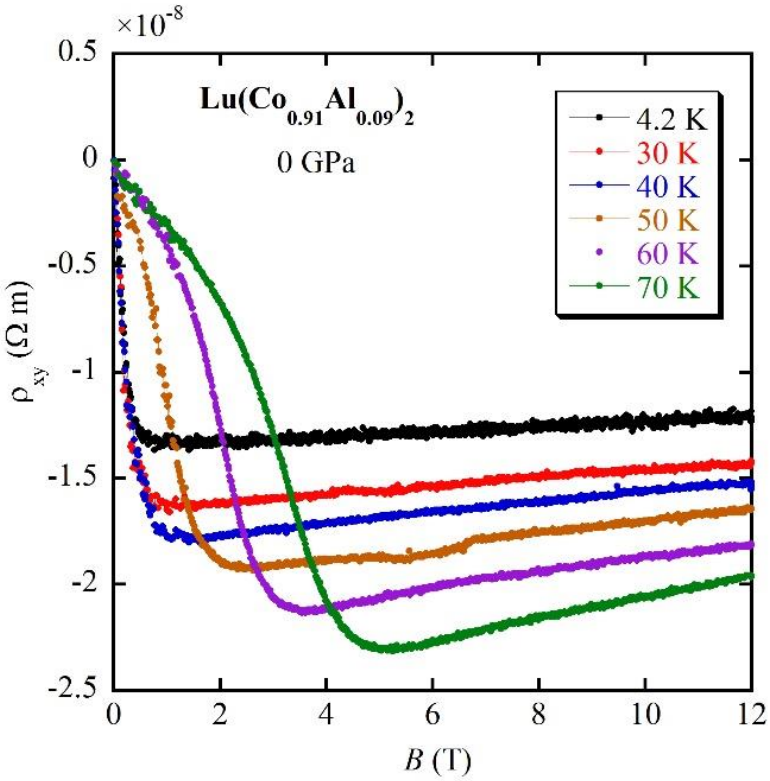

Fig. 4-3 Field dependence of the Hall resistivity ρ_{xy} of $Lu(Co_{0.91}Al_{0.09})_2$ at various temperatures and at ambient pressure.

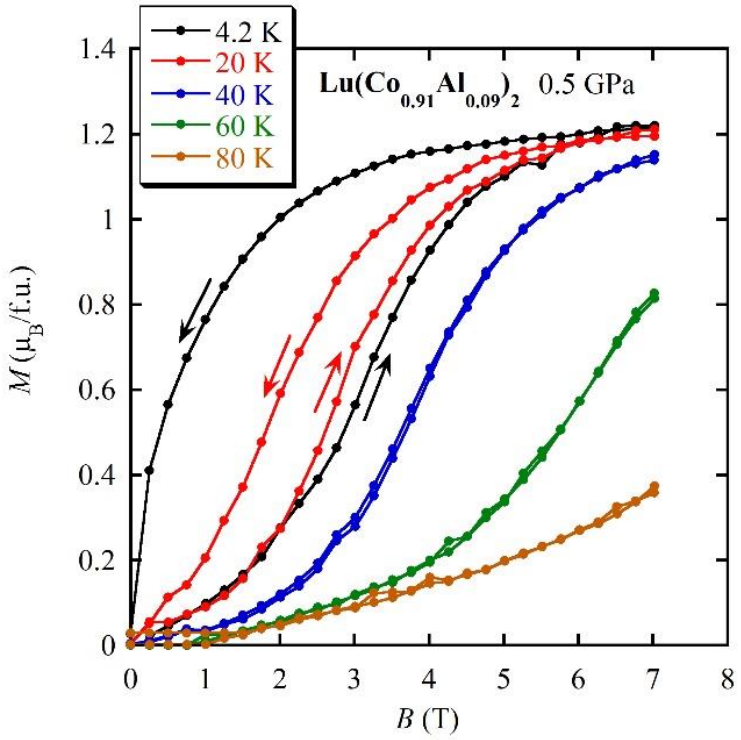

Fig. 4-4 Magnetization curves of $Lu(Co_{0.91}Al_{0.09})_2$ at various temperatures and at pressure of 0.5 GPa. Solid lines are guide to the eye.

The $\rho_{xy} - B$ curves of $Lu(Co_{0.91}Al_{0.09})_2$ at p = 0.5 GPa are displayed in Fig. 4-5. All the curves show characteristics of IEM described above. The $\rho_{xy} - B$ curve has a negative slope at low fields, followed by a rapid fall at around the transition field. Finally, ρ_{xy} increases with increasing field in the ferromagnetic state.

We analyzed the experimental data of $Lu(Co_{0.91}Al_{0.09})_2$ in the same manner as we did in Chapter 3. In the ferromagnetic state, both M and ρ_{xy} are approximated by linear functions of B given by eqs. (3.2) and (3.3). We determined the spontaneous magnetization M^0, the high-field magnetic susceptibility χ_{hf}, the intercept of the $\rho_{xy} - B$ curve ρ_{xy}^0, and its slope R_{obs}. The anomalous Hall coefficient R_A and the normal Hall coefficient in the ferromagnetic state R_N^f are obtained from eqs. (3.5) and (3.4), respectively.

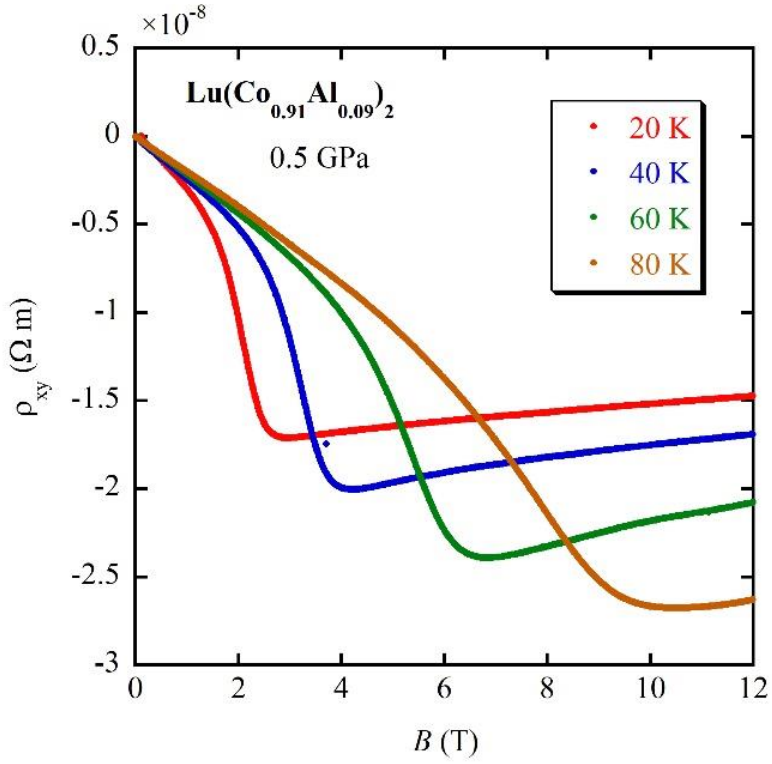

Fig. 4-5 The $\rho_{xy} - B$ curves of $Lu(Co_{0.91}Al_{0.09})_2$ at various temperatures and at pressure of 0.5 GPa.

The temperature dependence of R_A both at ambient pressure and at p = 0.5 GPa is illustrated in Fig. 4-6. At p = 0.5 GPa, the magnetization curves at 20 K and 40 K do not show saturation, so that we used M at 7 T as M^0. It is found that the magnitude of R_A increases with increasing temperature, which is a usual trend of ferromagnetic materials below T_C.

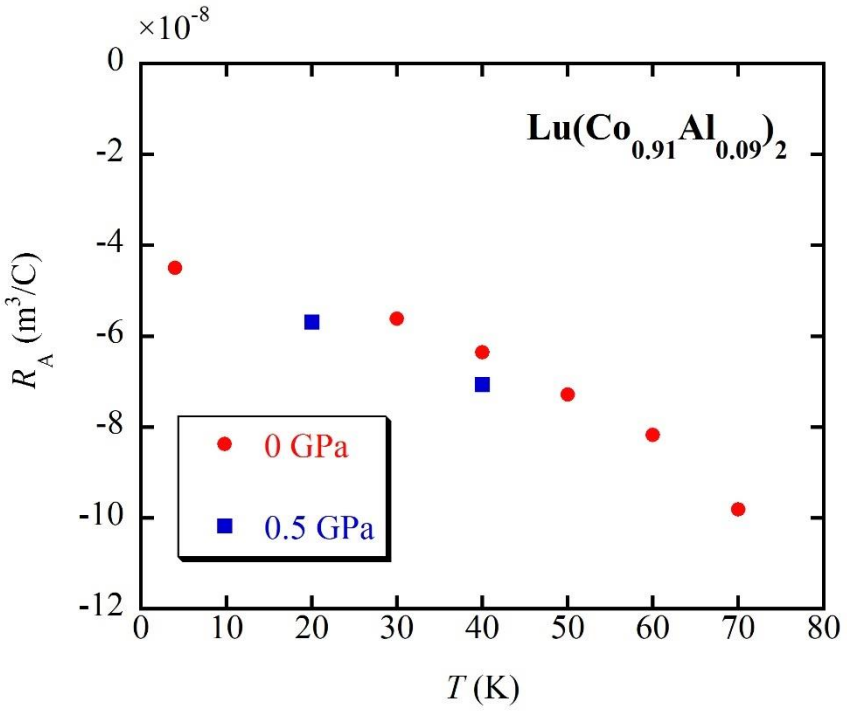

Fig. 4-6 Temperature dependence of R_A of $Lu(Co_{0.91}Al_{0.09})_2$ at ambient pressure and at 0.5 GPa.

The temperature dependence of $R_N{}^f$ at ambient pressure is shown by open circles in Fig. 4-7. For comparison, we plotted R_{obs}, at ambient pressure by closed circles in the same figure. It is found that both $R_N{}^f$ and R_{obs} are positive and they increase with increasing temperature. Moreover, $R_N{}^f$ is larger than R_{obs}. This is because R_A is negative. The difference between $R_N{}^f$ and R_{obs} is growing as the temperature is elevated. We were unable to estimate χ_{hf} and hence $R_N{}^f$ at p = 0.5 GPa, because IEM is not completed at the highest magnetic field of 7 T. Then, we plotted R_{obs} at p = 0.5 GPa by closed squares in Fig. 4-7. The R_{obs} values at p = 0.5 GPa are slightly larger than those at ambient pressure. Since the R_A values at p = 0.5 GPa are not so different from those at ambient pressure, we can deduce that $R_N{}^f$ at p = 0.5 GPa is slightly larger than that at ambient pressure. These results strongly suggest $R_N{}^f$ of $Lu(Co_{0.91}Al_{0.09})_2$ is in the range of 10-50 × 10^{-11} m^3/C below 70 K.

Before analyzing the Hall resistivity in the paramagnetic state, we checked the relation between $\rho_{xy}{}^0$ and $r_{xx}{}^0$ of $Lu(Co_{0.91}Al_{0.09})_2$ at ambient pressure, which is shown in Fig. 4-8. A nearly linear relation between them is obtained, suggesting that the skew scattering is dominant in the AHE of $Lu(Co_{0.91}Al_{0.09})_2$. Then, we assume that R_A is independent of the magnetic state of $Lu(Co_{0.91}Al_{0.09})_2$, as we have done for $Co(S_{1-x}Se_x)_2$.

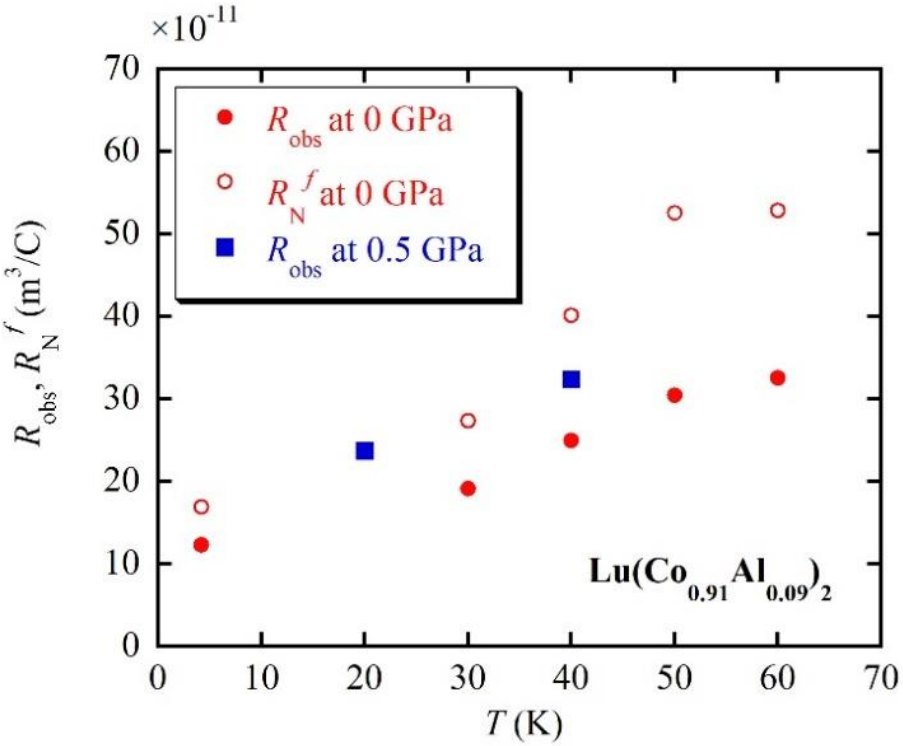

Fig. 4-7 Temperature dependence of R_{obs} and $R_N{}^f$ of ferromagnetic $Lu(Co_{0.91}Al_{0.09})_2$ at ambient pressure and at 0.5 GPa.

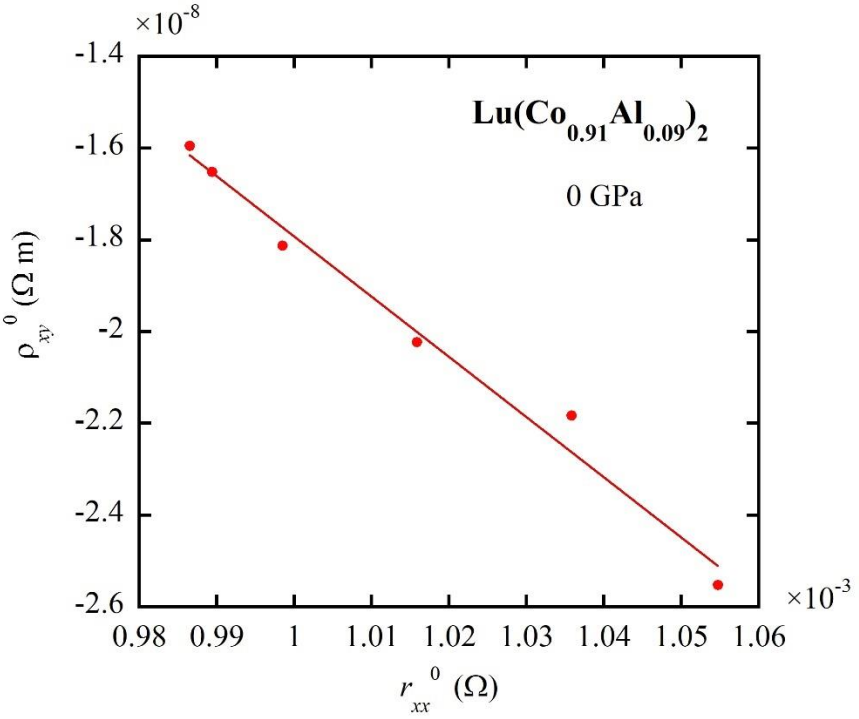

Fig. 4-8 Plots of $\rho_{xy}{}^0$ vs. $r_{xx}{}^0$ of $Lu(Co_{0.91}Al_{0.09})_2$. The solid line represents the linear least square fit.

Eqs. (3.6) - (3.8) are applied to estimation of R_N^p of $Lu(Co_{0.91}Al_{0.09})_2$. Unfortunately, the paramagnetic state is realized in a narrow field range, which makes it difficult to obtain both R_{obs} and χ_p of $Lu(Co_{0.91}Al_{0.09})_2$ with satisfactory accuracy. We only obtained them at (p = 0 GPa, T = 70 K) and at (0.5 GPa, 40 K), which are listed in Table 4-1. The estimated R_N^p values are negative, which are opposite in sign to R_N^f. The absolute values of R_N^p are larger than those of R_N^f. We have measured the $\rho_{xy} - B$ curves of $Lu(Co_{0.91}Al_{0.09})_2$ at 150 K and 200 K, which are displayed in Fig. 4-9. The measurements were carried out at ambient pressure. The Hall resistivity is linearly decreased with increasing field. The R_{obs} values are -120×10^{-11}m^3/C at 150 K and -70×10^{-11}m^3/C at 200 K. Since AHE becomes very small at high temperatures, the negative R_{obs} is mostly attributed to R_N^p. These results support that R_N^p is negative for $Lu(Co_{0.91}Al_{0.09})_2$.

Table 4-1 Observed R_{obs}, the anomalous Hall term $R_A\chi_p$, and estimated $R_N{}^p$ of paramagnetic $Lu(Co_{0.91}Al_{0.09})_2$.

p (GPa)	T (K)	R_{obs} (10^{-11} m^3/C)	$R_A\chi_p$ (10^{-11} m^3/C)	$R_N{}^p$ (10^{-11} m^3/C)
0	70	−274	−175	−99
0.5	40	−240	−66	−174

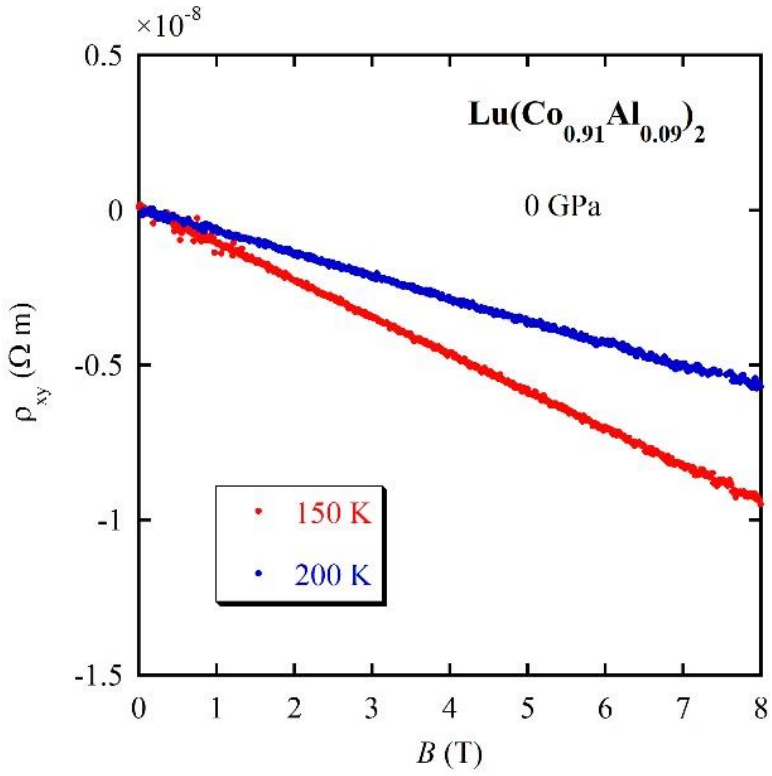

Fig. 4-9 The $\rho_{xy} - B$ curves of $Lu(Co_{0.91}Al_{0.09})_2$ at 150K and 200 K. The measurements were carried out at ambient pressure.

4.2 Experimental results and analyses of $LuCo_2$

Figure 4-10 shows the $\rho_{xy} - B$ curves of $LuCo_2$ at various temperatures. In the whole temperature range studied, ρ_{xy} increases linearly with increasing B. This is because both the NHE and AHE are proportional to B in the paramagnetic state, as described in section 1.7. The results indicate that R_{obs} of $LuCo_2$ is strongly dependent on temperature. Fig. 4-11 shows the temperature dependence of R_{obs} of $LuCo_2$. The R_{obs} is 102×10^{-11} m^3/C at 4.2 K and it decreases nearly linearly with increasing temperature down to 14×10^{-11} m^3/C at 70 K. The R_{obs} at 150 K is nearly the same as that at 70 K. As given in eq. (3.8), we need R_A to separate $R_N{}^p$ from R_{obs}. Since R_A of $LuCo_2$ is not known, we substitute R_A of $Lu(Co_{0.91}Al_{0.09})_2$ (Fig. 4-6) for it. The magnetic susceptibility of $LuCo_2$ gradually increases from 7×10^{-6} emu/g to 8×10^{-6} emu/g with increasing temperature from 4.2 K to 70 K [19]. Using these values, we estimated $R_A\chi_p$ and $R_N{}^p$ at 4.2 K, 40 K and 70 K, which are listed in Table 4-2. It is found that $R_A\chi_p$ is not sensitive to temperature. The $R_N{}^p$ is decreased with increasing temperature from 106×10^{-11} m^3/C (4.2 K) to 24×10^{-11} m^3/C(70 K). The magnitude of $R_A\chi_p$ is only 4 % of R_{obs} at 4.2 K, while it is comparable to R_{obs} at 70 K. The above R_A is of the same order of magnitude as those of $Co(S_{1-x}Se_x)_2$ described in Chapter 3. These results suggest that strong temperature dependence of R_{obs} is attributable to $R_N{}^p$. It is interesting to note that $R_N{}^p$ is positive in $LuCo_2$, while it is negative in $Lu(Co_{0.91}Al_{0.09})_2$. The origin of the sign change in $R_N{}^p$ in $Lu(Co_{1-x}Al_x)_2$ will be discussed later.

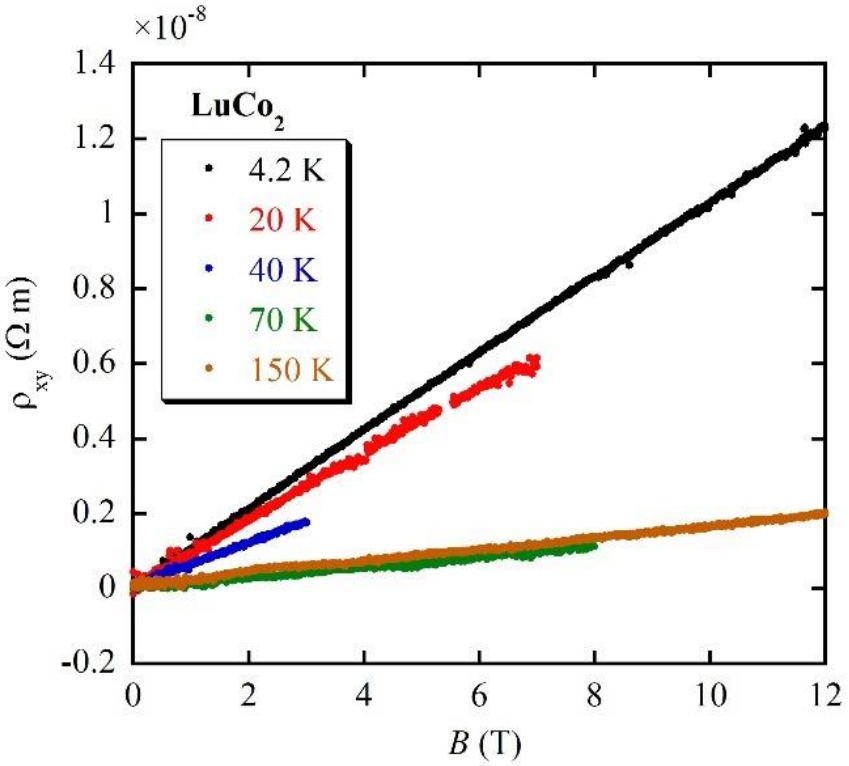

Fig. 4-10 Field dependence of the Hall resistivity ρ_{xy} of $LuCo_2$ at various temperatures.

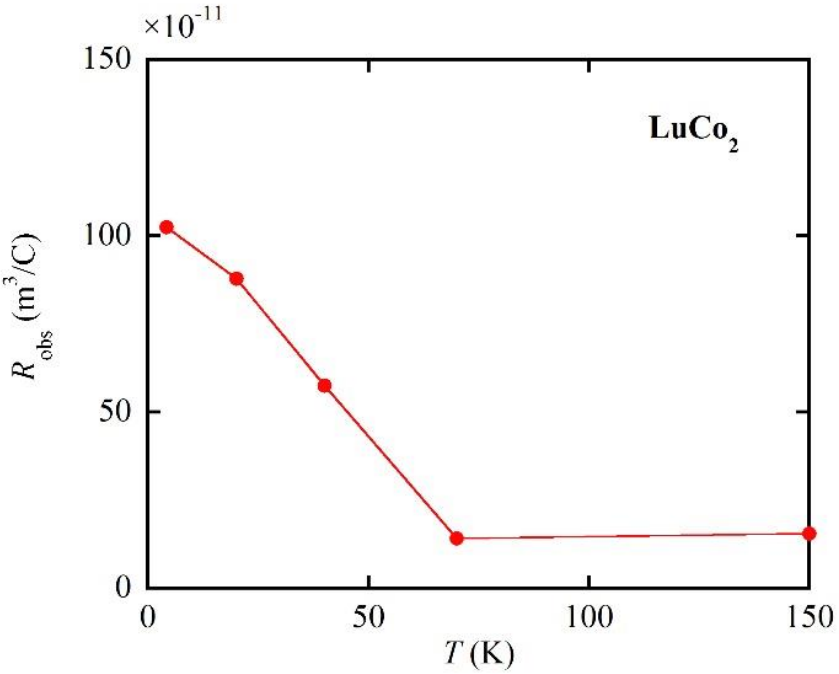

Fig. 4-11 Temperature dependence of R_{obs} of $LuCo_2$. A solid line is guide to the eye.

Table 4-2 Observed R_{obs}, the anomalous Hall term $R_A\chi_p$, and estimated $R_N{}^p$ for $LuCo_2$.

T (K)	R_{obs} (10^{-11} m^3/C)	$R_A\chi_p$ (10^{-11} m^3/C)	$R_N{}^p$ (10^{-11} m^3/C)
4.2	102	−4	106
40	57	−6	63
70	14	−10	24

4.3 Experimental results and analyses of $ErCo_2$

Figure 4-12 shows the isothermal magnetization curves of $ErCo_2$ at various temperatures. The resistivity measurements (not shown) revealed that T_C = 34 K for our sample. The $M - B$ curves in Fig. 4-12 resemble to Fig. 1-11, in which the magnetic field is applied parallel to the [111] direction. Below T_C, the compound is ferrimagnetic. Above T_C, IEM is observed. The magnetization increases rapidly below the transition field B_C. Above B_C, the ferrimagnetic state is induced and the $M - B$ curves have small slopes. As the temperature is elevated, B_C is higher and the transition is broader. No metamagnetic transition is observed up to 7 T above 47.5 K.

Figures 4-13 (a) and 4-13 (b) show the field dependences of ρ_{xy} of $ErCo_2$ below T_C (10 K ≤ T ≤ 30 K) and above T_C (35 K ≤ T ≤ 100 K), respectively. Below T_C, the $\rho_{xy} - B$ curves show ferromagnetic (or ferrimagnetic) behavior. The Hall resistivity shows a rapid rise at low fields, followed by another linear line with a smaller slope. A rapid rise at low fields originates in the AHE and a linear variation of ρ_{xy} at high fields is due to the

NHE. The results indicate that both the AHE and NHE are positive in the ferrimagnetic state of $ErCo_2$. The $\rho_{xy} - B$ curves above T_C are dramatically different from those below T_C. They are characterized by large and negative ρ_{xy}. The Hall resistivity first decreases with increasing B, showing a minimum at an appropriate field, and then abruptly increases, when IEM takes place. In the ferrimagnetic state above B_C, ρ_{xy} increases linearly with increasing field.

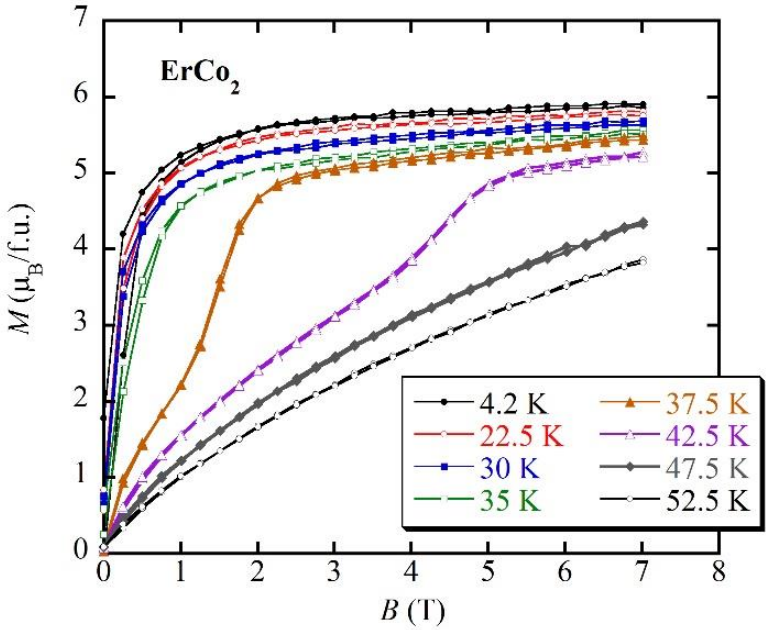

Fig. 4-12 Isothermal magnetization curves of $ErCo_2$.

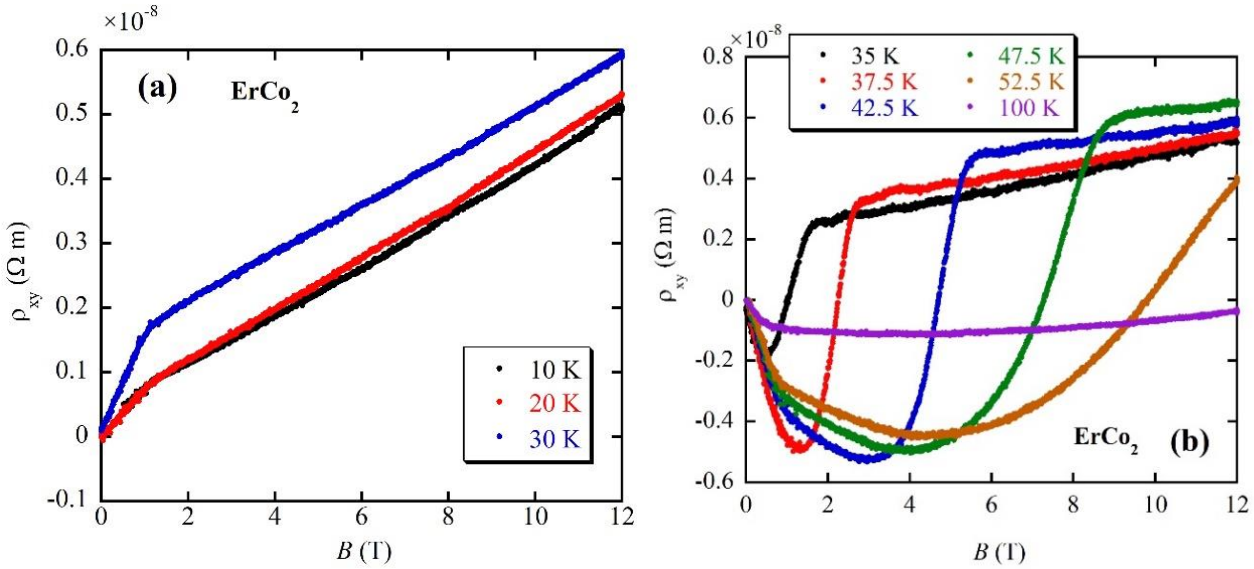

Fig. 4-13 Field dependence of ρ_{xy} of $ErCo_2$ at 10 K ≤ T ≤ 30 K (a) and at 35 K ≤ T ≤ 100 K (b).

To estimate R_N (R_N^f and R_N^p) and R_A we adopt alternative analysis. Dividing eq. (3.1) by B, we have,

$$\frac{\rho_{xy}}{B} = R_N + R_A \frac{M}{B}. \qquad (4.1)$$

This equation means that the ρ_{xy} /B vs. M/B plots collapse onto a straight line, when eq. (3.1) holds. The coefficients R_N and R_A are obtained from the intercept and the slope, respectively. For the plots, we have to prepare ($\rho_{xy}(B)$, $M(B)$) data. For ρ_{xy} (B), we used the measured data below 7 T. The $M(B)$ data were obtained from interpolation after smoothing the measured $M - B$ curve. Fig. 4-14 (a) displays the ρ_{xy}/B vs. M/B plots of $ErCo_2$ below 30 K. In these plots, data with $B < 1.4$ T were eliminated. Note that higher magnetic fields give smaller M/B values. Since we have not measured the $M - B$ curve at 10 K, the magnetization data at 4.2 K were adopted. The results indicate linear relations between ρ_{xy}/B and M/B for $ErCo_2$ below T_C. The normal Hall coefficient is estimated by extrapolating the line to $M/B = 0$. R_N is about 35×10^{-11}m^3/C below 30 K. The anomalous Hall coefficient is obtained from the slope of the line. The R_A at 30 K is about three times as large as that at 20 K. The ρ_{xy} /B vs. M/B plots of $ErCo_2$ at 35 K $\leq T \leq$ 52.5 K are depicted in Fig. 4-14 (b). In contrast to the plots below T_C, the ρ_{xy} /B shows complicated M/B dependence. For 35 K $\leq T \leq$ 42.5 K, ρ_{xy} /B varies linearly at high fields (at low M/B portions), because the ferrimagnetic state is stable above B_C. We estimated R_N^f and R_A in the induced ferrimagnetic state. Temperature dependence of R_N^f and R_A of $ErCo_2$ in the ferrimagnetic state below and above T_C is illustrated in Fig. 4-15. The R_N^f above T_C is about 15×10^{-11}m^3/C, being somewhat smaller than that below T_C. The R_A increases continuously from 0.04 to 0.28×10^{-8} m^3/C with increasing temperature from 10 to 40 K.

Next, we focus on the ρ_{xy} /B vs. M/B plots in the paramagnetic state. As shown in Fig. 4-14 (b), ρ_{xy} /B deviates from a straight line near B_C. At 35 K, deviation of ρ_{xy} /B starts at around $M/B = 3.2$ μ_B/f.u. T ($B = 1.5$ T), though it is not shown in the figure. We found that the ρ_{xy} /B data lie on a different straight line below the transition field just above T_C. This linear relation is observed in the field range of $0.63 \leq B \leq 2.3$ T at 40 K and $0.67 \leq B \leq$ 3.4 T at 42.5 K. The transition fields determined from a peak position of dM/dB are 2.8 T and 4.4 T at 40 K and 42.5 K, respectively. Dash-dotted lines in Fig. 4-14 (b) represent least squares fits of straight lines to the sets of data points near B_C. It looks that the linear portion shifts toward higher fields, as the temperature is raised. Assuming that this linear relation means eq. (4.1), we estimated R_N and R_A of $ErCo_2$ in the paramagnetic state. Temperature dependence of R_N^p and R_A of $ErCo_2$ in the paramagnetic state is displayed in Fig. 4-16. The results suggest that R_N^p is positive, while R_A is negative in the paramagnetic state. These results are also supported by ρ_{xy} at 100 K (shown in Fig. 4-13 (b)), which initially decreases with increasing field and increases at high fields. Since the AHE is dominant at low fields, it is plausible that the paramagnetic state of $ErCo_2$ has positive R_N^p and negative R_A. Therefore, large negative ρ_{xy} in the paramagnetic state of $ErCo_2$ is attributable to the negative AHE. The R_N^p value is about 200×10^{-11}m^3/C just above T_C, which are one order of magnitude larger than those in the ferrimagnetic state and of the same order of magnitude as that of $LuCo_2$ at 4.2 K. The absolute values of R_A in the paramagnetic state are also much larger than those in the ferrimagnetic state. Both R_N^p and R_A show weak temperature dependence. Our results indicate that the AHE changes the sign from positive to negative, when $ErCo_2$ undergoes a FOMT from the ferrimagnetic to paramagnetic state. The origin of sign change in R_A of $ErCo_2$ will be discussed later.

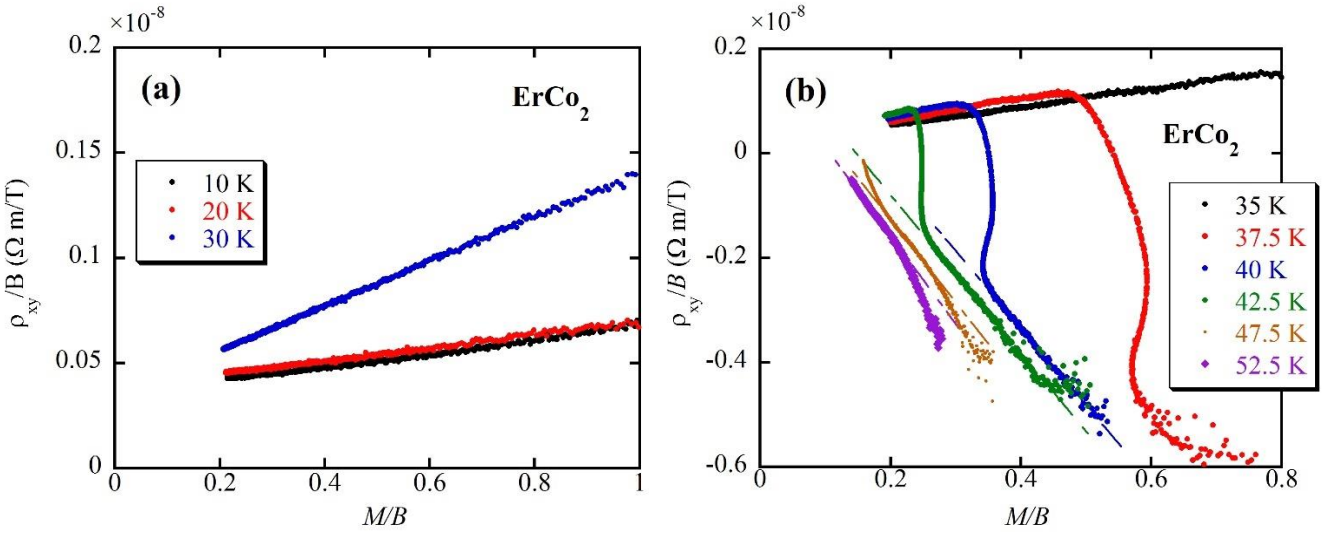

Fig. 4-14 (a) ρ_{xy} /B vs. M/B plots of $ErCo_2$ at 10 K ≤ T ≤ 30 K (below T_C). (b) The plots at 35 K ≤ T ≤ 52.5 K (above T_C). Dash-dot lines represent least squares fits of straight lines to the data near B_C.

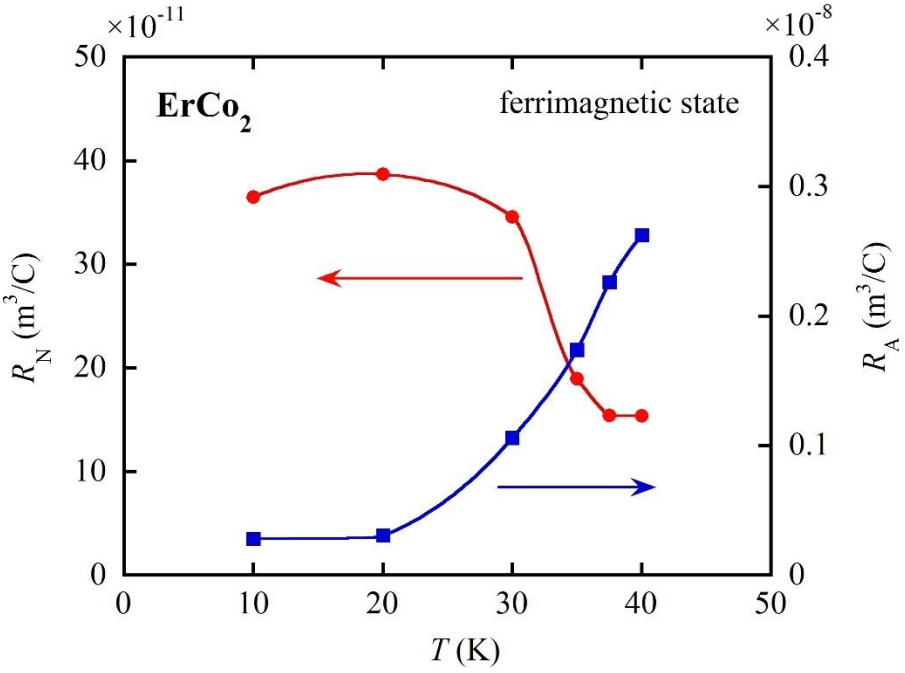

Fig. 4-15 Temperature dependence of R_N^f (circles)and R_A (squares) of $ErCo_2$ in the ferrimagnetic state. Solid lines are guide to the eye.

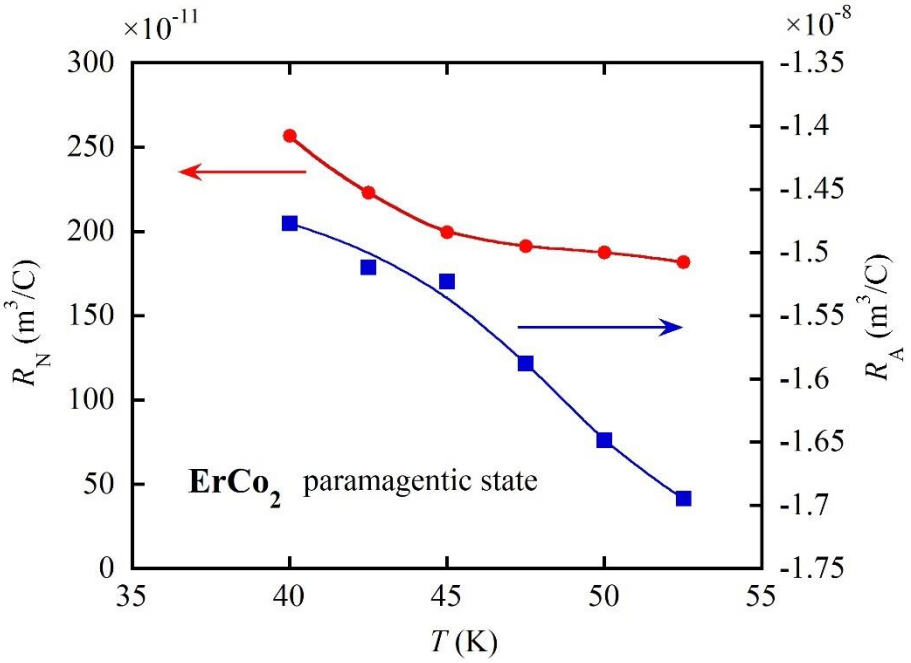

Fig. 4-16 Temperature dependence of $R_N{}^p$ (circles)and R_A (squares) of $ErCo_2$ in the paramagnetic state. Solid lines are guide to the eye.

4.4 Energy band structure of $LuCo_2$

To evaluate R_N of RCo_2 theoretically, we carried out density-functional theory calculations for nonmagnetic and ferromagnetic $LuCo_2$. The lattice parameter was fixed at their experimental value, a = 7.108 Å [66]. The muffin-tin radii are set as 1.2 Å and 1.0 Å for Lu and Co, respectively. The first Brillouin zone of the C15 Laves phase structure is depicted in Fig. 4-17. Figures 4-18 (a) and 4-18 (b) show the energy band structures of nonmagnetic and ferromagnetic $LuCo_2$, respectively. The total density of states (DOS) and Co-*d* partial DOS are shown in Figs. 4-19 (a) and 4-19 (b) for nonmagnetic and ferromagnetic states, respectively. The Co-*d* bands make a dominant contribution to the total DOS in the energy range from −2 to +0.5 eV. Two sharp peaks originating from van Hove singularities are visible near the Fermi energy ε_F, which are responsible for magnetic instability in the C15 Laves phase compounds containing 3*d* transition metals [67-69]. In the nonmagnetic state, the Fermi level is located near the bottom of the valley between two peaks. This is preferable for onset of IEM, because the DOS at the Fermi energy $N(\varepsilon_F)$ is increased by the application of magnetic field, as described in section 1.1 (see Fig. 1-2). In the ferromagnetic state, ε_F lies below two sharp peaks in the DOS of down-spin bands, while the up-spin *d* bands are nearly full-filled. The calculated Co moment is 1.07 μ_B, which is larger than that determined from the high-field magnetization curve of $LuCo_2$, 0.7 μ_B [27]. This calculated value is, however, in agreement with the observed Co moment in $DyCo_2$, $HoCo_2$ and $ErCo_2$, 1.0 μ_B [29, 30, 70]. These facts suggest that 1.0 μ_B is the saturation value of Co moment in RCo_2 compounds. This is understandable from the DOS in Fig. 4-19 (b). The up-spin *d* bands are almost full-filled in the ferromagnetic $LuCo_2$, so that further band splitting is no longer induced by a molecular field.

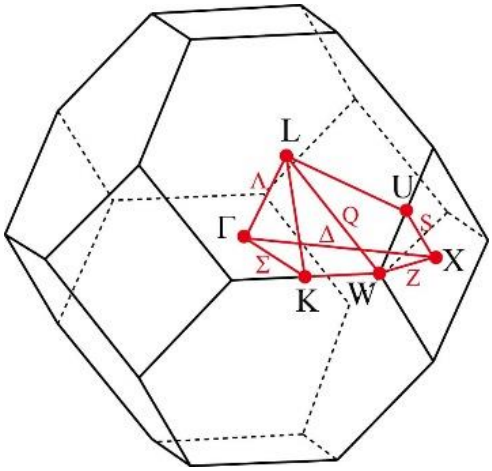

Fig. 4-17 The first Brillouin zone of $LuCo_2$ with high symmetry points.

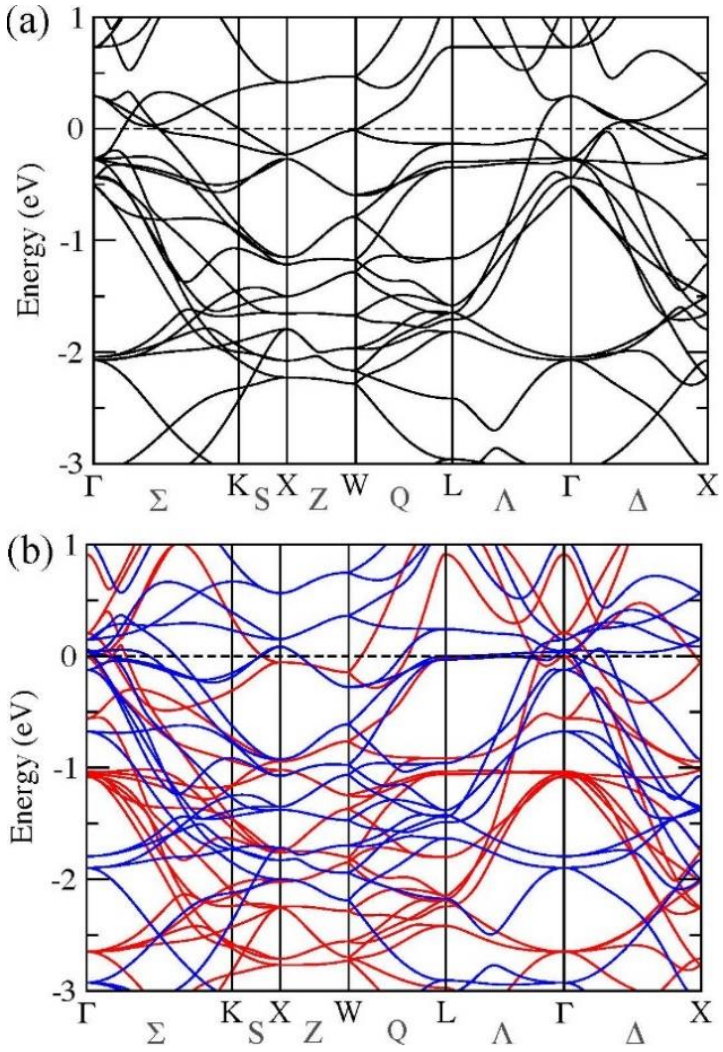

Fig. 4-18 Energy band structures of nonmagnetic $LuCo_2$ (a) and ferromagnetic $LuCo_2$ (b) along the symmetry axes in the Brillouin zone. The Fermi energy ε_F is set to zero. In (b), red and blue curves represent the up-spin and down-spin bands, respectively.

The Fermi surfaces of nonmagnetic and ferromagnetic $LuCo_2$ are illustrated in Figs. 4-20 (a) and 4-20 (b), respectively. The Fermi surfaces of nonmagnetic $LuCo_2$ are formed by the 40th, 41st, and 42nd bands. The 40th Fermi surface shows a multiply connected shape centered at the Γ point. The 41st Fermi surface forms a large bumpy sphere centered at the Γ point. The 42nd Fermi surface is composed of the surfaces centered at the X points.

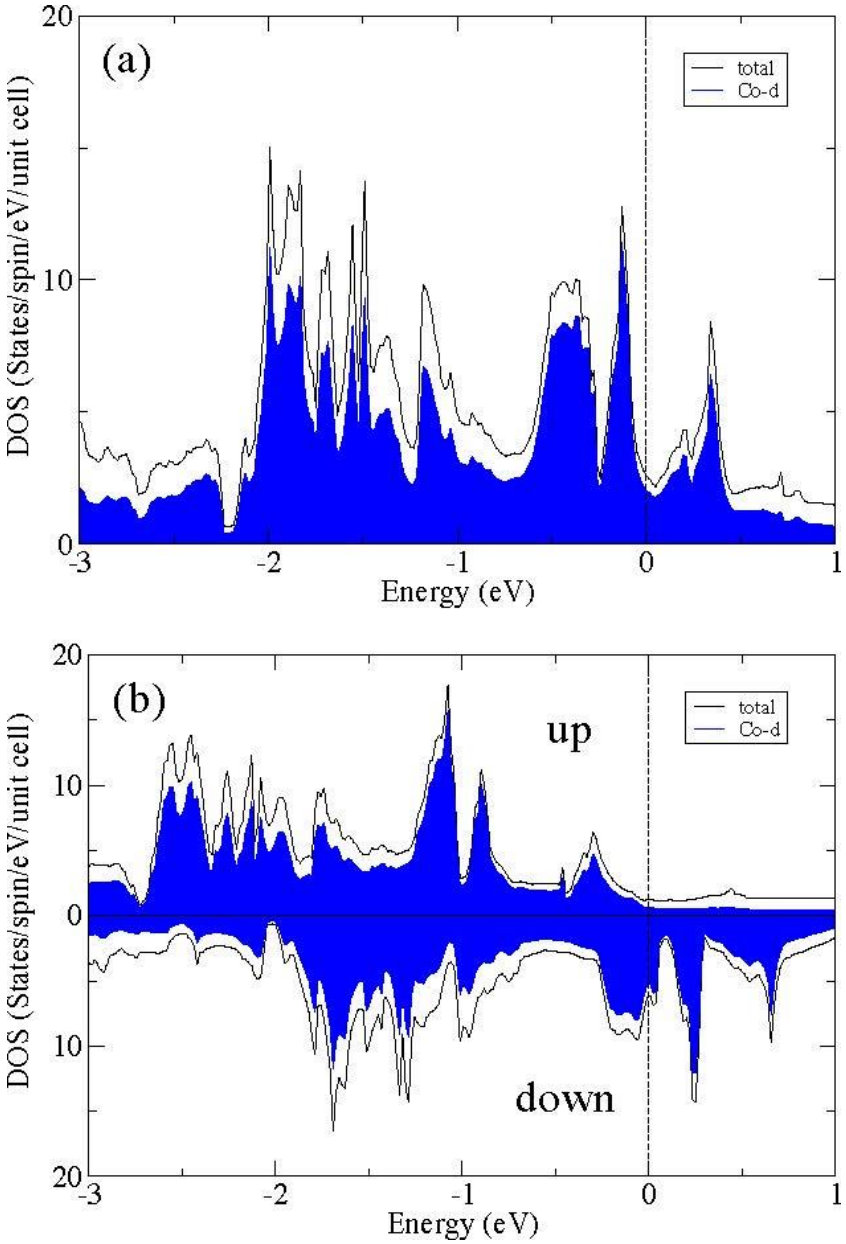

Fig. 4-19 Calculated DOS of nonmagnetic $LuCo_2$ (a) and ferromagnetic $LuCo_2$ (b). Black and blue painted curves represent the total and Co-*d* partial DOS, respectively.

The Fermi surfaces of ferromagnetic $LuCo_2$ are formed by the 43rd and 44th bands for the up-spin state and the 36th-40th bands for the down-spin state. The 43rd surface has a spherical shape centered at the Γ point with the tubes pointing along the Λ (ΓL) axis and connecting around the L point. The Fermi velocities on the tubes are quite large. The 44th surface shows a flat propeller-like shape centered at the X points. The Fermi velocity at the W point is considerably large. The 36th-38th Fermi surfaces are small spherical or connected spherical hole pockets around the Γ point. The 39th surface forms a large spherical shape centered at the Γ point with the tubes pointing along the Δ (ΓX) axis and connecting around the X point. The 40th surface shows a large spherical shape centered at the Γ point with the tubes pointing along the Δ (ΓX) and Λ (ΓL) axes and connecting around the X point and L point, respectively.

We calculated the DOS at the Fermi energy $N(\varepsilon_F)$, the root mean square of the Fermi velocity v_F, and the normal Hall coefficient R_N for nonmagnetic and ferromagnetic $LuCo_2$, which are listed in Table4-3. The $N(\varepsilon_F)$ of nonmagnetic $LuCo_2$ is comparable to that previously reported [18]. The $N(\varepsilon_F)$ of ferromagnetic $LuCo_2$ is larger than that of nonmagnetic $LuCo_2$. This is because the 39th Fermi surface and the 40th Fermi surface for the down-spin state make a significant contribution to the DOS in the ferromagnetic state. The Fermi velocity of nonmagnetic and ferromagnetic $LuCo_2$ is in the range of 0.16-0.20 × 10^8 cm/s. It is found that the normal Hall coefficients of both nonmagnetic and ferromagnetic $LuCo_2$ are positive with almost the same values of about 30 × 10^{-11} m^3/C.

The positive R_N of nonmagnetic $LuCo_2$ indicates that the positive (hole-like) contributions from the 40th and 41st surfaces are larger than the negative (electron-like) contribution from the 42nd surface. In the ferromagnetic state, the down-spin 39th large surface and the up-spin 43rd surface with the high Fermi velocities lead to the positive R_N.

Table 4-3 Calculated density of states (DOS) at Fermi energy $N(\varepsilon_F)$, the root mean square of the Fermi velocity v_F, and normal Hall coefficient R_N of nonmagnetic and ferromagnetic $LuCo_2$.

	Nonmagnetic $LuCo_2$	Ferromagnetic $LuCo_2$
$N(\varepsilon_F)$ [States/eV/unit cell]	5.509	7.175
v_F [10^8 cm/s]	0.167	0.201
R_N [10^{-11} m^3/C]	32.891	30.710

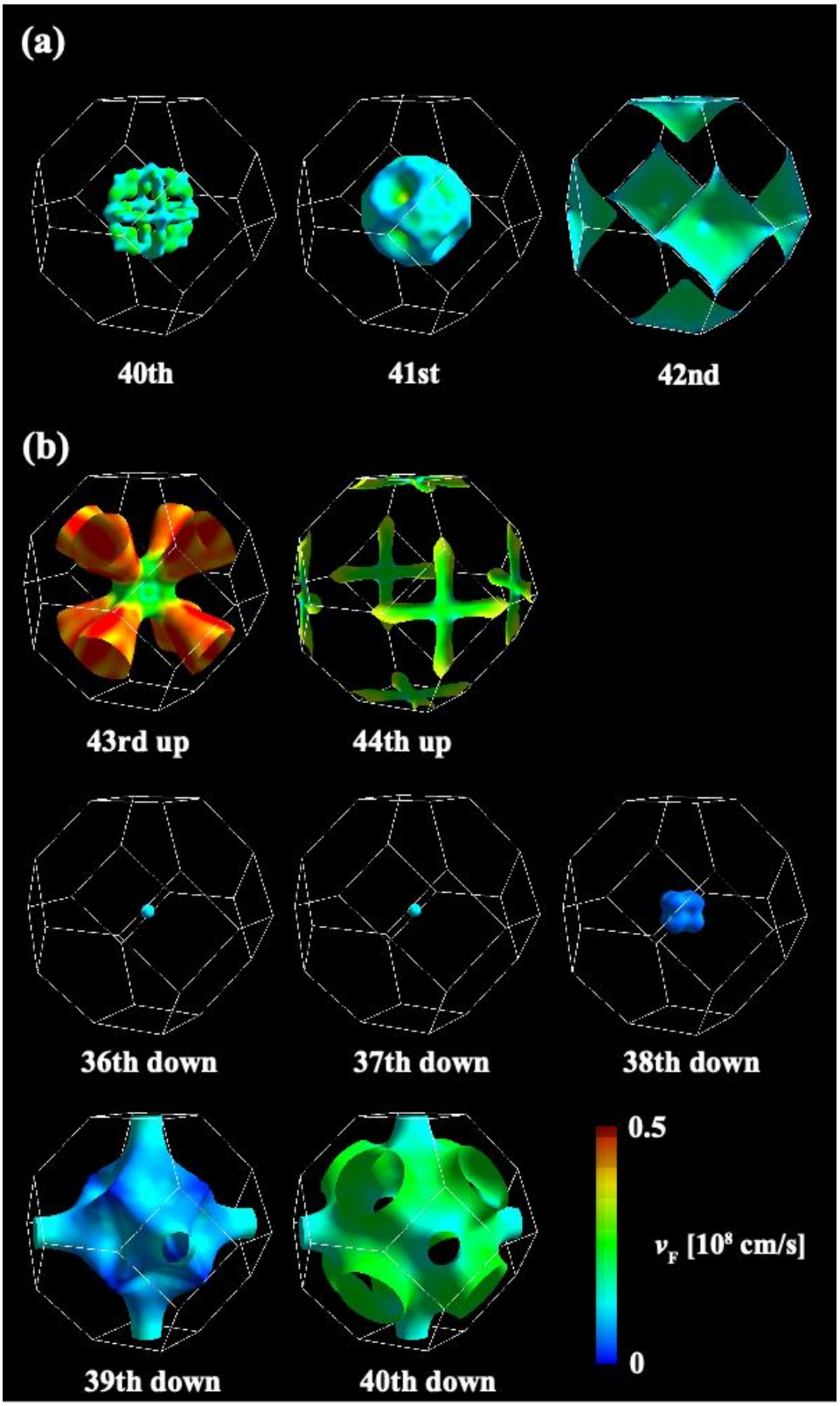

Fig. 4-20 Fermi surface and Fermi velocity of nonmagnetic $LuCo_2$ (a) and ferromagnetic $LuCo_2$ (b). In (b), up and down represent the up-spin and down-spin states, respectively. The inner side around the Γ point of all the Fermi surfaces is occupied by hole.

4.5 Discussion

First, we compare the experimental R_N's with the calculated ones and discuss their differences. The calculated R_N of ferromagnetic $LuCo_2$ is 30.7×10^{-11} m^3/C. We have two experimental data on R_N^f for RCo_2 in the present study: $ErCo_2$ and $Lu(Co_{0.91}Al_{0.09})_2$. In general, the energy level of 4*f* orbitals is far below the Fermi level. Therefore, 4*f* electrons do not affect the electronic state near the Fermi level. Er has eleven electrons in the 4f orbitals. It is quite difficult to calculate the energy band structure of $ErCo_2$ with satisfactory accuracy, because the crystal field effects for 4f electrons should be taken into account. In the case of Lu, the 4f orbitals are fully occupied, so that we can treat 4f electrons as core electrons. These electrons do not form the energy band, which enable us to calculate the energy band structure and hence the Fermi surface accurately. It is reasonable to compare the calculated R_N of ferromagnetic $LuCo_2$ with the experimental R_N^f of $ErCo_2$.

The R_N^f of $ErCo_2$ is about 35×10^{-11} m^3/C below T_C and 15×10^{-11} m^3/C above T_C. The origin of a sudden change in R_N^f at T_C is unclear. Above T_C, a ferrimagnetic state is induced by a magnetic field. The paramagnetic state below B_C may affect R_N^f of the ferrimagnetic state. For example, if some Er moments remain paramagnetic just above B_C due to concentration fluctuations or crystal imperfections, they decrease ρ_{xy} through the AHE and hence reduce R_N^f. In this sense, R_N^f determined below T_C seems to be more reliable. Accordingly, the calculated R_N for ferromagnetic $LuCo_2$ is in agreement with the experimental R_N^f of ferrimagnetic $ErCo_2$. In the case of $Lu(Co_{0.91}Al_{0.09})_2$, R_N^f is dependent on temperature. It increases from 10×10^{-11}m^3/C to 50×10^{-11}m^3/C with increasing temperature from 4.2 K to 70 K. The calculated R_N of ferromagnetic $LuCo_2$ is in the range of the R_N^f values. In this context, the agreement between the calculation and the experiments is satisfactory in the ferromagnetic state.

Quite recently, Huang *et al.* reported Hall effect of $TbCo_2$ and $DyCo_2$. [71]. They estimated the normal and anomalous Hall coefficients of these compounds at various temperatures. Temperature dependence of R_N of $TbCo_2$ and $DyCo_2$ are shown in Fig. 4-21 (in this figure, the normal Hall coefficient is represented as R_0). Note that μΩcm/T equals to 10^{-8} m^3/C. Their results indicate that R_N^f of these compounds is $20\sim30\times 10^{-11}$ m^3/C in the ferrimagnetic state below 100 K. These results are also in agreement with our calculated results. They reported that R_N^f changes the sign from positive to negative at high temperatures. The reason is not clear.

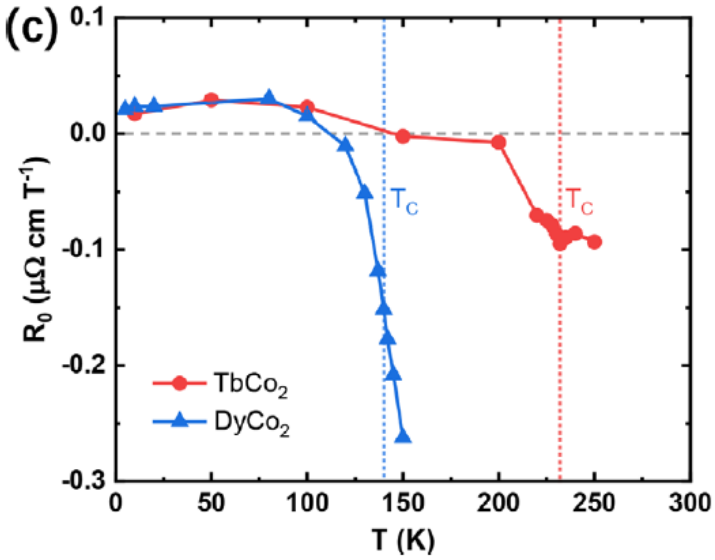

Fig. 4.21 Temperature dependence of the normal Hall coefficient (represented as R_0) of $TbCo_2$ and $DyCo_2$ [71].

The energy band calculations give $R_N = 32.9 \times 10^{-11}$ m^3/C for nonmagnetic $LuCo_2$. This value is close to that of ferromagnetic state. It is difficult to make a quantitative comparison between the calculated results and the experimental results of $LuCo_2$, because $R_N{}^p$ strongly depends on temperature. As shown in Table 4-2, $R_N{}^p$ of $LuCo_2$ is 106×10^{-11} m^3/C at 4.2 K, while it decreases to 24×10^{-11} m^3/C, when the temperature is raised to 70 K. As described in 1.6.1, the normal Hall coefficient is calculated in the constant τ approximation. The strong temperature dependence of $R_N{}^p$ of $LuCo_2$ suggests that $\boldsymbol{k}$ dependence of τ cannot be neglected. The main origins of τ are the impurity scattering and the electron-phonon scattering [72]. At very low temperatures, the impurity scattering is dominant and τ is isotropic [73]. At high temperatures, the scattering of electrons by phonons tends to be isotropic [74,75]. Therefore, eqs. (1.17)-(1.19) are applicable either at the low temperature limit or at the high temperature limit. Experimentally, R_{obs} seems to be temperature independent above 70 K. Though the calculated R_N is comparable to the roughly estimated value at 70 K, we should be very careful to reach a definite conclusion. To clarify the origin of temperature dependence of R_N of $LuCo_2$, further theoretical and experimental studies are necessary. The large R_N of paramagnetic $ErCo_2$ may be due to the same origin as the large R_N of $LuCo_2$ at low temperatures. We point out that the calculated R_N is positive, which is the same sign as the experimental results. This fact implies that the hole-like Fermi surfaces mainly contribute to the NHE in $LuCo_2$.

In contrast to $LuCo_2$, $R_N{}^p$ of $Lu(Co_{0.91}Al_{0.09})_2$ is negative. Therefore, $R_N{}^p$ changes the sign from positive to negative by the substitution of Al for Co in $LuCo_2$. We discuss the origin of the sign change in $R_N{}^p$ in the framework of a rigid-band approximation. We calculated R_N of nonmagnetic $LuCo_2$ by artificially shifting up the Fermi energy for the up-spin state and shifting down the Fermi energy for the down-spin state so as to maintain the total occupation number. The calculated R_N is shown as a function of the energy shift, Δε in Fig. 4-22. It is found that the normal Hall coefficient changes the sign from positive to negative at around Δε = 0.035 eV. With increasing Δε, R_N has a minimum value of -125×10^{-11}m^3/C at Δε = 0.085 eV and then increases. At

higher Δε, R_N becomes positive, again. The sign reversal of R_N originates in the change in Fermi surfaces. As described in section 4.4, the Fermi surfaces of nonmagnetic $LuCo_2$ consist of three bands. The 40th and 41st bands compose hole-like Fermi surfaces and the 42nd band makes an electron-like Fermi surface. The 40th and 41st Fermi surfaces are responsible for the positive R_N. When the Fermi level is shifted, the 40th and 41st bands are occupied more and their Fermi surfaces shrink. These bands are fully occupied at around Δε = 0.035eV. Further increase in Δε to 0.085 eV expands the 42nd electron-like surface, which gives a large negative R_N. We believe that Fermi level shift by the substitution of Al for Co is responsible for the negative $R_N{}^p$ of $Lu(Co_{0.91}Al_{0.09})_2$.

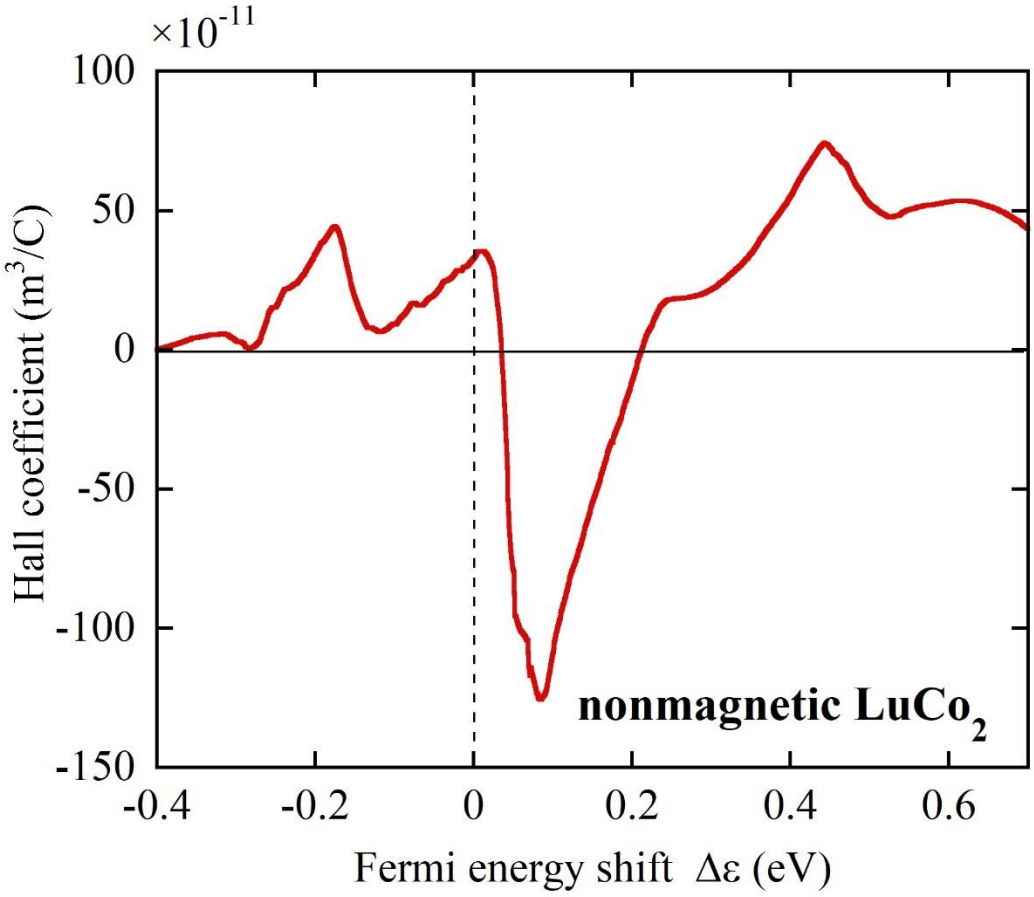

Fig. 4-22 Calculated normal Hall coefficient for nonmagnetic $LuCo_2$ as of shifting the Fermi energy.

Finally, we discuss on the sign change in the AHE of $ErCo_2$. Our results suggest that R_A of $ErCo_2$ is positive in the ferrimagnetic state, while it is negative in the paramagnetic state. The sign change in the AHE was reported for some rare-earth elements and compounds [76-78]. The temperature dependence of AHE of $TbAl_2$ is illustrated in Fig. 4-22 [78]. The compound has positive R_A at low temperatures. With increasing temperature, R_A initially increases and shows a maximum at around 0.6 T_C. Further increase in temperature causes a reduction in R_A and the AHE becomes negative above 0.7 T_C. Similar behavior was also observed for pure Dy [76] and

Tb [77], but no sign change in R_A was found for pure Gd [79]. These results suggest that the sign change in the AHE is associated with the non-zero orbital angular momentum of the 4*f* electrons. The sign change in R_A has been explained in terms of the impurity scattering. Kondo discussed the AHE on the basis of the $s - d$ (f) interaction [80]. Though he did not assume the presence of impurity, Maranzana pointed out that the asymmetric terms derived by Kondo can be regarded as the origin of skew scattering [81]. Giovannini found that another term, which was neglected by Kondo, can explain the sign change in the AHE in rare-earths [82]. Fert showed that, besides the skew scattering, the side-jump mechanism also contributes to the sign change in the AHE [83]. By combining these two mechanisms, he successfully explained the temperature dependence of the AHE of Tb. These models (skew scattering alone and skew scattering plus side-jump mechanism) are applied to ferromagnetic $TbAl_2$, which are shown by the lines in Fig. 4-22 [78]. Therefore, the sign change in the AHE in $ErCo_2$. can be understood in terms of the impurity scattering.

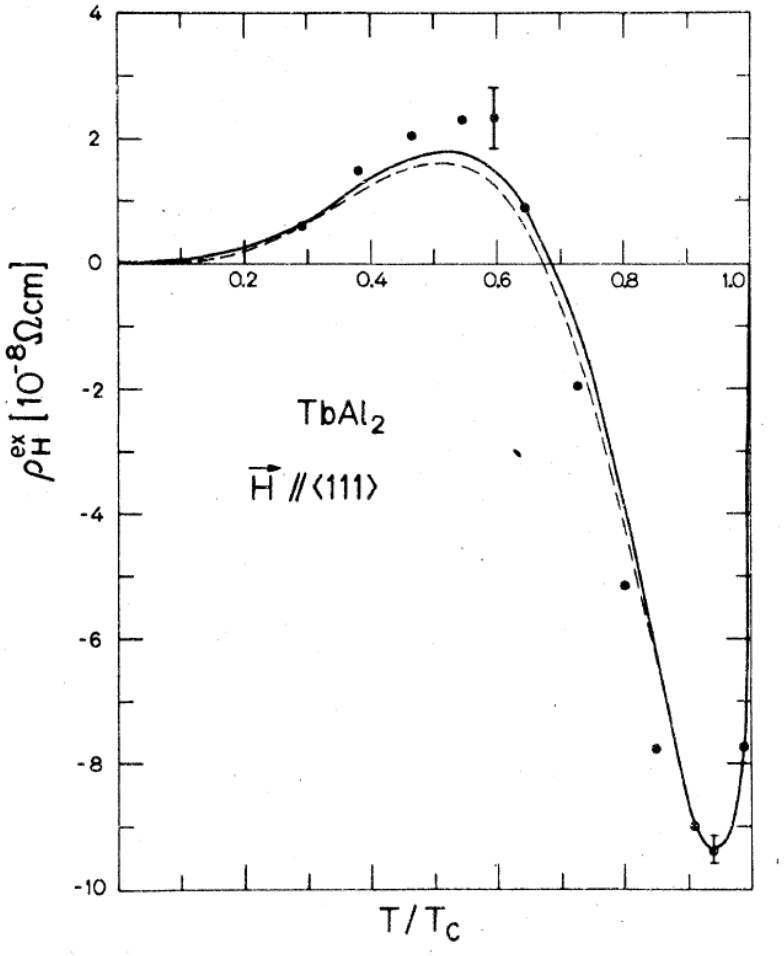

Fig. 4-22 Anomalous Hall resistivity of $TbAl_2$ below T_C. Closed circles represent the experimental values. A solid line is the calculated results by assuming skew scattering plus side-jump mechanism and a dashed line by assuming skew scattering alone [78].

Quite recently, Huang *et al.* reported the AHE of $DyCo_2$ and $TbCo_2$ [71]. Temperature dependence of R_A of $TbCo_2$ and $DyCo_2$ are shown in Fig. 4-23 (in this figure, the normal Hall coefficient is represented as R_H). These compounds show the positive AHE. No sign change in R_A was observed at around T_C. They discussed the AHE of $DyCo_2$ and $TbCo_2$ in terms of the intrinsic effect due to topology. In RCo_2, Co atoms form a kagome lattice. It is known that a kagome lattice can host non-trivial topological states due to geometrical frustration. These kagome magnets exhibit a large AHE due to the Berry phase effect [84]. Magnetic frustration does not exist in the Co sublattice of RCo_2. However, they claim noncoplanar magnetic structure can be realized in $DyCo_2$ and $TbCo_2$ at high temperatures, which can cause a large AHE near T_C. This speculation should be clarified. To understand the origin of AHE, further experimental and theoretical studies on Hall effect of RCo_2 are strongly desired.

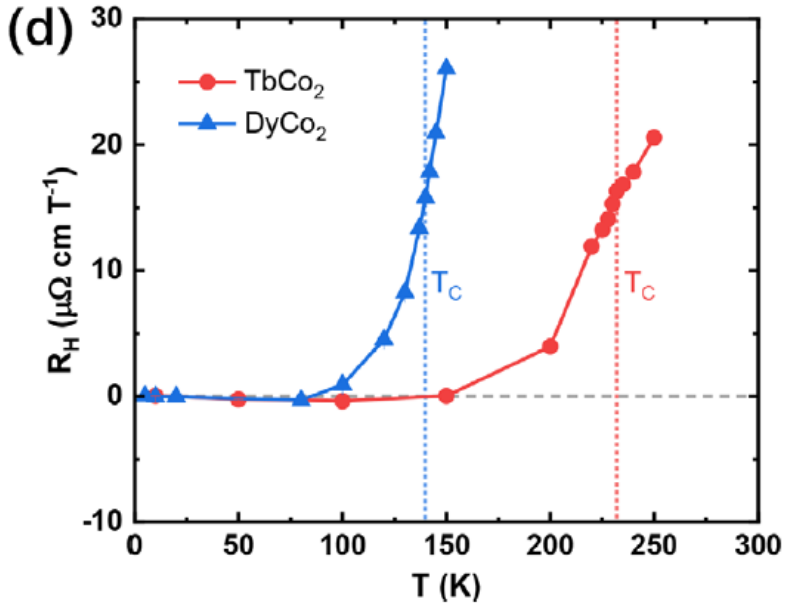

Fig. 4.23 Temperature dependence of the anomalous Hall coefficient (represented as R_H) of $TbCo_2$ and $DyCo_2$ [71].

In summary, we have studied the Hall effect of $Lu(Co_{0.91}Al_{0.09})_2$, $LuCo_2$ and $ErCo_2$. Assuming that R_A in the ferromagnetic state is the same as that in the paramagnetic state, we estimated R_N^f and R_N^p of $Lu(Co_{0.91}Al_{0.09})_2$. For $LuCo_2$, ρ_{xy} varies linearly with increasing field. Our analyses suggest that R_N^p of $LuCo_2$ is positive and temperature dependent. The $\rho_{xy} - B$ curves of $ErCo_2$ below T_C show ordinary ferromagnetic behavior with positive R_N^f and R_A. On the other hand, the $\rho_{xy} - B$ curves exhibit quite different behavior above T_C. The ρ_{xy} initially decreases with increasing field and shows a minimum, followed by abrupt increase at around B_C. We found that positive R_N^p and negative R_A can account for these $\rho_{xy} - B$ curves above T_C. These results are indicative of the sign change of R_A at T_C. We discussed the origin of the sign change of R_A in terms of the impurity scattering model of AHE. The calculated R_N of ferromagnetic $LuCo_2$ are comparable to R_N^f of

$Lu(Co_{0.91}Al_{0.09})_2$ and $ErCo_2$. On the other hand, the energy band calculations for nonmagnetic $LuCo_2$ give positive R_N, which is opposite in sign to the experimental $R_N{}^p$ of $Lu(Co_{0.91}Al_{0.09})_2$. We have shown that a slight shift of the Fermi energy causes the sign change of nonmagnetic R_N, from positive to negative in the framework of a rigid band approximation.

Chapter 5 Results and discussion on $La(Fe_{1-x}Si_x)_{13}$

5.1 Experimental results and analyses of $La(Fe_{1-x}Si_x)_{13}$

As shown in Fig. 1-14, the Curie temperature of $La(Fe_{1-x}Si_x)_{13}$ compounds is about 200 K, when they undergo the FOMT. In our apparatus, it is difficult to keep the temperature within ±0.1 K during the measurements above 200 K. Fujita *et al*. reported that applying pressure reduces T_C of $La(Fe_{1-x}Si_x)_{13}$ at a rate of 100 K/GPa for $x = 0.12$ [40]. Figure 5-1 shows our data of the temperature dependence of magnetization of $La(Fe_{0.88}Si_{0.12})_{13}$ at various pressures. The measurements were carried out in a field of 1.0 T. At ambient pressure, the compound undergoes the FOMT from a ferromagnetic state to a paramagnetic state at a 202 K. With increasing pressure to 1.0 GPa, T_C is decreased to 106 K . At $p = 1.0$ GPa, the FOMT is quite sharp accompanied by a large thermal hysteresis of about 20 K. Thus, we measured the Hall resistivity and magnetization of $La(Fe_{1-x}Si_x)_{13}$ with $x = 0.12$ and 0.10 at 0.5 GPa and 1.0 GPa.

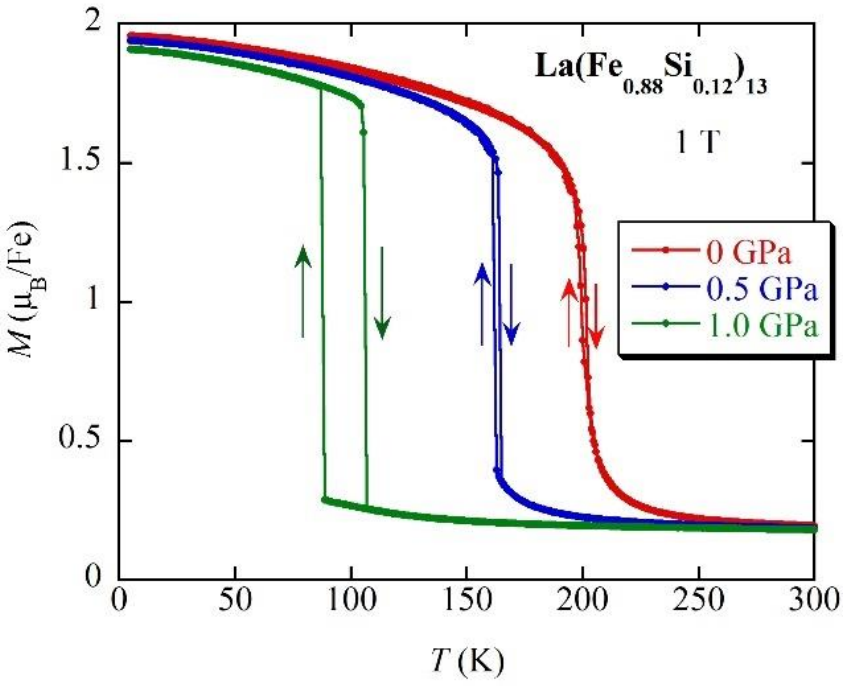

Fig. 5-1 Temperature dependence of magnetization of $La(Fe_{0.88}Si_{0.12})_{13}$ at various pressures.

The temperature dependence of ρ_{xy} of $La(Fe_{0.88}Si_{0.12})_{13}$ at 0.5 GPa is depicted in Fig. 5-2, together with the M – T curve. The measurements were carried out in a field of 1.0 T. The Hall resistivity is large at low temperatures and it increases with increasing temperature, followed by a sudden drop at T_C. Above T_C, ρ_{xy} exhibits a Curie-Weiss type tail, which was pointed out by Fujita and Takenaka [85]. Figure 5-3 displays the temperature dependence of ρ_{xx} of $La(Fe_{0.88}Si_{0.12})_{13}$ at 0.5 GPa. The compound shows a peak at T_C. Besides, the residual resistivity ρ_{xx0} is very large (~100 μΩ cm). These results are in agreement with the previous reports [86-88].

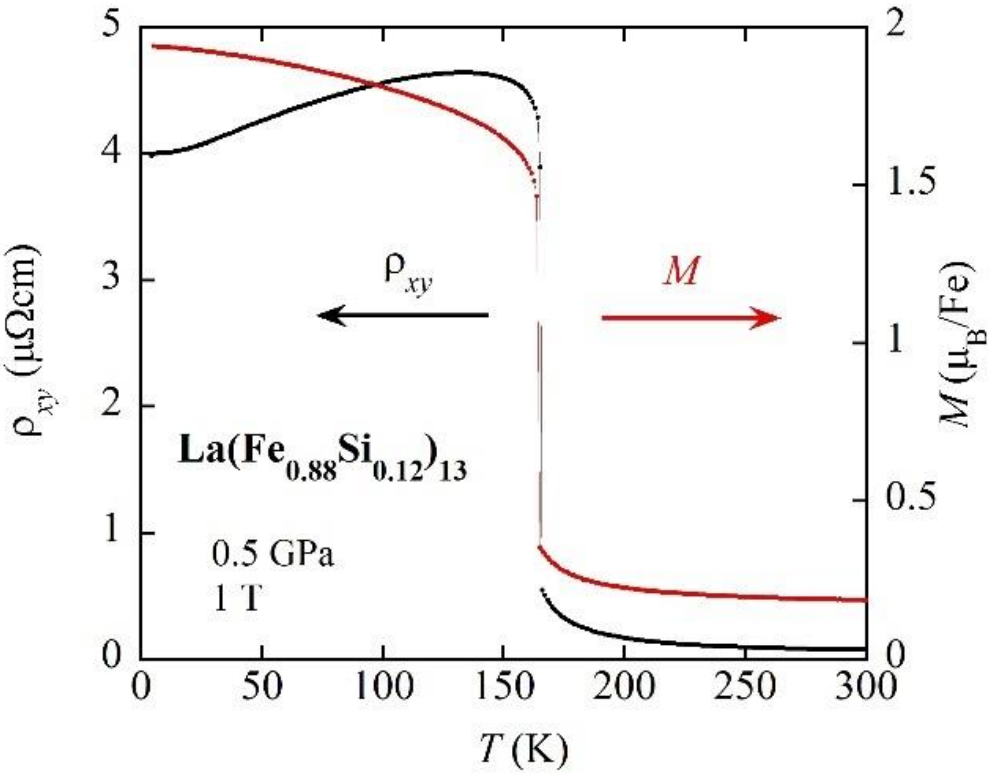

Fig. 5-2 Temperature dependences of ρ_{xy} and M of La(Fe$_{0.88}$Si$_{0.12}$)$_{13}$ at 0.5 GPa.

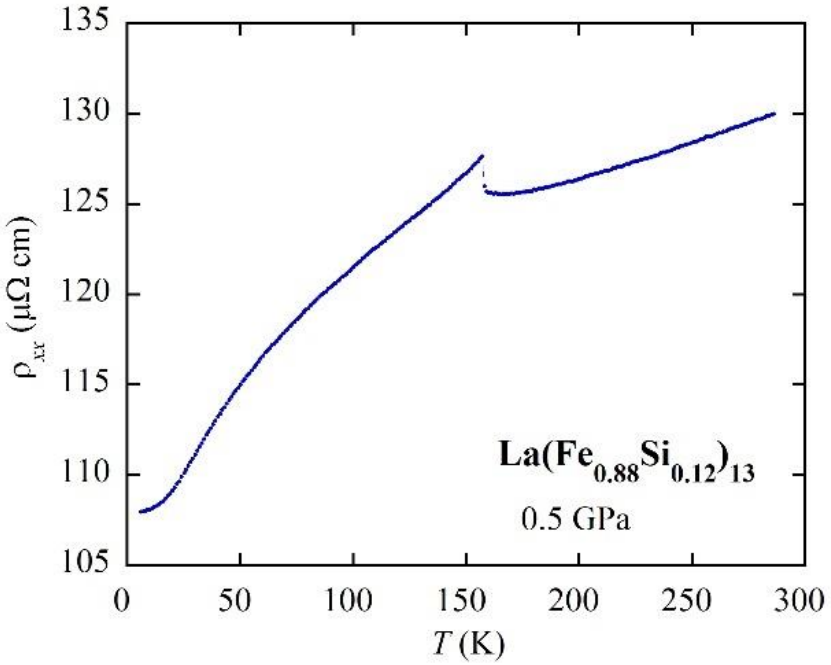

Fig. 5-3 Temperature dependence of the longitudinal resistivity, ρ_{xx} of La(Fe$_{0.88}$Si$_{0.12}$)$_{13}$ at 0.5 GPa.

The magnetization curves and the field dependence of the Hall resistivity of $La(Fe_{0.88}Si_{0.12})_{13}$ were measured at 1.0 GPa. The M – B curves at various temperatures are illustrated in Fig. 5-4. The compound exhibits ferromagnetic behavior at 4.2 K and 70 K. Above 105 K, IEM is observed. The metamagnetic transition is accompanied by a large hysteresis. In the paramagnetic state, the magnetization rapidly increases at low fields and it increases linearly with increasing field. A rapid rise in the magnetization originates in a ferromagnetic impurity α-Fe(Si), which was detected in the X-ray diffraction pattern. Since the Curie temperature of α-Fe(Si) is higher than room temperature, it is saturated at low magnetic fields. Therefore, a straight portion below B_C is attributable to intrinsic paramagnetic behavior of $La(Fe_{0.88}Si_{0.12})_{13}$. The field dependence of the Hall resistivity of $La(Fe_{0.88}Si_{0.12})_{13}$ at various temperatures is illustrated in Fig. 5-5. Below 70 K, ρ_{xy} increases rapidly at low field. This is due to the AHE. The results indicate that the AHE of $La(Fe_{0.88}Si_{0.12})_{13}$ is positive. At higher fields, ρ_{xy} tends to saturate. Above 105 K, ρ_{xy} is increased with increasing B in the paramagnetic state. When IEM takes place, ρ_{xy} shows a positive jump. We notice that the magnitude of AHE of $La(Fe_{0.88}Si_{0.12})_{13}$ is very large compared with that of the other systems in the present study. Especially at 4.2 K or 10 K, the magnitude of AHE are about 0.5×10^{-8} Ωm, 1.5×10^{-8} Ωm for $Co(S_{1-x}Se_x)_2$ and $Lu(Co_{0.91}Al_{0.09})_2$, respectively. On the other hand, that of $La(Fe_{0.88}Si_{0.12})_{13}$ is nearly 5×10^{-8} Ωm. As shown later, the AHE of $La(Fe_{0.90}Si_{0.10})_{13}$ is nearly the same as that of $La(Fe_{0.88}Si_{0.12})_{13}$. Therefore, the AHE of $La(Fe_{1-x}Si_x)_{13}$ is 3-10 times as large as that of the other systems. We point out that ρ_{xy} in Fig. 5-2 is mostly originates in the anomalous Hall resistivity. This is important for the analysis of the AHE in the following subsection.

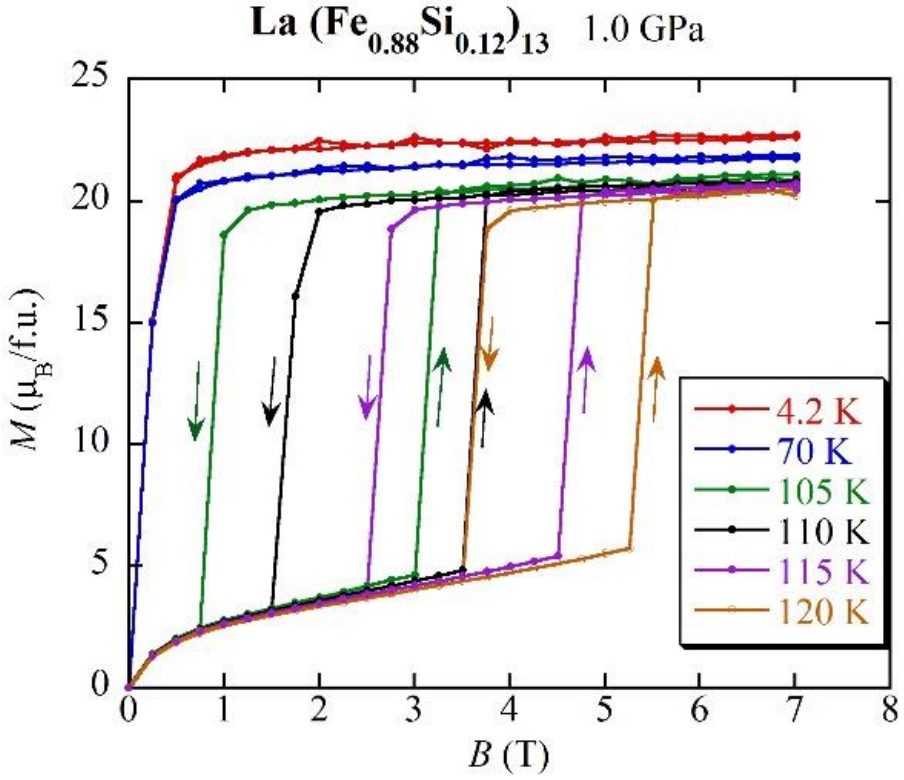

Fig. 5-4 M – B curves of $La(Fe_{0.88}Si_{0.12})_{13}$ at 1.0 GPa.

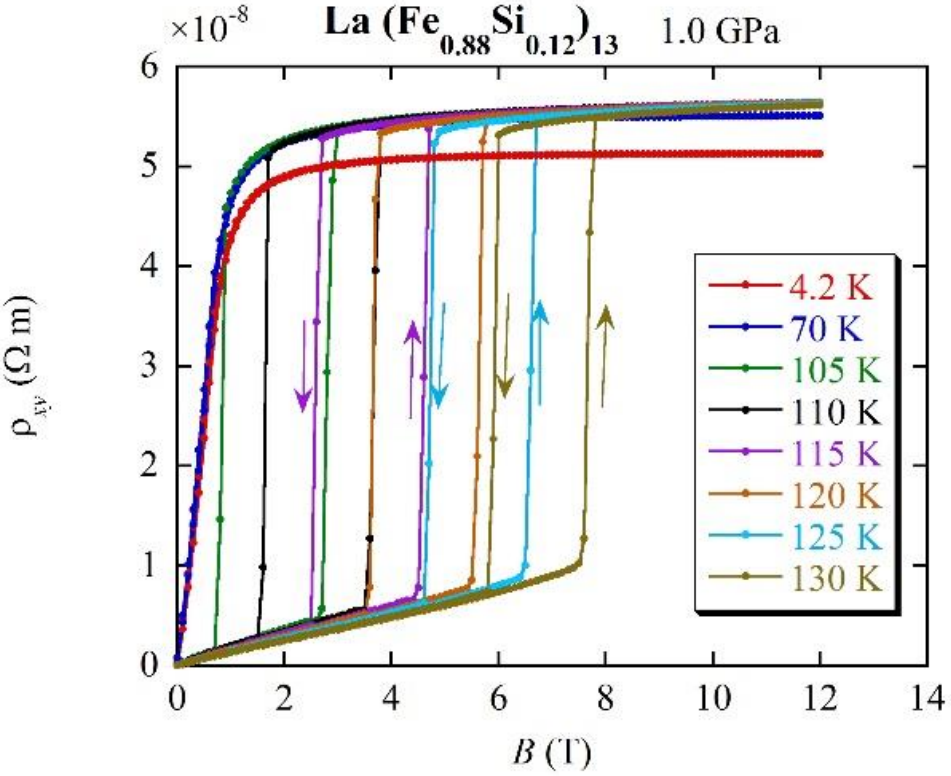

Fig. 5-5 $\rho_{xy} - B$ curves of $La(Fe_{0.88}Si_{0.12})_{13}$ at 1.0 GPa.

The magnetization curves of $La(Fe_{0.90}Si_{0.10})_{13}$ were measured just above T_C at 0.5 GPa, which are shown in Fig. 5-6. Between 155 K and 170 K, the $M - B$ curves show sharp IEM. In contrast to $La(Fe_{0.88}Si_{0.12})_{13}$, the magnetization of $La(Fe_{0.90}Si_{0.10})_{13}$ increases linearly in the paramagnetic state below B_C. These results suggest that the amount of ferromagnetic impurity is quite small for this sample. The $\rho_{xy} - B$ curves of $La(Fe_{0.90}Si_{0.10})_{13}$ were depicted in Fig. 5-7. Between 155 K and 170 K, ρ_{xy} increases first linearly and then more rapidly with increasing field in low fields. At B_C, the compound shows a large positive AHE. In high fields, the Hall resistivity tends to saturate. These features are similar to the $\rho_{xy} - B$ curves of $La(Fe_{088}Si_{0.12})_{13}$.

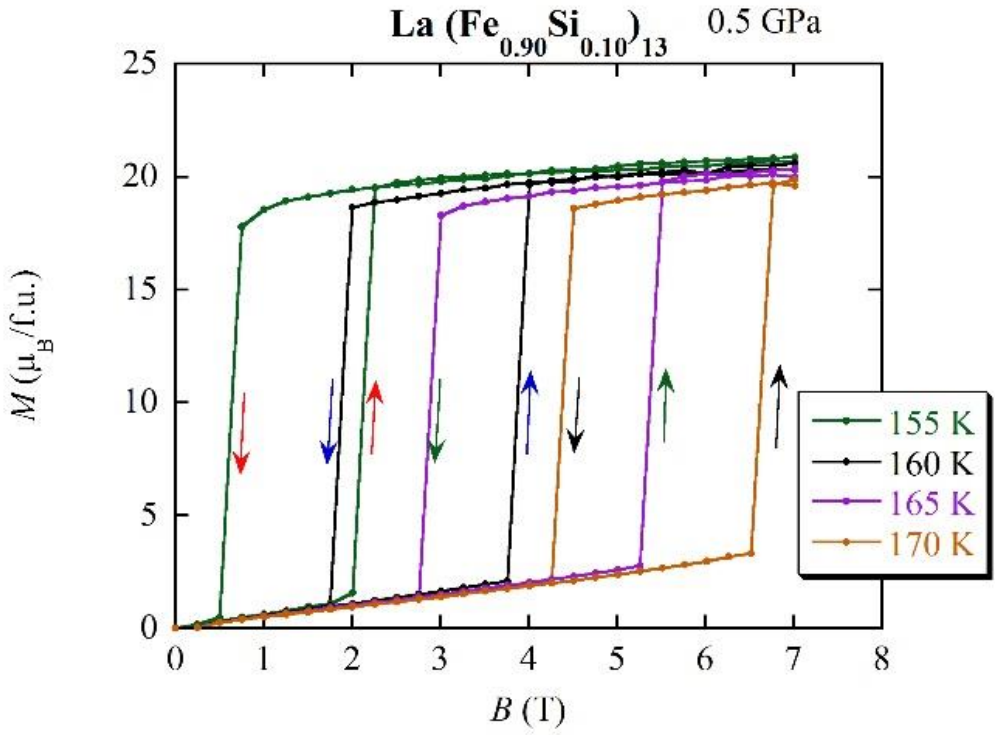

Fig. 5-6 $M - B$ curves of $La(Fe_{0.90}Si_{0.10})_{13}$ at 0.5 GPa.

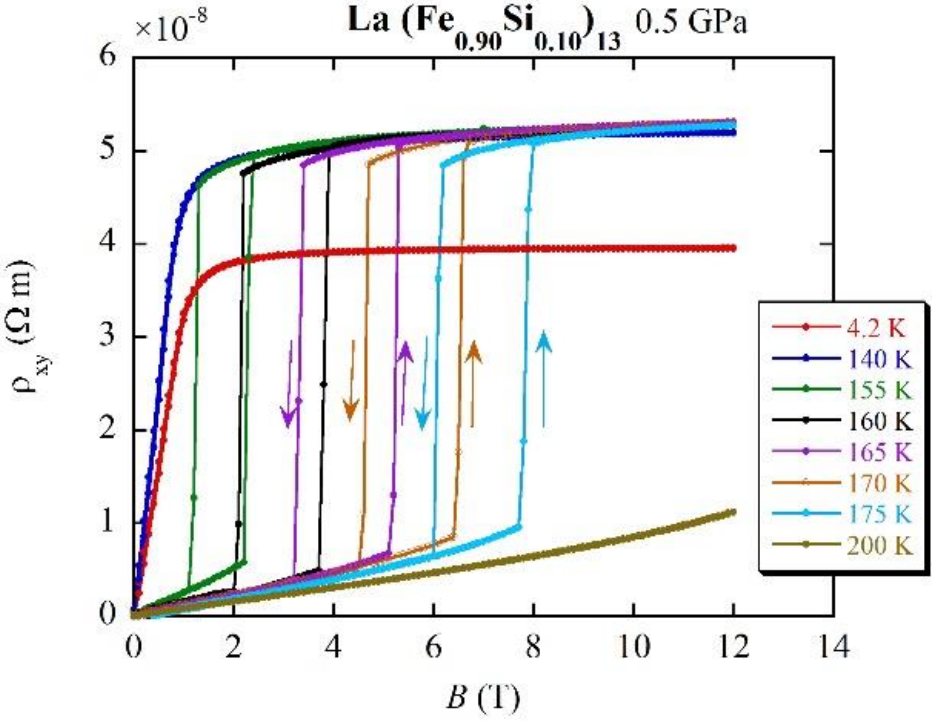

Fig. 5-7 $\rho_{xy} - B$ curves of $La(Fe_{0.90}Si_{0.10})_{13}$ at 0.5 GPa.

Fujita *et al.* measured the $\rho_{xy} - B$ curves of $La(Fe_{0.88}Si_{0.12})_{13}$ under pressures, independently. Their results at a pressure of 1.2 GPa are shown in Fig. 5-8, which are in qualitatively agreement our results [89].

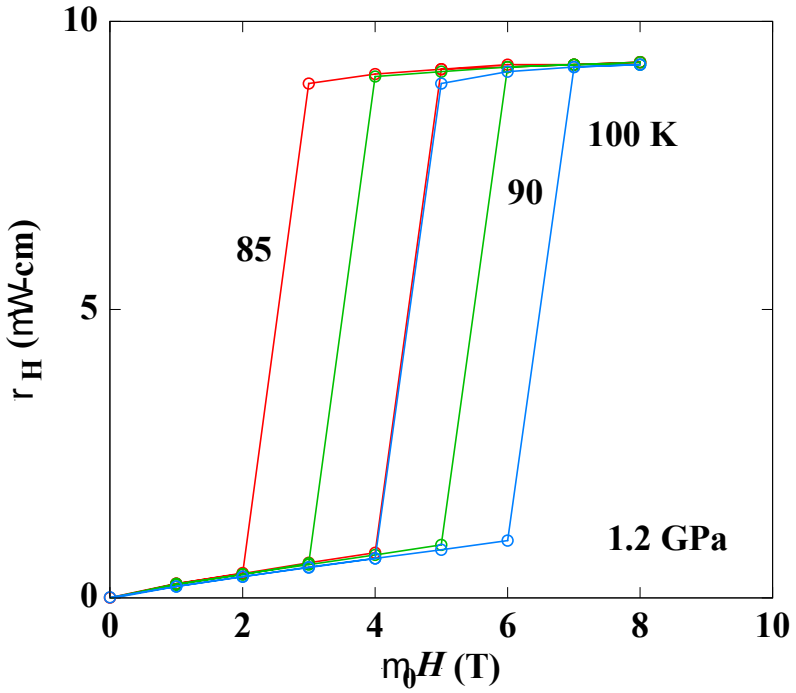

Fig. 5-8 The $\rho_{xy} - B$ curves of $La(Fe_{088}Si_{0.12})_{13}$ at a pressure of 1.2 GPa measured by Fujita [89].

As will be discussed in the following section, it is inadequate to assume that R_A in the ferromagnetic state equals to that in the paramagnetic state in $La(Fe_{1-x}Si_x)_{13}$. Thus, we analyzed the Hall resistivity of $La(Fe_{1-x}Si_x)_{13}$ only in the ferromagnetic state. We found that ρ_{xy} in the ferromagnetic state is not well approximated by eq. (3.3) ($\rho_{xy} = \rho_{xy}^0 + R_{obs}B$). Then, we analyzed the Hall resistivity of $La(Fe_{1-x}Si_x)_{13}$ on the basis of eq. (4.1) ($\rho_{xy}/B = R_N + R_A M/B$). For the ρ_{xy}/B vs. M/B plots, we adopted the data in both field-increasing and field-decreasing processes in a wide field region of the ferromagnetic state. As described previously, the magnetization of $La(Fe_{0.88}Si_{0.12})_{13}$ is affected by the ferromagnetic impurity. We use both the raw data and the corrected data for the analyses. The correction was made by subtracting a ferromagnetic component from the measured magnetization by assuming a linear dependence on B in the paramagnetic state. Typical examples of the ρ_{xy}/B vs. M/B plots are illustrated in Figs. 5-9 (a) - (c). In Fig. 5-9 (a), the plots of $La(Fe_{0.88}Si_{0.12})_{13}$ at 110 K are given with the raw M data (red symbols) and the corrected M data (blue symbols). Solid lines represent least squares fits of straight lines to the data, from which R_N^f and R_A were determined. We confirmed that Pearson correlation coefficient is higher than 0.9995 for all the least squares fittings.

The temperature dependence of R_N^f for $La(Fe_{0.88}Si_{0.12})_{13}$ and $La(Fe_{0.90}Si_{0.10})_{13}$ are shown in Fig. 5-10 (a) and 5-10 (b), respectively. For $La(Fe_{0.88}Si_{0.12})_{13}$, we got the intercepts of the ρ_{xy}/B vs. M/B plots with and without

correction for the magnetization and adopt the mean value as R_N^f. Large error bars in Fig. 5-10 (a) are due to inaccuracy in correction of the magnetization. Error bars in Fig. 5-10 (b) are obtained from 95% confidence intervals in the least squares regression. For $La(Fe_{0.88}Si_{0.12})_{13}$, R_N^f is positive at low temperatures, while it suddenly decreases at around 100 K. Above 110 K, R_N^f becomes negative. Similar sign change in R_N^f is observed for $La(Fe_{0.90}Si_{0.10})_{13}$ at around T_C, though the data were available in the narrow temperature range near T_C.

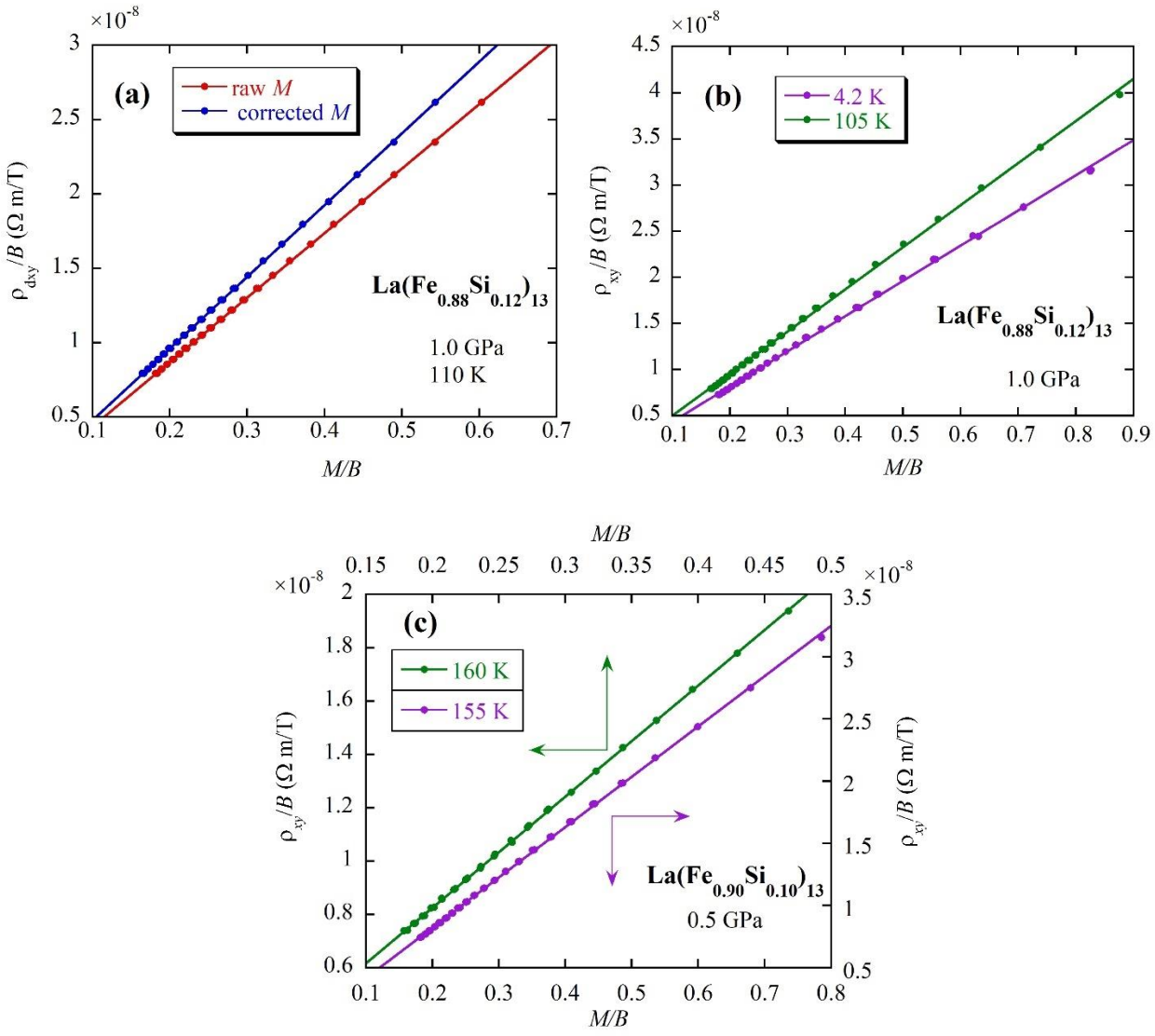

Fig. 5-9 (a) ρ_{xy}/B vs. M/B plots of $La(Fe_{0.88}Si_{0.12})_{13}$ at 110 K. Red and blue symbols represent the plots with the raw M data and the corrected M data, respectively. (b) The plots of $La(Fe_{0.88}Si_{0.12})_{13}$ at 4.2 K and 105 K. The corrected M data were used for analyses. (c) The plots of $La(Fe_{0.90}Si_{0.10})_{13}$ at 155 K and 160 K. Solid lines represent least squares fits of straight lines to data.

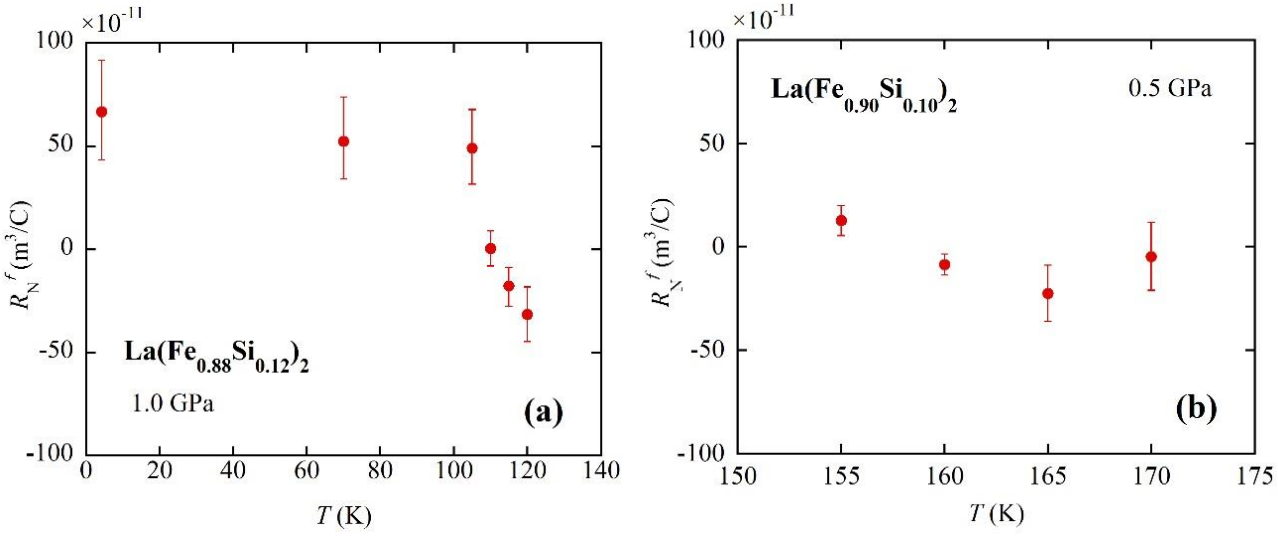

Fig. 5-10 Temperature dependence of R_N^f for $La(Fe_{0.88}Si_{0.12})_{13}$ (a) and $La(Fe_{0.90}Si_{0.10})_{13}$ (b).

The temperature dependence of R_A for $La(Fe_{0.88}Si_{0.12})_{13}$ and $La(Fe_{0.90}Si_{0.10})_{13}$ are shown in Figure 5-11. For both compounds, R_A increases with increasing temperature in the temperature range studied.

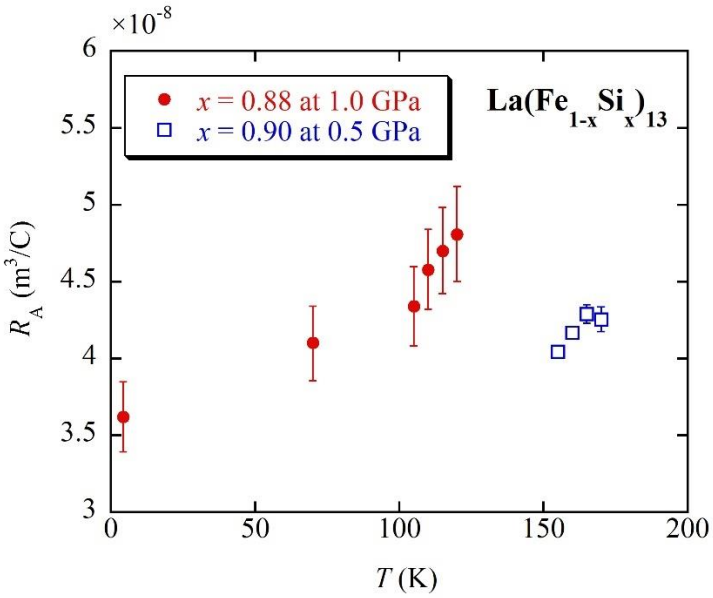

Fig. 5-11 Temperature dependence of R_A of $La(Fe_{0.88}Si_{0.12})_{13}$ and $La(Fe_{0.90}Si_{0.10})_{13}$.

Figure 5-12 displays the magnetoresistance (MR) (MR – B curves) of $La(Fe_{0.88}Si_{0.12})_{13}$ between 110 K and 130 K. The MR is defined as $\mathrm{MR} = \{r_{xx}(B) - r_{xx}(0)\} / r_{xx}(0)$, where r_{xx} is the transverse resistivity. The MR – B curves exhibit a positive jump associated with IEM. This is consistent with the temperature dependence of the

longitudinal resistivity (Fig. 5-3), in which the ferromagnetic state has higher resistivity than the paramagnetic state. Above B_C, the MR decreases with increasing field. This is probably because the electron-magnon scattering is suppressed in high fields.

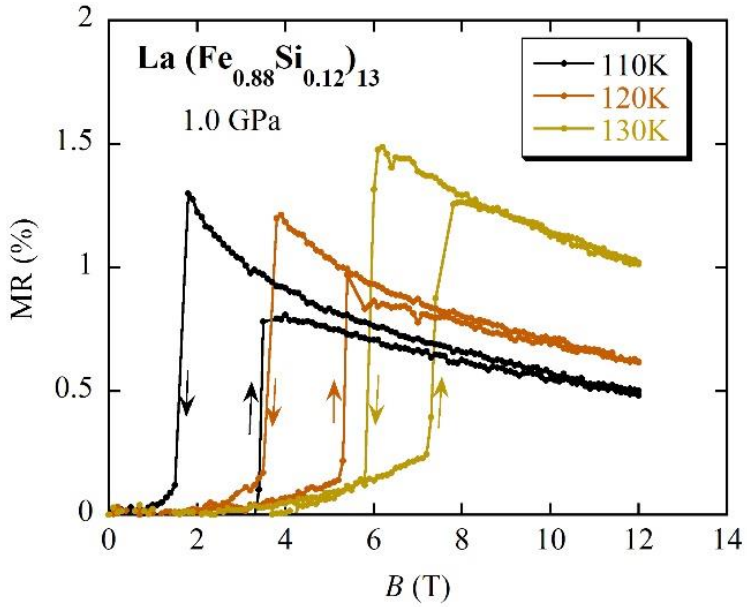

Fig. 5-12 Magnetoresistance (MR) curves of $La(Fe_{0.88}Si_{0.12})_{13}$ between 110 K and 130 K at 1.0 GPa.

5.2 Discussion

First, we discuss the AHE of $La(Fe_{1-x}Si_x)_{13}$. Karpenkov *et al*. reported Hall effect of $LaFe_{11.5}Si_{1.5}$ [88]. This composition corresponds to $x = 0.885$ in our notation, $La(Fe_{1-x}Si_x)_{13}$ and T_C of the compound is about 210 K. The $\rho_{xy} - B$ curves of the compound at ambient pressure are shown in Fig. 5-13. They did not observe IEM at 220 K but the reason is unclear.

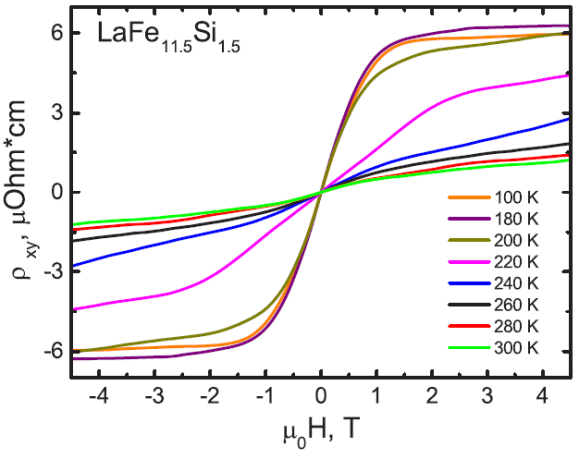

Fig. 5-13 The $\rho_{xy} - B$ curves of $LaFe_{11.5}Si_{1.5}$ at ambient pressure reported by Karpenkov *et al*. [88].

To separate the intrinsic and extrinsic contributions to the AHE, Karpenkov *et al*. used Tian–Ye–Jin scaling model [90], which is given by,

$$\rho_{xy} = \alpha\rho_{xx0} + \beta\rho_{xx0}^2 + b\rho_{xx}^2, \quad (5.1)$$

where ρ_{xx0} is the residual resistivity and α, β and b are coefficients. Originally, this equation was proposed empirically from the analyses of AHE of Fe thin films with different thickness. In this equation, $b\rho_{xx}^2$ comes mostly from the intrinsic contribution due to Berry phase effect and $\alpha\rho_{xx0}$ term represents the extrinsic skew scattering. Moreover, $\beta\rho_{xx0}^2$ term is attributable to the skew scattering plus side jump contribution. Karpenkov *et al*. applied eq. (5.1) to their results. As shown in Fig. 5-3, ρ_{xx0} is very large for $La(Fe_{1-x}Si_x)_{13}$, so that β is expected to very small. Assuming that β is negligibly small, they fit eq. (5.1) to their data and obtained α and b. As a result, they concluded that the intrinsic contribution is about 50 % of the total AHE. To validate their estimation, we applied Tian–Ye–Jin scaling model to our data. Figure 5-14 illustrates the ρ_{xy} – ρ_{xx} plot of $La(Fe_{0.88}Si_{0.12})_{13}$ at 0.5 GPa. The red circles represent the experimental data shown in Figs. 5-2 and 5-3. The black symbols are the calculated results by least square fitting eq. (5-1) to the data between 40 K and 90 K. The coefficients determined are $\alpha = 15.6 \times 10^{-3}$ and $b = 0.195 \times 10^{-3}$ $\mu\Omega^{-1}cm^{-1}$. These values give the intrinsic term $b\rho_{xx}^2$ is about 60% of the total AHE in this temperature range. However, this discussion is insufficient to conclude that the intrinsic contribution is dominant in the AHE of $La(Fe_{1-x}Si_x)_{13}$, because the temperature range for goof fit is limited between 40 K and 90 K. Moreover, a different scaling for AHE has been proposed after Tian–Ye–Jin scaling model [91, 92].

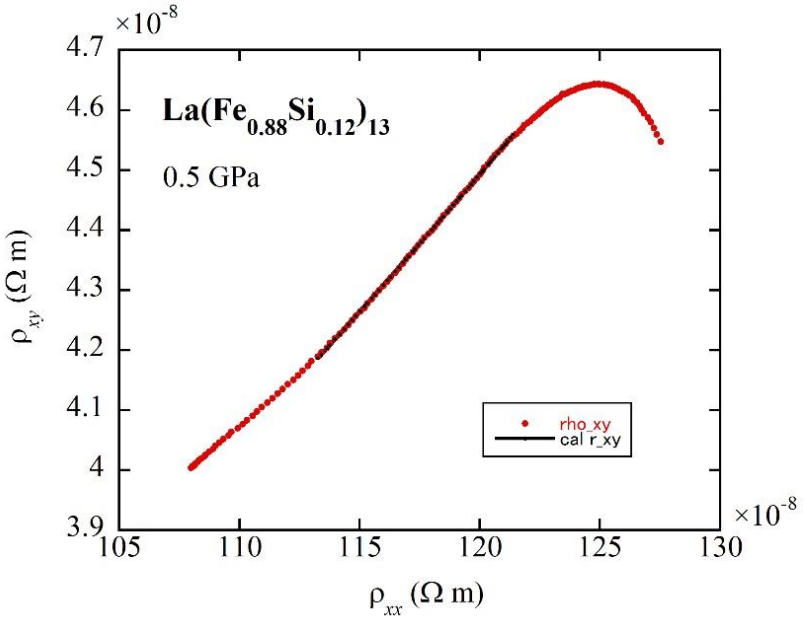

Fig. 5-14 The ρ_{xy} – ρ_{xx} plots of $La(Fe_{0.88}Si_{0.12})_{13}$ at 0.5 GPa. Red symbols represent the experimental data in Figs. 5-2 and 5-3. Black symbols are calculated results by least square fitting eq. (5-1) to the data between 40 K and 90 K.

Karpenkov *et al*. also calculated the anomalous Hall conductivity (AHC) based on the electronic structure of $LaFe_{11.5}Si_{1.5}$ [88]. The first-principle energy band calculations were carried out using VASP code. They estimated the intrinsic AHC following the Kubo-Středa formula. Furthermore, the side jump contribution was also evaluated. To discuss the effect of Co substitution on the AHC, they calculated the AHC by shifting the Fermi energy in the rigid band approximation.(Fig.5-15) It is found that the intrinsic AHC σ_{xy}^{int} is about 200 S/cm for $LaFe_{11.5}Si_{1.5}$ (at energy shift = 0). The correspondence intrinsic anomalous Hall resistivity ρ_{xy}^{int} = 2.9 μΩ cm (note that $\sigma_{xy} = \rho_{xy}/\rho_{xx}^2$). This value is more than 50 % of the total ρ_{xy} of $La(Fe_{0.88}Si_{0.12})_{13}$. These results seem convincing to conclude the intrinsic contribution is dominant in the AHE of $La(Fe_{1-x}Si_x)_{13}$. By shifting the Fermi energy, σ_{xy}^{int} is increased to 350 S/cm (ρ_{xy}^{int} = 4.3 μΩ cm). The calculated results indicate the AHE is sensitive to the fine structure near the Fermi level even in the ferromagnetic state. As shown in the previous chapters, IEM is accompanied by drastic changes in the electronic structure. Figure 5-16 illustrates the DOS curves of $LaFe_{11.5}Si_{1.5}$ in the ferromagnetic state as well as in the paramagnetic state reported by Gruner *et al.* [93]. Significant differences between two DOS curves are visible, which suggest that considerable changes in the electronic structure take place at T_C. From these results, we conclude that R_A of $La(Fe_{1-x}Si_x)_{13}$ is strongly dependent on the magnetic state.

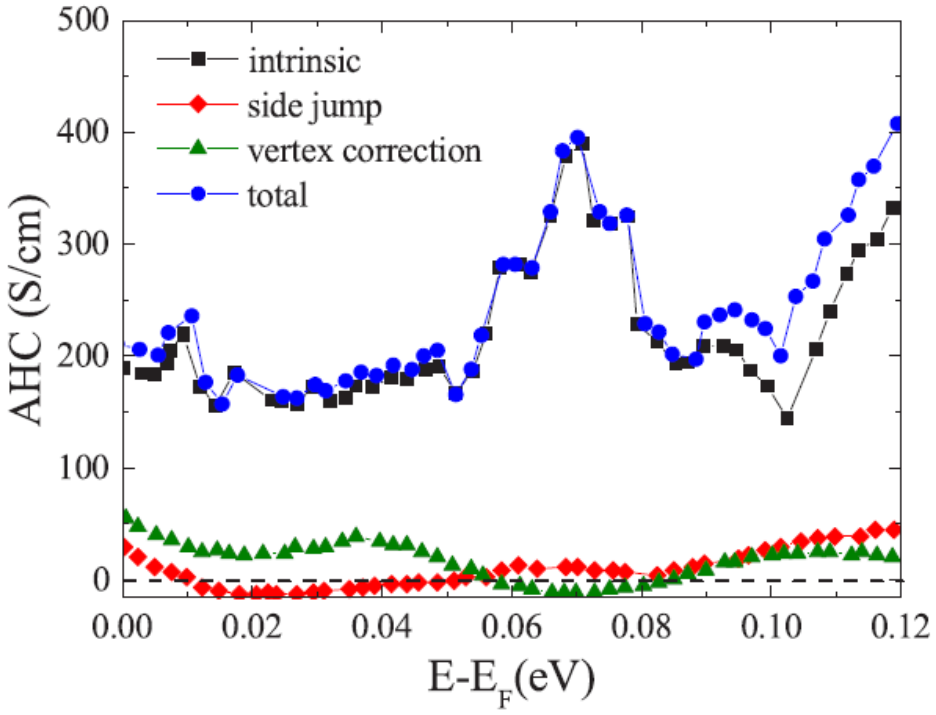

Fig. 5-15 Calculated anomalous Hall conductivity of $LaFe_{11.5}Si_{1.5}$ as shifting Fermi energy [88].

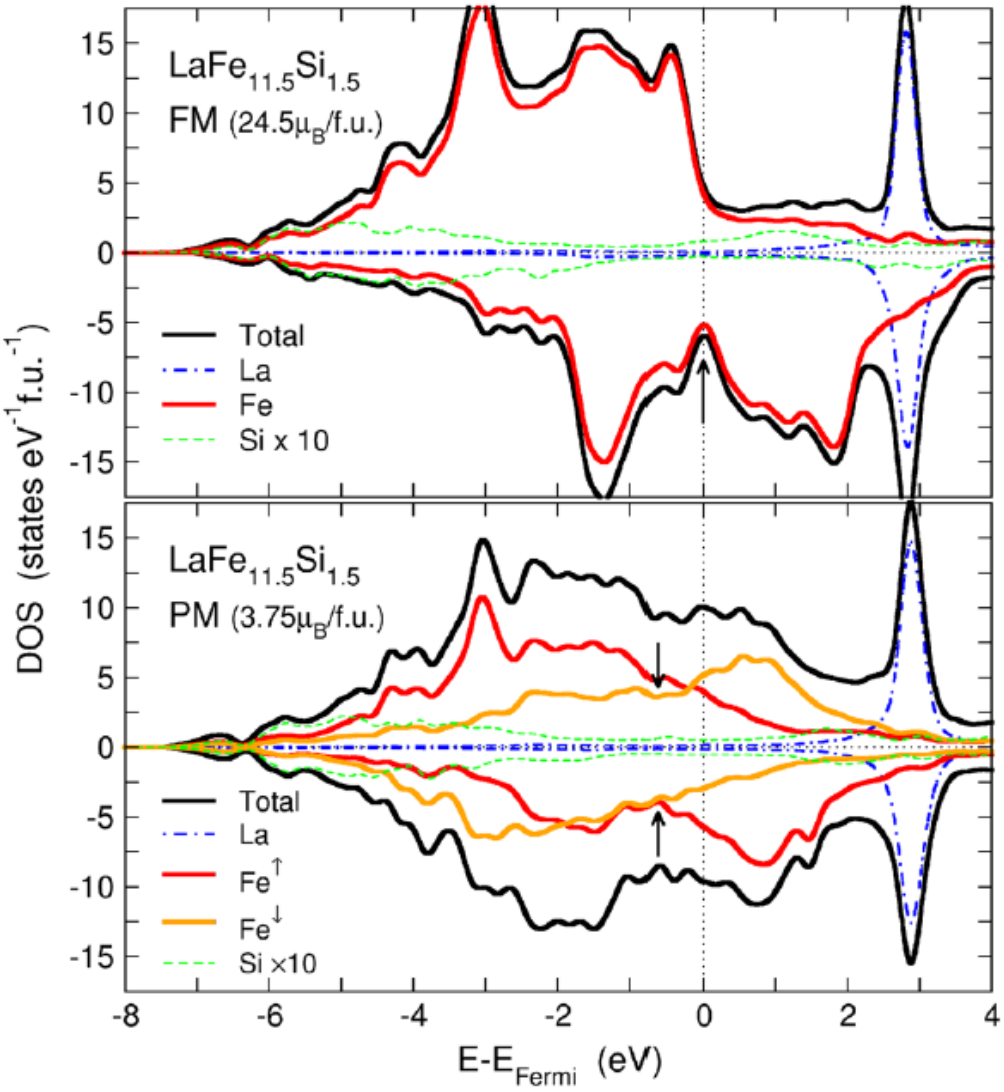

Fig.5-16 Total and partial DOS of $LaFe_{11.5}Si_{1.5}$ for ferromagnetic (upper panel) and paramagnetic (lower panel) states [93].

Next, we briefly discuss R_N^f of $La(Fe_{1-x}Si_x)_{13}$. $La(Fe_{0.88}Si_{0.12})_{13}$ has positive R_N^f at low temperatures, while R_N^f is decreased around 100 K and it changes a sign to negative above 110 K. $La(Fe_{0.90}Si_{0.10})_{13}$ also shows the sign change from positive to negative around T_C, though the absolute value is small compared with $La(Fe_{0.88}Si_{0.12})_{13}$. These results indicate that the hole contribution to the NHE is dominant at low temperatures, while the electron contributions become larger at around T_C. According to two carrier model, the normal Hall coefficient is given by eq. (1.15), $R_N = (n_h\mu_h^2 - n_e\mu_e^2) / \{e(n_h\mu_h + n_e\mu_e)^2\}$. The sign of R_N depends on the product of the carrier density n_h (n_e) and square of the carrier mobility μ_h^2 (μ_e^2). Since the carrier density is independent of temperature, the temperature dependence of R_N is attributable to the carrier mobility. Our results suggest that the electron mobility μ_e decreases more slowly that the hole mobility μ_h does with increasing temperature. For further discussion, the calculations of R_N^f of $La(Fe_{1-x}Si_x)_{13}$ based on the electronic structure is desired.

Finally, we comment on the positive MR of $La(Fe_{0.88}Si_{0.12})_{13}$. Previously, we observed similar positive MR jump associated with IEM in $Co(S_{1-x}Se_x)_2$. We pointed out that the increase in ρ in the ferromagnetic state originates in a distinct reduction of DOS at the Fermi level $N(\varepsilon_F)$ [63]. As shown in Table 3-2, $N(\varepsilon_F)$ of ferromagnetic CoS_2 is less than half of that of nonmagnetic CoS_2. This is because ferromagnetic CoS_2 is half-metallic, in which only the up-spin bands form the Fermi surfaces. Therefore, IEM of $Co(S_{1-x}Se_x)$ is accompanied by sudden decrease in the number of charge carriers. In other words, Fermi surfaces shrinks at the FOMT from the paramagnetic state to the ferromagnetic state, which gives a positive jump in the MR curve. This scenario is also applicable to $La(Fe_{1-x}Si_x)_{13}$. As shown in Fig. 5-15, the Fe 3*d* bands are almost occupied in the ferromagnetic state. Consequently, $N(\varepsilon_F)$ in the ferromagnetic state is nearly twice as large as that in the paramagnetic state. Similar DOS curves of $La(Fe_{1-x}Si_x)_{13}$ were reported by different groups [94, 95]. We believe that the reduction in the number of charge carriers is responsible for the positive jump in the MR curve associated with IEM.

In conclusion, $La(Fe_{1-x}Si_x)_{13}$ shows the large AHE. As discussed by Karpenkov *et al*., it is plausible that this AHE originates in the intrinsic Hall effect. Therefore, it is difficult to assume that R_A of the ferromagnetic state equals to that of the paramagnetic state in the present system. We analyzed the $\rho_{xy} - B$ curves in the ferromagnetic states and obtained R_N^f and R_A. It is found that R_N^f changes a sign from positive to negative near T_C. These results indicate the hole contribution to the NHE is dominant at low temperatures, while the electron contribution becomes significant at high temperatures. The $La(Fe_{1-x}Si_x)_{13}$ compounds show positive magnetoresistance. This is are attributable to a sudden reduction of $N(\varepsilon_F)$ caused by IEM.

Chapter 6 Conclusions

We have studied Hall effect of itinerant electron systems, $Co(S_{1-x}Se_x)_2$, $Lu(Co_{1-x}Al_x)_2$, $ErCo_2$ and $La(Fe_{1-x}Si_x)_{13}$. Following conclusions are obtained from chapters 3-5.

1. The field dependence of the Hall resistivity has been measured for $Co(S_{1-x}Se_x)_2$ with $0.08 \leq x \leq 0.14$. Assuming that R_A is independent of the magnetic state, we estimated the normal Hall coefficient in the ferromagnetic state $R_N{}^f$ and that in the paramagnetic state $R_N{}^p$ of $Co(S_{1-x}Se_x)_2$ It is found that $R_N{}^f$ is 30-40 $\times 10^{-11}$ m^3/C and $R_N{}^p$ is 10-20 $\times 10^{-11}$ m^3/C. These normal Hall coefficients show weak temperature dependence below 70 K. We have performed FLAPW energy band calculations with LDA for nonmagnetic CoS_2, ferromagnetic CoS_2, and nonmagnetic $CoSe_2$. The normal Hall coefficient R_N was evaluated for each magnetic state. It is found that the calculated R_N of ferromagnetic CoS_2 is comparable to the experimental $R_N{}^f$ of $Co(S_{1-x}Se_x)_2$ with $0.08 \leq x \leq 0.13$. The calculated R_N of nonmagnetic CoS_2 is negative and small, which is inconsistent with the experimental $R_N{}^p$ of $Co(S_{1-x}Se_x)_2$ with $0.11 \leq x \leq 0.14$. The origins of this discrepancy were discussed from both experimental and theoretical aspects. In the experiments, we pointed out the possibility that $R_N{}^p$ is overestimated. The concentration fluctuations may give rise to enhancement of the magnetic susceptibility in the paramagnetic state, which leads to excessive estimation of $R_N{}^p$. The calculated results have shown that R_N of the nonmagnetic state changes the sign from negative to positive by the induced magnetization. This may be an alternative explanation for the above discrepancy.

2. The Hall resistivity of $Lu(Co_{0.91}Al_{0.09})_2$ was measured at ambient pressure and at 0.5 GPa. The compound has a negative R_A. We analyzed the Hall data and estimated $R_N{}^f$ and $R_N{}^p$ based on the same assumption as $Co(S_{1-x}Se_x)_2$: R_A in the ferromagnetic state is the same as that in the paramagnetic state. The estimated $R_N{}^f$ is in the range of 10-50 $\times 10^{-11}$$m^3$/C below 70 K. On the other hand, $R_N{}^p$ is negative with large values of −100- −170 $\times 10^{-11}$ m^3/C. We compared the experimental results with the theoretical R_N obtained from FLAPW energy band calculations for ferromagnetic and nonmagnetic $LuCo_2$. The calculated R_N of ferromagnetic $LuCo_2$ is 30.7 $\times 10^{-11}$$m^3$/C. This value is comparable to the experimental $R_N{}^f$ of $Lu(Co_{0.91}Al_{0.09})_2$. On the other hand, the calculations give $R_N = 32.9 \times 10^{-11}$$m^3$/C for nonmagnetic $LuCo_2$. which is opposite in sign to the experimental $R_N{}^p$ of $Lu(Co_{0.91}Al_{0.09})_2$. The origin of this inconsistency was discussed in terms of a rigid-band approximation. We found that the hole bands are fully occupied by a slight shift of the Fermi energy, which makes R_N negative. These results indicate that R_N is sensitive to the position of ε_F in nonmagnetic $LuCo_2$. The shift of the Fermi level by the substitution of Al for Co can be an origin of the negative $R_N{}^p$ of $Lu(Co_{0.91}Al_{0.09})_2$.

3. We measured the $\rho_{xy} - B$ curves of RCo_2 (R = Lu and Er) at various temperatures. The ρ_{xy} of $LuCo_2$ increases in proportion to a magnetic field. Its slope R_{obs} rapidly decreases with increasing temperature from 4.2 K to 70 K. Our analyses suggest that the strong temperature dependence of R_{obs} originates in $R_N{}^p$. We roughly estimated $R_N{}^p$ of $LuCo_2$ in the range of 30-100 $\times 10^{-11}$$m^3$/C depending on temperature. The calculated R_N has the same sign as the experimental values of paramagnetic $LuCo_2$ and it is within the observed range.

4. In the ferrimagnetic state of $ErCo_2$, the ρ_{xy}/B vs. M/B plots show straight lines. From these plots, we can separate R_N^f and R_A, successfully. The estimated R_N^f is 15-40 × 10^{-11}m^3/C. This R_N^f is in agreement with the calculated R_N for ferromagnetic $LuCo_2$. Above T_C, the ρ_{xy} of $ErCo_2$ initially decreases with increasing field and shows a minimum, followed by abrupt increase at around B_C. We found that a linear relation between ρ_{xy}/B and M/B is realized in the paramagnetic state just above T_C in a certain field range. From the analyses, we obtain $R_N \sim 200 \times 10^{-11}$ m^3/C and negative R_A just above T_C. These results imply that the AHE of $ErCo_2$ changes the sign from positive to negative, when a ferrimagnetic state is replaced by a paramagnetic state. The sign change in the AHE is possibly explained by the impurity scattering, as shown for some rare-earth elements.

5. Temperature and field dependence of ρ_{xy} of $La(Fe_{1-x}Si_x)_{13}$ with x = 0.10 and 0.12 were examined at high pressures. These compounds have large and positive AHE. Karpenkov *et al*. discussed the AHE of $LaFe_{11.5}Si_{1.5}$ using Tian–Ye–Jin scaling model. We applied this model to our data of $La(Fe_{0.88}Si_{0.12})_{13}$ at 0.5 GPa. Karpenkov *et al*. also calculated the anomalous Hall conductivity (AHC) based on the electronic structure of $LaFe_{11.5}Si_{1.5}$. Their results indicate that the intrinsic contribution is dominant in the AHE of $La(Fe_{1-x}Si_x)_{13}$. It is reasonable to consider that R_A is strongly dependent on the magnetic state. Therefore, the assumption that R_A is independent of the magnetic state is not valid for $La(Fe_{1-x}Si_x)_{13}$. From the ρ_{xy}/B vs. M/B plots, we determined R_N^f and R_A as a function of temperature. It is found that R_N^f changes a sign from positive to negative near T_C. These results suggest that the electron mobility μ_e decreases more slowly that the hole mobility μ_h does with increasing temperature in $La(Fe_{1-x}Si_x)_{13}$. We also pointed out that positive jumps in the magnetoresistance curves in $La(Fe_{1-x}Si_x)_{13}$ are attributable to a sudden reduction of $N(\varepsilon_F)$ caused by IEM.

We can draw the following conclusions from the present study. Our analyses made it possible to determine both R_N^f and R_N^p in itinerant electron metamagnets, taking advantage of a unique characteristic of IEM. In the analyses, R_A is assumed to be independent of the magnetic state. We believe that the assumption is valid for, at least, $Co(S_{1-x}Se_x)_2$ and $Lu(Co_{0.91}Al_{0.09})_2$, because these compounds are solid solutions, in which the guest elements (Se and Al) are randomly distributed. These guest elements act as impurities in the lattice, so that the impurity scattering plays an important role in the AHE. In general, it is difficult to determine R_N^p of magnetic materials, because both the NHE and AHE show linear field dependence. For some rare-earth metals and those compounds, R_N^p and R_A were estimated from the temperature dependences of ρ_{xy} and the magnetic susceptibility, by assuming that R_N^p and R_A are independent of temperature [42, 96]. This assumption is, however, invalid for 3*d* transition metals, because the anomalous Hall effect strongly depends on temperature [42]. We emphasize that our research is the first report to estimate the normal Hall coefficient in the paramagnetic state of magnetic materials based on 3*d* transition metals, as far as we know. The present results revealed distinct difference between R_N^f and R_N^p. Such difference in the electronic states between the ferromagnetic and paramagnetic states has not been reported experimentally. The comparisons between the experimental values and theoretical results were also made. The theoretical results seem to be in a satisfactory agreement with the experimental values in

the ferromagnetic state. On the other hand, discrepancies between them were found in the paramagnetic state. We have shown that these discrepancies can be understood in the framework of a rigid band model. It has been demonstrated that IEM provides a unique stage to discuss the electronic structure between ferromagnetic and paramagnetic states. However, our results indicate that the electronic structures of IEM strongly depend on the material. In other words, IEM has a wide variety of electronic structures. In this context, further experimental and theoretical studies are strongly desired towards a unified picture of IEM.

References

[1] E. P. Wohlfarth, P. Rhodes, Collective electron metamagnetism, Philos. Mag. 7 (1962) 1817-1824, https://doi.org/10.1080/14786436208213848

[2] Kengo Adachi, Magnetism of Compounds, − Itinerant Electron System − (written in Japanese), Shokabo, Tokyo, 1996.

[3] R. S. Perry, K. Kitagawa, S. A. Grigera, R. A. Borzi, A. P. Mackenzie, K. Ishida, Y. Maeno, Multiple first-order metamagnetic transitions and quantum oscillations in ultrapure $Sr_3Ru_2O_7$, Phys. Rev. Lett. 92 (2004) 166602.
https://doi.org/10.1103/PhysRevLett.92.166602

[4] N.V. Mushnikov, T. Goto, K. Kamishima, H. Yamada,A.V. Andreev, Y. Shiokawa, A. Iwao, V. Sechovsky, Magnetic properties of the 5f itinerant electron metamagnet UCoAl under high pressure. Phys. Rev. B 59 (1999) 6877–6885.
https://doi.org/10.1103/PhysRevB.59.6877

[5] H. Wada, Y. Tanabe, Giant magnetocaloric effect of $MnAs_{1-x}Sb_x$, Appl. Phys. Lett. 79 (2001) 3302-3304. https://doi.org/10.1063/1.1419048

[6] A. Fujita, S. Fujieda, Y. Hasegawa, K. Fukamichi, Itinerant-electron metamagnetic transition and large magnetocaloric effects in $La(Fe_xSi_{1-x})_{13}$ compounds and their hydrides, Phys. Rev. B 67 (2003), 104416. https://doi.org/10.1103/PhysRevB.67.104416

[7] T. Waki, S. Terazawa, T. Yamazaki, Y. Tabata, K. Sato, A. Kondo, K. Kindo, M. Yokoyama, Y. Takahashi, H. Nakamura, Interplay between quantum criticality and geometric frustration in Fe_3Mo_3N with stella quadrangula lattice, EPL, 94 (2011) 37004.
doi:10.1209/0295-5075/94/37004

[8] M. Imai, C. Michioka, H. Ohta, A. Matsuo, K. Kindo, H. Ueda, K. Yoshimura, Anomalous itinerant-electron metamagnetic transition in the layered $Sr_{1-x}Ca_xCo_2P_2$ system, Phys. Rev. B 90 (2014) 014407. https://doi.org/10.1103/PhysRevB.90.014407

[9] L. V. B. Diop and O. Isnard, Avalanche-like magnetization process in itinerant-electron system $LaFe_{12}B_6$, J. Alloys Compd. 688 (2016) 953-957.
https://doi.org/10.1016/j.jallcom.2016.07.124

[10] M. Shimizu, Itinerant electron metamagnetism, J. Phys. (Paris) 40 (1982) 155-163.
https://doi.org/10.1051/jphys:01982004301015500

[11] H. Yamada, Metamagnetic transition and susceptibility maximum in an itinerant-electron system, Phys. Rev. B 47 (1993) 11211-11219.
https://doi.org/10.1103/PhysRevB.47.11211

[12] T. Goto, K. Fukamichi, H. Yamada, Itinerant electron metamagnetism and peculiar magnetic properties observed in 3d and 5f intermetallics, Physica B 300 (2001) 167-185.
https://doi.org/10.1016/S0921-4526(01)00579-8

[13] A. Piñeiro, A. S. Botana, V. Pardo and D. Baldomir, Fermiology and magnetism in weak itinerant

ferromagnet CoS_2: an ab initio study, J. Phys.Condens. Matter, 22 (2010) 505602. doi:10.1088/0953-8984/22/50/505602

[14] K. Adachi, M. Matsui, M. Kawai, Further investigations on magnetic properties of $Co(S_xSe_{1-x})_2$ $(0 \leq x \leq 1)$, J. Phys. Soc. Jpn. 46 (1979) 1474-1482.
https://doi.org/10.1143/JPSJ.46.1474

[15] T. Goto, Y. Shindo, H. Takahashi, S. Ogawa, Magnetic properties of the itinerant metamagnetic system $Co(S_{1-x}Se_x)_2$ under high magnetic fields and high pressure, Phys. Rev. B 56 (1997) 14019-14028. https://doi.org/10.1103/PhysRevB.56.14019.

[16] O. Sadakuni,, A. Mitsuda, H. Wada, Magnetocaloric effect of $Co(S_{1-x}Se_x)_2$ under high pressure, J. Phys. Soc. Jpn. 79 (2010) 024701. https://doi.org/10.1143/JPSJ.79.024701

[17] Carnegie Mellon University homepage. https://som.web.cmu.edu/structures/S032-Cu2Mg.html.

[18] S. Tanaka and H. Harima, Mass enhancement factor and Fermi surface in YCo_2, J. Phys. Soc. Jpn. 67 (1998) 2594–2597. https://doi.org/10.1143/JPSJ.67.2594

[19] K. Yoshimura, K. Fukamichi, H. Yasuoka, M. Mekata, NMR study of nearly itinerant ferromagnetic $LuCo_2$, J. Phys. Soc. Jpn. 56 (1987) 3652–3660.
https://doi.org/10.1143/JPSJ.56.3652

[20] E. Burzo, E. Gratz, V. Pop, On the magnetic behaviour of ACo_2 (A = Y, Lu, Zr, Sc and Hf) compounds, J. Magn. Magn. Mater. 123 (1993) 159–164.
https://doi.org/10.1016/0304-8853(93)90026-X

[21] J. Beille, D. Bloch, J. Voiron, The weak ferromagnetic properties of disordered-concentration transition metal alloys, AIP Conf. Proc. 29 (1976) 123.
https://doi.org/10.1063/1.30548

[22] W. Steiner, E. Gratz, H. Ortbauer, H. W. Camen, Magnetic properties, electrical resistivity and thermal expansion of $(Ho,Y)Co_2$, J. Phys. F 8 (1978) 1525.

[23] K. Schwarz, P. Mohn, Itinerant metamagnetism in YCo_2, J. Phys. F 14 (1984) L129-L134. DOI 10.1088/0305-4608/14/7/008

[24] H. Yamada, M. Shimizu, Metamagnetic transition of YCo_2, J. Phys. F 15 (1985) L175-L180. DOI 10.1088/0305-4608/15/6/007

[25] C. J. Schinkel, Anomalous high-field magnetisation of YCo_2 and $LuCo_2$, J. Phys. F 8 (1978) L87-L90. DOI 10.1088/0305-4608/8/4/003

[26] T. Goto, K. Fukamichi, T. Sakakibara, H. Komatsu, Itinerant electron metamagnetism in YCo_2, Solid State Commun. 72 (1989) 945-947.
https://doi.org/10.1016/0038-1098(89)90433-X

[27] T. Goto, T. Sakakibara, K. Murata, H. Komatsu, K. Fukamichi, Itinerant electron metamagnetism in YCo_2 and $LuCo_2$, J. Magn. Magn. Mater. 90-91 (1990) 700-702.
https://doi.org/10.1016/S0304-8853(10)80256-2

[28] D. Bloch, D. M. Edwards, M. Shimizu, J. Voiron, First order transitions in ACo_2 compounds, J. Phys. F 5 (1975) 1217−1226. DOI 10.1088/0305-4608/5/6/022

[29] R. M. Moon, W. C. Koehler, J. Farrell, Magnetic structure of rare-earth-cobalt (RCo_2) intermetallic compounds, J. Appl. Phys. 36 (1965) 978−979.
https://doi.org/10.1063/1.1714286
[30] A. Pirogov, A. Podlesnyak, T. Strässle, A. Mirmelstein, A. Teplykh, D. Morozov, A. Yermakov, Neutron-diffraction investigation of the metamagnetic transition in $ErCo_2$, Appl. Phys. A 74 (2002) s598–s600. https://doi.org/10.1007/s003390201617
[31] A. A. Abozeed, D. I. Gorbunov, T. Kadono, Y. Kanai-Nakata, K. Yamagami, H. Fujiwara, A. Sekiyama, A. Higashiya, A. Yamasaki, K. Tamasaku, M. Yabashi, T. Ishikawa, H. Wada, A. V. Andreev, S. Imada, Anisotropic magnetization and electronic structure of the first-order ferrimagnet $ErCo_2$ studied by polarization dependent hard X-ray photoemission spectroscopy, Physica B 649 (2023) 414465.
https://doi.org/10.1016/j.physb.2022.414465
[32] V. V. Aleksandryan, K. P. Belov, R. Z. Levitin, A. S. Markosyan, V. V. Snegirev, Giant increase in the Curie temperature of RCo_2 intermetallic rare-earth compounds at low degrees of replacement of magnetic cobalt by nonmagnetic aluminum, JETP Lett., 40 (1984) 815-818.
[33] K. Yoshimura, Y. Nakamura, New weakly itinerant ferromagnetic system, $Y(Co_{1-x}Al_x)_2$, Solid State Commun. 56 (1985) 767-771. https://doi.org/10.1016/0038-1098(85)90305-9
[34] V. V. Aleksandryan, A. S. Lagutin, R. Z. Levitin, A. S. Markosyan, Metamagnetism of itinerant d-electrons in YCo_2: Investigation of metamagnetic transitions in $Y(Co,Al)_2$, Sov. Phys. JETP 62 (1985) 153-155.
[35] T. Sakakibara, T. Goto, K. Yoshimura, M. Shiga, Y. Nakamura, Itinerant electron metamagnetism in $Y(Co_{1-x}Al_x)_2$, Phys. Lett. A 117 (5) (1986) 243-246.
https://doi.org/10.1016/0375-9601(86)90085-X
[36] I. L Gabelko, R. Z. Levitin, A. S. Markosyan, V. V. Snegirev, Onset of ferromagnetism in the band paramagnet $LuCo_2$ upon the replacement of cobalt by aluminium, JETP Lett. 45 (1987) 458-461.
[37] K. Endo, M. Iijima, A. Shinogi, K. Ishiyama, The metamagnetic transition in pseudobinary Laves phase compounds $Lu(Co_{1-x}Al_x)_2$, J. Phys. Soc. Jpn. 56 (1987) 1316-1319.
https://doi.org/10.1143/JPSJ.56.1316
[38] K. Fukamichi, T. Yokoyama, H. Saito, T. Goto, H. Yamada, Magnetic phase diagrams of itinerant-electron metamagnetic $Lu(Co_{1-x}M_x)_2$ (M =Al and Ga) Laves-phase compounds, Phys Rev. B 64 (2001) 134401. https://doi.org/10.1103/PhysRevB.64.134401
[39] W. Wang, R. Huang, W. Li, J. Tan, Y. Zhao, S. Li, C. Huang, L. Li, Zero thermal expansion in $NaZn_{13}$-type $La(Fe,Si)_{13}$ compounds, Phys. Chem. Chem. Phys., 17 (2015) 2352-2356.
https://doi.org/10.1039/C4CP04672B

[40] A. Fujita, S. Fujieda, K. Fukamichi, H. Mitamura, T. Goto, Itinerant-electron metamagnetic transition and large magnetovolume effects in $La(Fe_{1-x}Si_x)_{13}$ compounds, Phys. Rev. B 65 (2001) 014410. https://doi.org/10.1103/PhysRevB.65.014410
[41] Aakash Educational Services Ltd. homepage.
https://www.aakash.ac.in/important-concepts/physics/hall-effect

[42] C. M. Hurd, The Hall effect in metals and alloys, Plenum Press, New York, 1972.
[43] T. Oguch, HiLAPW (written in Japanese), Osaka University.
http://www.dyn.ap.eng.osaka-u.ac.jp/CMD/CMD13/HiLAPW_TEXT.pdf
[44] T. Oguchi, T. Sasaki, Fermi surface and transport properties of $YBa_2Cu_4O_8$, J. Phys. Chem. Solids 53 (12) (1992) 1525-1532. https://doi.org/10.1016/0022-3697(92)90139-5
[45] L. Berger, G. Bergmann, The Hall Effect of Ferromagnets, in: C.L.Chien, C. R .Westgate (Eds.), The Hall Effect and Its Applications, Plenum Press, New York, 1980, pp. 55–76.
[46] J. Smit, The spontaneous hall effect in ferromagnetics I, Physica 21 (1955) 877–887.
https://doi.org/10.1016/S0031-8914(55)92596-9
[47] J. Smit, The spontaneous hall effect in ferromagnetics II, Physica 24 (1958) 39–51.
https://doi.org/10.1016/S0031-8914(58)93541-9
[48] L. Berger, Side-jump mechanism for the Hall effect of ferromagnets, Phys. Rev. B 2 (1970) 4559–4566.
https://doi.org/10.1103/PhysRevB.2.4559
[49] L. Berger, Application of the side-Jump model to the Hall effect and Nernst effect in ferromagnets, Phys. Rev. B 5 (1972) 1862–1870. https://doi.org/10.1103/PhysRevB.5.1862
[50] R. Karplus, J. M. Luttinger, Hall effect in ferromagnetics, Phys. Rev. 95 (1954) 1154-1160.
https://doi.org/10.1103/PhysRev.95.1154
[51] N. Nagaosa, J. Sinova, S. Onoda, A. H. MacDonald, N. P. Ong, Anomalous Hall effect Rev. Mod. Phys. 82 (2010) 1539–1592. https://doi.org/10.1103/RevModPhys.82.1539
[52] K. Adachi, K. Sato and M. Takeda, Magnetic properties of cobalt and nickel dichalcogenide compounds with Pyrite structure, J. Phys. Soc. Jpn. 26 (1969) 631-638.
https://doi.org/10.1143/JPSJ.26.631
[53] T. Yokoyama, H. Nakajima, H. Saito, K. Fukamichi, H. Mitamura, T. Goto, Change in the itinerant-electron metamagnetic transition behavior by annealing in $Lu(Co_{1-x}Al_x)_2$ Laves phase compounds, J. Alloys. Compd. 266 (1998) 13-16.
https://doi.org/10.1016/S0925-8388(97)00464-7
[54] H. Wada, T. Inoue, M. Hada, M. Shiga, Y. Nakamura, Effect of magnetic phase transition on the Electronic specific heat coefficient of $Lu(Co_{1-x}Al_x)_2$, Phys. Status Solidi B 162 (1990) 407–411.
https://doi.org/10.1002/pssb.2221620210
[55] T. Oguchi, Augmented-plane-wave force calculations for transition-metal systems, in: K. Terakura, H. Akai (Eds.) Inter-atomic Potentials and Structural Stability, Springer-Verlag, Berlin, 1993, pp. 33-41.
[56] J. F. Janak, V. L. Moruzzi, A. R. Williams, Ground-state thermomechanical properties of some cubic elements in the local-density formalism, Phys. Rev. B 12 (4) (1975) 1257-1261.
https://doi.org/10.1103/PhysRevB.12.1257
[57] P. E. Blöchl, O. Jepsen, and O. K. Andersen, Improved tetrahedron method for Brillouin-zone integrations, Phys. Rev. B 49 (23) (1994) 16223-16233.
https://doi.org/10.1103/PhysRevB.49.16223
[58] M. Kawamura, FermiSurfer: Fermi-surface viewer providing multiple representation schemes, Comp. Phys.

Commun. 239 (2019) 197-203.
https://doi.org/10.1016/j.cpc.2019.01.017
[59] T. Shishidou,A. J. Freeman , R. Asahi, Effect of GGA on the half-metallicity of the itinerant ferromagnet CoS_2, Phys. Rev. B 64 (18) (2001) 180401.
https://doi.org/10.1103/PhysRevB.64.180401
[60] A. Teruya, F. Suzuki, D. Aoki, F. Honda, A. Nakamura, M. Nakashima, Y. Amako, H. Harima, K. Uchima, M. Hedo, T. Nakama, and Y. Onuki, Fermi Surface and Magnetic Properties in Ferromagnet CoS_2 and Paramagnet $CoSe_2$ with the Pyrite-type Cubic Structure, J. Phys.: Conf. Series 807 (2017) 012001.
https://doi.org/10.1088/1742-6596/807/1/012001
[61] T. Takahashi, Y. Naitoh, T. Sato, T. Kamiyama, K. Yamada, H. Hiraka, Y. Endoh, M. Usuda,N. Hamada, Para- to ferromagnetic phase transition of CoS_2 studied by high-resolution photoemission spectroscopy, Phys. Rev. B 63 (2001) 094415.
https://doi.org/10.1103/PhysRevB.63.094415
[62] T. Sato, S. Souma, K. Sugawara, K. Nakayama, S. Raj, H. Hiraka, T. Takahashi, Xenon-plasma-light low-energy ultrahigh-resolution photoemission study of $Co(S_{1-x}Se_x)_2$ (x = 0.075), Phys. Rev. B 76 (2007) 113102.
https://doi.org/10.1103/PhysRevB.76.113102
[63] H. Wada, Y. Maekawa, D. Kawasaki, High-field transport properties of itinerant electron metamagnetic $Co(S_{1-x}Se_x)_2$, J. Sci.:Adv. Mater. Devices 1 (2016) 179-184.
https://doi.org/10.1016/j.jsamd.2016.06.001
[64] E. Nowack, D. Schwarzenbach, Th. Hahn, Charge densities in CoS_2 and NiS_2 (pyrite structure), Acta Cryst. B47 (1991) 650-659. https://doi.org/10.1107/S0108768191004871
[65] S. Furuseth, A. Kjekshus and A. F. Andresen, On the magnetic properties of $CoSe_2$, NiS_2 and $NiSe_2$, Acta Chem. Scand. 23 (1969) 2325-2334.
DOI: 10.3891/acta.chem.scand.23-2325
[66] R. Ballou, B. Barbara, Z. M. Gamishidze, R. Lemaire, R. Z. Levitin, A. S. Markosyan, A spin-glass state in the itinerant magnet systems $Y(Co_{1-x}Mn_x)_2$ and $Lu(Co_{1-x}Mn_x)_2$, J. Magn. Magn. Mater. 119 (1993) 294-300.
https://doi.org/10.1016/0304-8853(93)90414-W
[67] M. Aoki, H. Yamada, Electronic structure of the ordered ternary compound $Y(M_{0.75}Al_{0.25})_2$ (M = Co and Fe) with C15-type laves phase structure, J. Magn. Magn. Mater. 78 (1989) 377-383.
https://doi.org/10.1016/0304-8853(89)90209-6
[68] K. Nakada, H. Shimizu, H. Yamada, H. Harima, Magnetic properties and Fermi surface of YMn_2, J. Magn. Magn. Mater. 262 (2003) 374–381.
https://doi.org/10.1016/S0304-8853(03)00067-2
[69] S. Ziri, L. Blaha, F. Boukabrine, A. Maafa, A. Oughilas, A. Bouabça, H. Rozale, Probing the structural, elastic, electronic and thermoelectric properties of C15-type Laves phase LaCo2: a DFT based ab-initio investigation, Rev. Mex. de Fıs. 67 (2021) 041003.
https://doi.org/10.31349/RevMexFis.67.4.041003
[70] E. Burzo, P. Vlaic, D.P. Kozlenko, S.E. Kichanov, A.V. Rutkauskas, B.N. Savenk, Crystal structure and

magnetic behaviour of $DyCo_2$ compound at high pressures, J. Alloys. Compd. 724 (2017) 1184−1191. http://dx.doi.org/10.1016/j.jallcom.2017.07.078

[71] D. Huang, H. Li, B. Ding, X. Xi, J. Gao, Y. Lau, W. Wang, Plateau-like magnetoresistance and topological Hall effect in Kagome magnets $TbCo_2$ and $DyCo_2$, Appl. Phys. Lett. 121, (2022) 232404. https://doi.org/10.1063/5.0111086

[72] J. S. Dugdale, The electrical properties of metals and alloys, Edward Arnold, London, 1977.

[73] N. P. Ong, Geometric interpretation of the weak-field Hall conductivity in two-dimensional metals with arbitrary Fermi surface, Phys. Rev. B 43, (1991) 193–201.
https://doi.org/10.1103/PhysRevB.43.193

[74] J. M. Ziman, Approximate calculation of the anisotropy of the relaxation time of the conduction electrons in the noble metals, Phys. Rev. 121 (1961) 1320–1324.
https://doi.org/10.1103/PhysRev.121.1320

[75] J. S. Dugdale, L. D. Firth, The Hall coefficient of dilute alloys of copper and silver, J. Phys. C 2 (1969) 1272–1284. DOI 10.1088/0022-3719/2/7/319

[76] J. J. Rhyne, Anomalous Hall Effect in Single-Crystal Dysprosium, Phys. Rev. 172 (1968) 523−529. https://doi.org/10.1103/PhysRev.172.523

[77] J. J. Rhyne, Anomalous and Ordinary Hall Effect in Terbium, J. Appl. Phys. 40 (1969) 1001−1003. https://doi.org/10.1063/1.1657500

[78] M. Christen, B. Giovannini, J. Sierro, Extraordinary Hall-effect in ferromagnetic (rare-earth) $A1_2$, Phys. Rev.B 20 (1979) 4624−4632. https://doi.org/10.1103/PhysRevB.20.4624

[79] R. S. Lee, S. Legvold, Hall Effect of Gadolinium, Lutetium, and Yttrium Single Crystals, Phys. Rev. 162 (1967) 431 – 435.
https://doi-org.anywhere.lib.kyushu-u.ac.jp/10.1103/PhysRev.162.431

[80] J. Kondo, Anomalous Hall effect and magnetoresistance of ferromagnetic metals, Prog. of Theor. Phys. 27 (1962) 772−792.
https://doi.org/10.1143/PTP.27.772

[81] F. E. Maranzana, Contributions to the Theory of the Anomalous Hall Effect in Ferro- and Antiferromagnetic Materials, Phys. Rev. 160 (1967) 421−429.
https://doi.org/10.1103/PhysRev.160.421

[82] B.Giovannini, Theory of the anomalous hall effect in the rare earths, Phys. Lett. 36A (1971) 381-382. https://doi.org/10.1016/0375-9601(71)90269-6

[83] A. Fert, On the extraordinary hall effect of the rare-earth metals, J. Physique Lett. 35 (1974) 107-110. https://doi.org/10.1051/jphyslet:01974003507-8010700

[84] Y. Xu, L. Elcoro, Z. Song, B. J. Wieder, M. G. Vergniory, N. Regnault, Y. Chen, C. Felser, B. A. Bernevig, High-throughput calculations of magnetic topological materials, Nature 586 (2020) 702-707. https://doi.org/10.1038/s41586-020-2837-0

[85] A. Fujita, K. Takenaka, "Entropics": Science and engineering of caloric phenomena related to itinerant-electron magnetism and spin fluctuations, J. Phys.: Conf. Ser. 868 (2017) 012004. DOI :10.1088/1742-

6596/868/1/012004
[86] T. T. M. Palstra, J. A. Mydosh, G. J. Nieuwenhuys, A. M. van der Kraan, K. H. J. Buschow, Study of the critical behaviour of the magnetization and electrical resistivity in cubic La(Fe, Si)$_{13}$ compounds, J. Magn. Magn. Mater. 36 (1983) 290-296.
https://doi.org/10.1016/0304-8853(83)90128-2
[87] A. Fujita, Relation between paramagnetic entropy and disordered local moment in La(Fe$_{0.88}$Si$_{0.12}$)$_{13}$ magnetocaloric compound, APL Mater 4 (2016) 064108.
https://doi.org/10.1063/1.4953434
[88] D. Yu. Karpenkov, K. P. Skokov, I. A. Radulov, O. Gutfleisch, J. Weischenberg, H. Zhang, Anomalous Hall effect in La(Fe,Co)$_{13-x}$Si$_x$ compounds, Phys. Rev. B 100 (2019) 094445. https://doi.org/10.1103/PhysRevB.100.094445
[89] A. Fujita, private communication.
[90] Y. Tian, L. Ye, and X. Jin, Proper scaling of the anomalous Hall effect, Phys. Rev. Lett. 103 (2009) 087206. https://doi.org/10.1103/PhysRevLett.103.087206
[91] D. Hou, G. Su, Y. Tian, X. Jin, S. A. Yang, Q. Niu, Multivariable scaling for the anomalous Hall effect, Phys. Rev. Lett. 114 (2015) 217203.
https://doi.org/10.1103/PhysRevLett.114.217203
[92] D. Yue, X. Jin, Towards a better understanding of the anomalous Hall effect, J. Phys. Soc. Jpn.86 (2017) 011006. https://doi.org/10.7566/JPSJ.86.011006
[93] M. E. Gruner, W. Keune, B. Roldan Cuenya, C. Weis, J. Landers, S. I. Makarov, D. Klar, M. Y. Hu, E. E. Alp, J. Zhao, M. Krautz, O. Gutfleisch, H. Wende, Element-Resolved Thermodynamics of Magnetocaloric LaFe$_{13-x}$Si$_x$, Phys. Rev. Lett. 114 (2015) 057202. https://doi.org/10.1103/PhysRevLett.114.057202
[94] A. Fujita, K. Fukamichi, J.-T. Wang, Y. Kawazoe, Large magnetovolume effects and band structure of itinerant-electron metamagnetic La(Fe$_x$Si$_{1-x}$)$_{13}$ compounds, Phys. Rev. B 68 (2003) 104431. https://doi.org/10.1103/PhysRevB.68.104431
[95] G. Wang, F. Wang, N. Di, B. Shen, Z. Cheng, Hyperfine interactions and band structures of LaFe$_{13-x}$Si$_x$ intermetallic compounds with large magnetic entropy changes, J. Magn. Magn. Mater. 303 (2006) 84-91. https://doi.org/10.1016/j.jmmm.2005.10.231
[96] K. Yagasaki, T. Nakama, N. Nakama, Paramagnetic Hall effect in cubic rare earth compounds, J. Magn. Magn. Mater. 90-91 (1990) 577-578. https://doi.org/10.1016/S0304-8853(10)80212-4

Acknowledgments

The author would like to express his gratitude to Prof. H. Wada of Kyushu University for his enthusiastic guidance on physics. I would also like to thank Dr. A. Mitsuda for his guidance in experiments and academic discussions.

This research was possible with the support of many collaborators.

I am sincerely grateful to Dr. K. Yamauchi of Osaka University for band calculations.

Special thanks to Prof. Prof. H. Harima of Kobe University and Prof. T. Oguchi of Osaka University for discussions on theoretical calculations.

I am thankful to thank Prof. T. Kimura and Dr. O. Narikiyo and S. Nakamura of Kyushu University for their kind acceptance as the referees of my thesis.

I would like to acknowledge Mr. Y. Maekawa and Mr S. Hatoyama of the Physics of Magnetism Laboratory, Department of Physics. Kyushu University for their grateful help in measurement of Hall resistivity.

I appreciate Dr. K. Ohyama of the Physics of Magnetism Laboratory, Department of Physics. Kyushu University, for his technical advice.

All the members in the Physics of Magnetism Laboratory, Department of Physics, Kyushu University, are greatly acknowledged for their help in experiments and valuable comments.

Finally, I would like to express my gratitude to my family for their mental and financial supports.